الجمهورية الجزائرية الديمقراطية الشعبية

République Algérienne Démocratique et Populaire
Ministère de L'Enseignement Supérieur et de la Recherche Scientifique



UNIVERSITÉ SETIF 1-Ferhat ABBAS

FACULTÉ DE TECHNOLOGIE

THÈSE

Présentée au Département de Génie des Procédés

Pour l'obtention du diplôme de

DOCTORAT

Domaine : Sciences et Technologie

Filière : Génie des Procédés **Option : Génie Chimique**

Par

ACHOUR Mahdi

THÈME

Valorization of biomass by catalytic hydrogenation and deoxygenation reaction

Soutenue le .../…/2026 devant le Jury :

BENCHEIKH Lahcene	**Professeur**	**Univ. Sétif1-Ferhat ABBAS**	**Président**
AMMARI Fatima	**Professeur**	**Univ. Sétif1-Ferhat ABBAS**	**Directrice de thèse**
IVANOVA Svetlana	**Professeur**	**Univ. Séville**	**Co-Directrice**
OUARI Kamel	**Professeur**	**Univ. Sétif1-Ferhat ABBAS**	**Examinateur**
BOURAS Omar	**Professeur**	**Univ. Saad Dahlab Blida-1**	**Examinateur**
ZOUAOUI-MAHZOUL Nabila	**Docteur**	**Univ. Haute Alsace Mulhouse**	**Examinatrice**

الجمهورية الجزائرية الديمقراطية الشعبية

DEMOCRATIC AND POPULAR REPUBLIC OF ALGERIA
MINISTRY OF HIGHER EDUCATION AND SCIENTIFIC RESEARCH



Setif 1 University-Ferhat ABBAS

Faculty of Technology

Thesis submitted to the Process Engineering Department for a Doctorate Degree

Domain: Science and Technology

Section: Process Engineering **Option: Chemical Engineering**

BY

ACHOUR Mahdi

TITLE OF THE THESIS

Valorization of biomass by catalytic hydrogenation and deoxygenation reaction

Defended on …/…/ 2026 in front of the Jury:

BENCHEIKH Lahcene	**Professor**	**SETIF-1 University-Ferhat ABBAS**	**Chairman**
AMMARI Fatima	**Professor**	**SETIF-1University-Ferhat ABBAS**	**Supervisor**
IVANOVA Svetlana	**Professor**	**Seville University**	**Co-Supervisor**
OUARI Kamel	**Professor**	**SETIF-1University-Ferhat ABBAS**	**Examinator**
BOURAS Omar	**Professor**	**Blida-1 University**	**Examinator**
ZOUAOUI-MAHZOUL Nabila	**PhD**	**Haute Alsace Mulhouse University**	**Examinator**

ACKNOWLEDGMENTS

First and foremost, I thank God for granting me the strength and guidance to accomplish this work.

I would like to express my sincere gratitude to my supervisor**,** ***Professor Fatima AMMARI***, University of Sétif-1, for her valuable supervision and for following this work with great interest. I am deeply thankful for her advice, continuous support, trust, and the high quality of her guidance throughout this research.

I would also like to express my sincere gratitude to my co-supervisor, ***Professor Svetlana IVANOVA***, for her valuable scientific guidance, insightful discussions, and constructive suggestions throughout this research. Her expertise, critical perspective, and continuous support greatly contributed to the development and quality of this work.

I am extremely honored that ***Professor Lahcene BENCHEIKH***, University of Ferhat Abbas–Sétif 1, accepted to chair the jury of this thesis.

I would also like to express my sincere gratitude to ***Professor Kamel OUARI***, University of Ferhat Abbas–Sétif 1, for accepting to serve as an examiner and for his valuable evaluation of this work.

My sincere thanks are extended to ***Professor Omar BOURAS***, University of Saad Dahlab Blida-1, for kindly agreeing to examine this thesis and for his insightful comments.

I am also grateful to ***Doctor Nabila ZOUAOUI-MAHZOUL***, University of Haute-Alsace, Mulhouse, for accepting to serve as an examiner and for her careful review and constructive feedback.

I am also grateful to ***Professor Messaoud GUELLAL***, Head of the LGPC Laboratory, for his support and encouragement throughout this work.

I would like to express my sincere gratitude to ***Professor Miguel Ángel CENTENO***, Head of the laboratory at CSIC Sevilla, for providing an excellent research environment and access to laboratory facilities.

We gratefully acknowledge the support and facilities provided by the ***Departamento de Química Inorgánica*** and ***the Instituto de Ciencia de Materiales de Sevilla (ICMS)***, a joint research center of the ***Spanish National Research Council (CSIC)*** and the ***University of Seville***. Their scientific environment and infrastructure were essential for the development of this work.

This work was supported by ***the ERASMUS KA-171 program***, whose contribution to international academic mobility and collaboration is gratefully acknowledged.

We gratefully acknowledge ***Doctor CHARF EDDINE BOUNOUKTA*** for his encouragement and kind support throughout this work.

We gratefully acknowledge ***Doctor Débora Álvarez-Hernández*** for her valuable help and assistance in the laboratory during this work.

DEDICATION

I dedicate this thesis to my late father and my beloved brother Omar, whose memory continues to guide me in everything I do.

To my mother and my sisters, thank you for your unconditional love, patience, and constant support during this long journey.

This achievement is as much yours as it is mine

2,5-DMF :2,5-Dimethylfuran

5-HMF :5-Hydroxymethylfurfural

5-MFA :5-Methylfurfuryl Alcohol

5-MF :5-Methylfurfural

BET :Brunauer–Emmett–Teller (Surface Area Measurement)

C_3N_4 : Carbon Nitride (Graphitic Carbon Nitride)

CHN : Carbon, Hydrogen, Nitrogen (Elemental Analysis)

CO_2: Carbon Dioxide

CTH: Catalytic Transfer Hydrogenation

DAD: Diode Array Detector

DRS: Diffuse Reflectance Spectroscopy

FAD: Formic Acid Dehydrogenation

GC: Gas Chromatography

GC–MS: Gas Chromatography–Mass Spectrometry

HDO: Hydrodeoxygenation

HPLC: High Performance Liquid Chromatography

H_2: Di-hydrogen

ICP-OES: Inductively Coupled Plasma Optical Emission Spectroscopy

RI: Refractive Index Detector

TOF: Turnover Frequency

TON: Turnover Number

XPS: X-ray Photoelectron Spectroscopy

XRD: X-ray Diffraction

Figure I.1. Formic acid decomposition reaction in gas phase. 7
Figure I.2: Formic acid production from glucose and related reactions. 8
Figure I.3: Glucose oxidation in methanol over polyoxymethylene (POM) based catalysts ... 10
Figure I.4. 5-hydroxymethylfurfural (HMF) structure. 12
Figure I.5. Schemes of the reaction steps from glucan to HMF. 13
Figure I.6: Catalytic hydrogenation/hydrogenolysis of 5-HMF to 2,5-DMF. 15
Figure II.1: Preparation of the supports and the catalysts 31
Figure II.2 :Diffraction phenomena 33
Figure II.3: Adsorption Isotherm types according to IUPAC classifications 36
Figure II.4: Schematic Representation of the XPS Photoemission Process 38
Figure II.5: Representative scheme of the reduction furnace. 39
Figure II.6: Stainless-steel Parr 4848 autoclave reactor 40
Figure III.1: N_2-physisorption of the prepared supports and Pd-based catalysts. 52
Figure III.2:X-ray diffractograms of 5Pd-M_xU_y-T 54
Figure III.3: UV-VIS spectra of M_xU_y-T and 5Pd M_xU_y-T samples 57
Figure III.4: XRD diffraction patterns of PdNi and PdCo catalysts 61
Figure III.5: XPS survey scan spectra of the synthesized catalysts 64
Figure III.6: Pd3d spectra for the catalysts 65
Figure IV.1: Generated gas pressure and formic acid conversion over different 5Pd-MxUy -T catalysts 72
Figure VI.2: Comparison of formic acid dehydrogenation reaction in water and THF solvents 75
Figure IV.3: FA conversion vs. BET surface area and FA conversion vs. Pd particle size. 76
Figure IV.4: Generated gas pressure and formic acid conversion over PdCo catalysts 80
Figure IV.5: Generated gas pressure and formic acid conversion over PdNi catalysts 81
Figure IV.6: Effect of Pd/M ratio on total gas volume generation 83
Figure IV.8: Generated gas pressure and 5-HMF conversion and 2,5-DMF yield over different 5Pd-MxUy -600 catalysts 84
Figure IV.9: Products selectivity over different 5Pd-MxUy -600 catalysts 86
Figure IV.10: Generated pressure and Conversion over the PdCo bimetallic catalysts for 5-HMF 88
Figure IV.11: Genetated pressure and 5-HMF Conversion over the PdNi bimetallic catalysts for 5-HMF 90

Figure IV.12: Products yields and Selectivity over different PdCo catalysts for 5-HMF HDO 91
Figure IV.13: Products yields and Selectivity over PdNi catalysts for 5-HMF HDO 93
Figure IV.14: Recyclability of 5-CN 96

Table I.1: Overview of the catalytic systems used for formic acid production from glucose.. 11
Table I.2: Formic acid as hydrogen donor in the catalytic transfer hydrogenation of HMF. ... 17
Table II.1: List of prepared catalysts ... 32
Table II.2: List of prepared bimetallic catalysts. ... 32
Table III.1: ICP-OES analysis of the Pd-MxUy-T catalysts ... 49
Table III.2: CNH analysis and solid yield. ... 50
Table III.3: Textural properties of the prepared supports and catalysts ... 53
Table III.4: Structural parameters, Pd particle size and Pd content of the prepared catalysts . 55
Table III.5: ICP-OES analysis of the Pd-MxUy-T catalysts ... 58
Table III.6: Elemental analysis of the PdCo and PdNi catalysts ... 59
Table III.7 : Lattice Parameters, Palladium Particle Size, and Metal Dispersion of the Catalysts Supported on C_3N_4 ... 63
Table III.8 : XPS results, surface composition ... 63
Table IV.1: Total gas volume, CO_2 concentration in liquid ((bi)carbonates and in gas phase and carbon balance. ... 73
Table IV.2. Generated total volume of gas and CO_2 concentration for the reactions performed in water and THF ... 74
Table. IV.3. TON and TOF for different palladium-based catalysts ... 78
Table IV.4: Total gas volume, CO_2 concentration in liquid ((bi)carbonates) and in gas phase and carbon balance. ... 82
Table IV.5: Effect of Pd/M ratio on total gas volume generation. ... 94
Table IV.6: Turnover number (TON) and turnover frequency (TOF) for the catalytic conversion of 5-HMF to DMF over Pd-based mono and bimetallic catalysts ... 94

General Introduction 1

Chapter I: Literature Review

I.1. Hydrogen generation from formic acid FA 6

I.1.1. Production of formic acid from biomass 7

I. 1.1.1 Hydrogen peroxide as the oxidant 8

I. 1.1.2. Molecular oxygen as the oxidizing agent 9

I.2. Production and valorization of 5-hydroxymethylfurfural HMF as a platform chemical 11

I. 2.1 HMF as a versatile platform chemical 11

I. 2.2 HMF valorization 13

I.3. Research aims 18

Chapter II: Experimental techniques

II.1. Support and catalysts synthesis 30

II.1.1. Graphitic carbon nitrides properties and method of preparation 30

II.1.1. Pd/C_3N_4 catalysts synthesis 30

II.2. Characterization Techniques 33

II.2.1. Powder X-Ray Diffraction (XRD) 33

II.1.2 CHN Elemental Analysis 34

II.1.3 Inductively coupled plasma–optical emission spectroscopy (ICP-OES) 34

II.1.4 Textural Properties by N_2 Adsorption 35

II.1.5 UV–Visible Diffuse Reflectance Spectroscopy (UV–Vis DRS) 36

II.1.6 X-Ray Photoelectron Spectroscopy (XPS) 37

II.1.7 Pyrolysis 38

II.3. Catalytic activity measurements and analysis 39

II.3.2. Analytical method for products separation and analysis 41

Chapter III: Results of catalysts characterization

III.1. Characterization of monometallic Pd-based catalysts 49

III.1.1 Chemical analysis by ICP-OES spectrometry 49
III.1.2 Elemental analysis 49
III.1.4. XRD results 54
III.1.5. UV-Vis spectroscopy: 56
III.2. Characterization of bimetallic catalysts 57
III.2.1. Chemical analysis by ICP-OES spectrometry 58
III.2.2. Elemental analysis 59
III.2.3 XRD-analysis 60
III.2.4 XPS-analysis 63
III.3. Partial Conclusion 66

Chapter IV: Catalytic Results

IV.1. Formic acid dehydrogenation 71
IV.1.1. Pd-based catalysts 71
IV.1.1.1. Effect of tetrahydrofuran (THF) solvent 74
IV.1.1.2. Reactivity-structure correlation 75
IV.1.2 Bimetallic catalysts 79
IV.2. HMF hydrodeoxygenation 83
IV.2.1. Pd-based catalysts 83
IV.2.2. Bimetallic catalysts 87
IV.2.2.1. Catalyst recyclability studies 95
IV.3. Partial conclusion 96

General Conclusion and Perspectives 102

GENERAL INTRODUCTION

General Introduction

Decreasing fossil fuel resources associated with the increased petroleum demand by emerging economies, drives our society to search for a renewable energy resource. Lignocellulosic (LCB) biomass, which is the principal low-cost and sustainable biomass provides an important source of renewable carbon that can be sustainably converted into chemicals and fuels. In the last decades, a considerably efforts have been made to develop new technologies for biomass upgrading into high value-added chemicals [1]. The key processes to transform these molecules into chemicals and biofuels are hydrogenation and hydrogenolysis reactions. In the particular case of biomass, we frequently refer to hydrodeoxygenation (HDO) as a hydrogenolytic reaction in connection to the reduction of oxygen content of all LCB derived molecules[2,3]. The main challenge of the HDO mediated processes is to remove as much oxygen as possible while using the least possible amount of hydrogen. Molecular hydrogen (H_2) has been widely employed as hydrogen donor for HDO processes due to its beneficial activation potential on metal surfaces and to its availability. Nevertheless, its use presents some considerable issues owing to the high pressure H2 over-utilization, and its high cost and safety hazards during transportation, storage, and use. Formic acid (FA), has been recently identified as one of the most important and safest chemical molecules for hydrogen storage as well as a hydrogen donor for catalytic hydrogenation [4,5] due to its ability to decompose rapidly and selectively into H_2 and CO_2 under mild conditions [6–8].

However, the catalytic system for that purpose must participate selectively in formic acid dehydrogenation to assure the good hydrogen supply and then in hydrogenation/hydrogenolysis reactions. Usually, the catalysts that can assure the dehydrogenation participate also in hydrogenation reaction. On the other hand, 5-Hydroxymethylfurfural (HMF) is considered as one of the most flexible platform chemicals obtained from biomass. Its two functional groups along with the furan ring, makes it a promising precursor for many chemical reactions. In this regard, high-value HMF derivatives include 2,5-bis-(hydroxymethyl)furan (BHMF) [9], 5-methylfurfural (MF) [10], 5-methylfurfuryl alcohol (MFA) [11] and 2,5-dimethylfuran (DMF) [12].

Among them, 2,5-Dimethylfuran (DMF) product stands out as an exceptional fuel candidate due to its remarkably high-octane number (RON 119), superior energy content (30 MJ/L) in comparison to ethanol (23 MJ/L), ease of mixing with gasoline, high boiling point and

immiscibility with water [13,14]. Additionally, 2,5-DMF serves as a versatile building block for high-value aromatic compounds synthesis, through Diels–Alder reactions [15].

2,5-DMF may be readily produced from 5-hydroxymethylfurfural (HMF) by hydrogenation of bio-derived substrates, either using gaseous hydrogen or another alternative sources through catalytic transfer hydrogenation (CTH) by using formic acid as hydrogen donor [16–20]. Several catalytic systems, mostly based on palladium, were reported to catalyze formic acid dehydrogenation (FAD) and CTH reactions [21,22].

The main objective of this project is to investigate the performance of graphitic carbon nitrides supported Pd nanoparticles for the hydrodeoxygenation of 5-hydroxymethylfurfural (5-HMF) using formic acid as hydrogen donor molecule. The effect of some parameters of support synthesis, like used precursors and temperature of thermal decomposition, on catalytic properties and reactivity is also studied.

This manuscript consists of four chapters. The first bibliographic chapter describes the importance of 5-hydroxymethylfurfural (5-HMF) as a platform molecule and a synthesis of all its valorization reactions, in particular, the hydrodeoxygenation reaction. Chapter II is devoted to the description of synthesis methods, experimental techniques for characterization of catalysts, catalytic tests and operating conditions. Chapter III presents the results of physicochemical characterizations (N_2 Adsorption-Desorption, XRD, UV-VIS spectroscopy) of the synthesized catalysts. Chapter IV studies the results obtained from hydrodeoxygenation reactions.

References

[1] C. Herna, I. Valdez-vazquez, J.A. Acevedo-benı, Distribution and potential of bioenergy resources from agricultural activities in Mexico, 14 (2010) 2147–2153. https://doi.org/10.1016/j.rser.2010.03.034.

[2] A.R. Ardiyanti, S.A. Khromova, R.H. Venderbosch, V.A. Yakovlev, H.J. Heeres, Applied Catalysis B : Environmental Catalytic hydrotreatment of fast-pyrolysis oil using non-sulfided bimetallic Ni-Cu catalysts on a ʕ -Al 2 O 3 support, "Applied Catal. B, Environ. 117–118 (2012) 105–117. https://doi.org/10.1016/j.apcatb.2011.12.032.

[3] M.J. Gilkey, B. Xu, Heterogeneous Catalytic Transfer Hydrogenation as an E ff ective Pathway in Biomass Upgrading, 5 (2016). https://doi.org/10.1021/acscatal.5b02171.

[4] Demirbaş, A. Biomass Resource Facilities and Biomass Conversion Processing for Fuels and Chemicals. *Energy Convers. Manag.* **2001**, *42* (11), 1357–1378. https://doi.org/10.1016/S0196-8904(00)00137-0

[5] T. Wang, J. Du, Y. Sun, X. Tang, Z. Wei, X. Zeng, S. Liu, L. Lin, Catalytic transfer hydrogenation of biomass-derived furfural to furfuryl alcohol with formic acid as hydrogen donor over CuCs-MCM catalyst, Chinese Chem. Lett. 32 (2021) 1186–1190. https://doi.org/10.1016/j.cclet.2020.07.044.

[6] D.A. Bulushev, J.R.H. Ross, Towards Sustainable Production of Formic Acid, ChemSusChem. 11 (2018) 821–836. https://doi.org/10.1002/cssc.201702075.

[7] S. Enthaler, V. Langermann, T. Schmidt, Carbon dioxide and formic acid — the couple for environmental-friendly hydrogen storage ?, (2010) 1207–1217. https://doi.org/10.1039/b907569k.

[8] W. Yang, P. Li, D. Bo, H. Chang, The optimization of formic acid hydrolysis of xylose in furfural production, Carbohydr. Res. 357 (2012) 53–61. https://doi.org/10.1016/j.carres.2012.05.020.

[9] Q. Cao, W. Liang, J. Guan, L. Wang, Q. Qu, X. Zhang, X. Wang, X. Mu, Applied Catalysis A : General Catalytic synthesis of 2 , 5-bis-methoxymethylfuran : A promising cetane number improver for diesel, "Applied Catal. A, Gen. 481 (2014) 49–53. https://doi.org/10.1016/j.apcata.2014.05.003.

[10] S. Fulignati, C. Antonetti, D. Licursi, M. Pieraccioni, E. Wilbers, H. Jan, A. Maria, R. Galletti, Applied Catalysis A , General Insight into the hydrogenation of pure and crude HMF to furan diols using Ru / C as catalyst, Appl. Catal. A, Gen. 578 (2019) 122–133. https://doi.org/10.1016/j.apcata.2019.04.007.

[11] Hu, L.; Tang, X.; Xu, J.; Wu, Z.; Lin, L.; Liu, S. Selective Transformation of 5-Hydroxymethylfurfural into the Liquid Fuel 2,5-Dimethylfuran over Carbon-Supported Ruthenium. *Ind. Eng. Chem. Res.* **2014**, *53* (8), 3056–3064. https://doi.org/10.1021/ie404441a

[12] L. Hu, L. Lin, S. Liu, Chemoselective hydrogenation of biomass-derived 5-hydroxymethylfurfural into the liquid biofuel 2, 5-dimethylfuran, Ind. Eng. Chem. Res. 53 (2014) 9969–9978.

[13] A.T. Hoang, A. Pandey, Z. Huang, R. Luque, K.H. Ng, A.M. Papadopoulos, W.-H.

Chen, S. Rajamohan, H. Hadiyanto, X.P. Nguyen, Catalyst-based synthesis of 2, 5-dimethylfuran from carbohydrates as a sustainable biofuel production route, ACS Sustain. Chem. Eng. 10 (2022) 3079–3115. https://doi.org/10.1021/acssuschemeng.1c06363

[14] D.C. Nguyen, A.T. Hoang, Q.V. Tran, H. Hadiyanto, K. Wattanavichien, V.V. Pham, A review on the performance, combustion, and emission characteristics of spark-ignition engine fueled with 2, 5-dimethylfuran compared to ethanol and gasoline, J. Energy Resour. Technol. 143 (2021) 40801. https://doi.org/10.1115/1.4048228

[15] I.F. Teixeira, B.T.W. Lo, P. Kostetskyy, M. Stamatakis, L. Ye, C.C. Tang, G. Mpourmpakis, S. Chi, E. Tsang, Biomass Conversion From Biomass-Derived Furans to Aromatics with Ethanol over Zeolite, (2016) 13061–13066. https://doi.org/10.1002/anie.201604108.

[16] T. Thananatthanachon, T.B. Rauchfuss, Zuschriften Efficient Production of the Liquid Fuel 2 , 5-Dimethylfuran from Fructose Using Formic Acid as a Reagent **, (2010) 6766–6768. https://doi.org/10.1002/ange.201002267.

[17] J. Mitra, X. Zhou, T. Rauchfuss, Pd / C-catalyzed reactions of HMF :, (2015) 307–313. https://doi.org/10.1039/c4gc01520g.

[18] B. Hu, L. Warczinski, X. Li, M. Lu, J. Bitzer, M. Heidelmann, T. Eckhard, Q. Fu, J. Schulwitz, M. Merko, M. Li, W. Kleist, H. Christof, M. Muhler, B. Peng, Catalysis Formic Acid-Assisted Selective Hydrogenolysis of 5-Hydroxymethylfurfural to 2 , 5-Dimethylfuran over Bifunctional Pd Nanoparticles Supported on N-Doped Mesoporous Carbon Research Articles, (2021) 6807–6815. https://doi.org/10.1002/anie.202012816.

[19] P. Wu, D. Zhao, G. Lu, C. Cai, Supported Pd – Au bimetallic nanoparticles as an e ffi cient catalyst for the hydrodeoxygenation of vanillin with formic acid at room temperature †, (2022) 1096–1102. https://doi.org/10.1039/d1gc04240h.

[20] L. Tao, T. Yan, L. Tao, T. Yan, W. Li, Y. Zhao, Q. Zhang, Y. Liu, M.M. Wright, Toward an Integrated Conversion of 5-Hydroxymethylfurfural and Ethylene for the Production of Renewable p -Xylene Toward an Integrated Conversion of 5-Hydroxymethylfurfural and Ethylene for the Production of Renewable p -Xylene, CHEMPR. 4 (n.d.) 2212–2227. https://doi.org/10.1016/j.chempr.2018.07.007.

[21] M. Ribota Peláez, E. Ruiz-López, M.I. Domínguez, S. Ivanova, M.A. Centeno, Formic acid dehydrogenation over a monometallic Pd and bimetallic Pd: Co catalyst supported on activated carbon, Catalysts. 13 (2023) 977. https://doi.org/10.3390/catal13060977.

[22] G.-L. Reactions, M. Mart, S. Ivanova, M.Á. Centeno, Formic Acid Dehydrogenation over Ru- and Pd-Based Catalysts: Gas- vs. Liquid-Phase Reactions, (2023). https://doi.org/10.3390/ma16020472

CHAPTER I:

LITERATURE REVIEW

This chapter presents the use 5-hydroxymethylfurfural (5-HMF) as a platform molecule and a synthesis of all its valorization reactions, in particular, the hydrodeoxygenation reaction using formic acid as hydrogen donor.

I.1. Hydrogen generation from formic acid FA

In the last decades, the continuous restrictions related to climate change and CO_2 emissions have directed the research toward novel, clean and renewable sources able to produce and store energy. As an example, the Liquid Organic Hydrogen Carriers (LOHCs), organic compounds that can reversibly store and release hydrogen through catalytic processes [1]. These systems offer several advantages over the traditional hydrogen storage methods like high energy density, ease of handling, and ability to maintain the existing liquid fuel infrastructure [2]. Among others, formic acid (FA) is considered as promising hydrogen storage agent and versatile C1 building block for many industries [3–5]. FA shows an important volumetric capacity of around 53.4 g/L at hydrogen content of 4.4 wt% [6], converting the molecule in a convenient hydrogen carrier. What is more, FA can be transported to any desired location and decomposed to generate hydrogen under ambient temperature and pressure, thus addressing the challenges associated with the safe storage and transportation of molecular hydrogen (H_2)[7–11]. Although often overlooked as a suitable liquid organic hydrogen carrier, FA is readily used as a hydrogen donor in hydrogenation/hydrodeoxygenation reactions [2,3]. For such a role, FA must dehydrogenate easily and selectively to CO_2 and H_2 (figure I.1), which is the case in aqueous solutions (Eq. (I.1)) but sometimes a side dehydration could appear in other solvents and in gas phase (Eq. (I.2)).

In addition, the resulting gas mixture from formic acid dehydrogenation can be used *in-situ* or even stored and/or recycled [7,8]. This is an industrially important factor that stimulates the move towards the use of formic acid as H-donor for hydrogenation/hydrodeoxygenation reactions.

$$HCOOH \leftrightharpoons CO_2 + H_2 \qquad \text{(Eq. I.1)}$$

$$HCOOH \leftrightharpoons CO + H_2O \qquad \text{(Eq. I.2)}$$

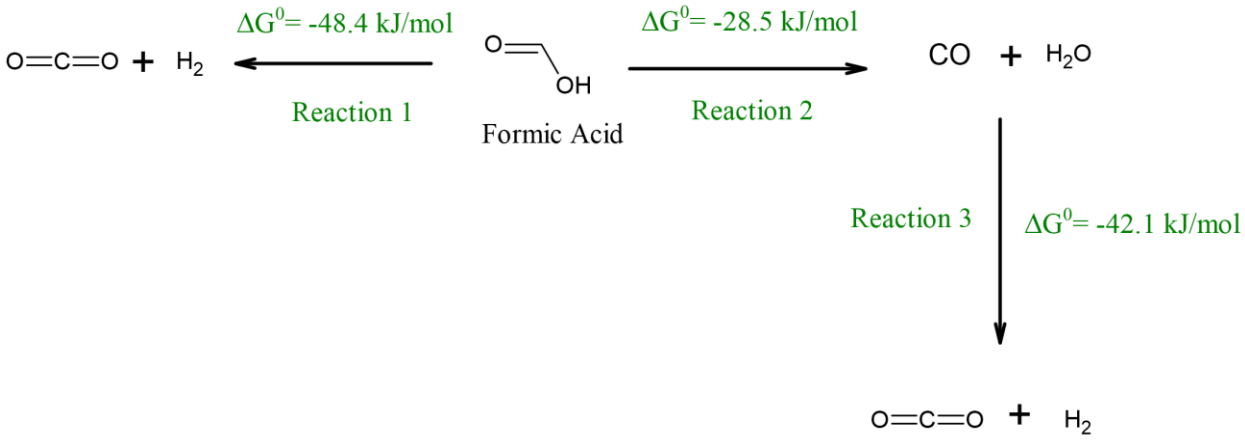

Figure I.1. Formic acid decomposition reaction in gas phase.

I.1.1. Production of formic acid from biomass

Formic acid finds widespread application across multiple industrial sectors, including agriculture, food processing, and the chemical industry, and its prominence has grown considerably with the development of scalable production methods [12]. These methods can be broadly grouped into three categories: methyl formate hydrolysis following methanol carbonylation; CO_2 hydrogenation; and biomass-based conversion routes [13]. Each of these processes carries inherent limitations, including (i) reliance on fossil-derived feedstocks, (ii) formation of undesired by-products, and (iii) requirement for severe operating conditions. These shortcomings have renewed scientific interest in sustainable and green chemistry approaches capable of reducing the environmental footprint of FA production [14–17]. Accordingly, next-generation production technologies should incorporate renewable feedstocks, minimize waste and emissions, and favor the use of more efficient and less hazardous chemical processes. FA production from biomass satisfies all of these criteria [18].

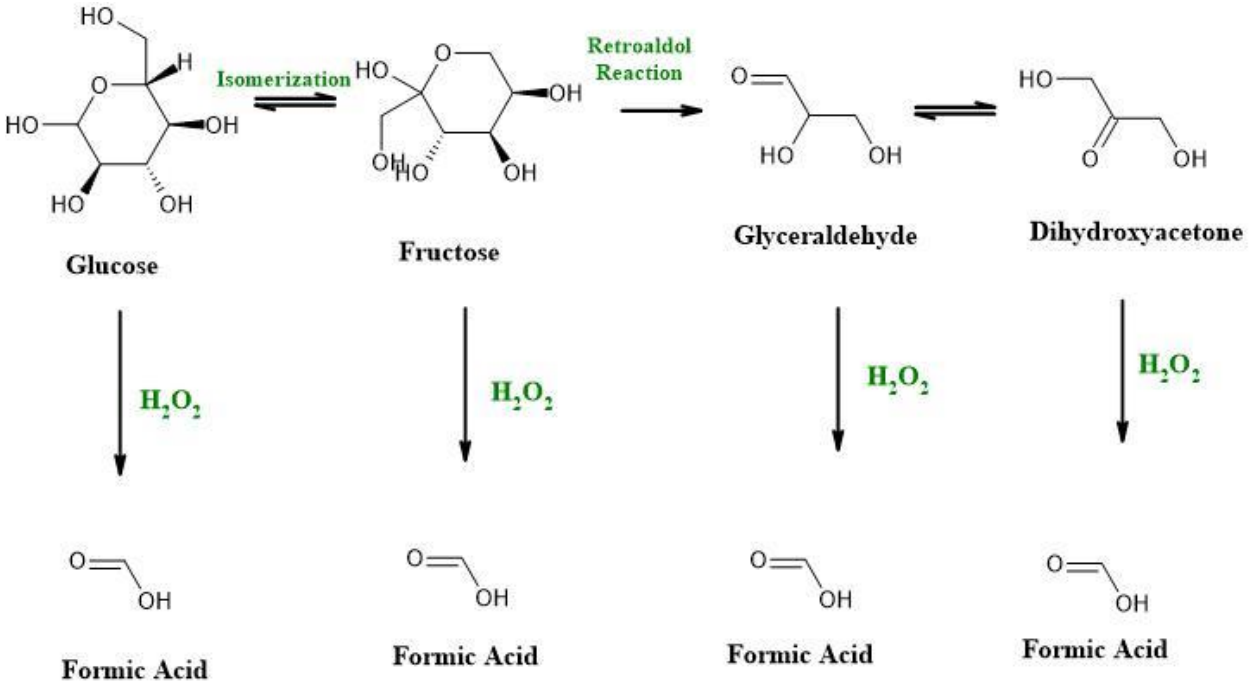

Figure I.2: Formic acid production from glucose and related reactions.

Glucose (GLC) is frequently employed as a model substrate for lignocellulosic biomass (LCB) owing to its predominant abundance in this feedstock. Nevertheless, achieving selective oxidation of glucose remains challenging due to the structural complexity of the molecule and the sensitivity of the reaction to catalyst properties. The selectivity toward formic acid is commonly reduced by the concurrent formation of isomerization products, retro-aldol reaction intermediates, and various C–C cleavage products (Figure I.2). Consequently, the nature of both the oxidant and the catalyst particularly in terms of acidity/basicity or redox behavior plays a pivotal role in attaining high selectivity throughout the conversion process.

I. 1.1.1 Hydrogen peroxide as the oxidant

Aluminium triflate ($Al(OTf)_3$) is a well-established Lewis acid catalyst, recognized for its particular effectiveness in reactions including oxidation that involve water as both reactant and solvent [19]. Kong et al. [20] employed this catalyst for the conversion of glucose to formic acid under mild conditions (70°C, 12 h), using a GLC-to-oxidant (H_2O_2) molar ratio of 1:10 and acetonitrile as an additive. While a relatively high glucose conversion of 85% was achieved, the FA yield remained very low at 6.8%. Takagaki and co-workers [21] demonstrated that alkaline metal oxides exhibit good catalytic activity in the oxidative conversion of glucose to formic acid,

attributing this behavior to the basicity of the solid surface. Wu et al.[22] investigated MgO as a catalyst and reported a high FA yield of 78% with 90% glucose conversion under mild conditions (50°C, 4 h) using a stoichiometric GLC/H_2O_2 ratio. Nevertheless, undesired by-products such as lactic acid and arabinose were also observed. The catalytic activity of MgO was maintained over up to five consecutive cycles, though calcination between cycles was necessary to regenerate the catalyst.

Kılıç et al.[23] examined hydrotalcite-like materials as catalysts for GLC oxidation to FA in ethanol, with particular attention to the effect of the Mg/Al ratio. No significant differences in activity were observed among the uncalcined materials, but post-treatment calcination revealed enhanced conversion at higher Mg/Al ratios.

Yuan et al. [24] investigated a novel silica-encapsulated heteropolyacid (HPA) catalyst for the oxidation of several biomass-derived platform molecules. Although HPAs are known for their strong redox properties, their low surface area and high solubility in polar solvents represent significant drawbacks for this application. Encapsulation within a silica matrix was proposed to address these limitations, resulting in glucose conversions approaching 25% and an improved FA selectivity of 67%.

I. 1.1.2. Molecular oxygen as the oxidizing agent

Albert [25] reported a series of heteropolyacids (HPAs) with varying vanadium-to-molybdenum ratios within the Keggin structure. The highest FA yield of 26% was achieved with the HPA-4 sample ($H_7PV_4Mo_8O_{40}$) at 90°C under 20 bar O_2 pressure after 8 h of reaction. The authors concluded that a minimum of two vanadium atoms within the polyoxometalate framework is required for FA production. Maerten et al. [26] also studied HPA-5 in aqueous medium at 90°C and 20 bar O_2, reporting a FA yield of 55% alongside a CO_2 yield of 45%. Switching the solvent to ethanol resulted in complete selectivity toward methyl formate. A ^{13}C-labelled glucose study confirmed that formic acid originates from the glucose molecule itself rather than from oxidation or esterification of the solvent. This work also proposed a reaction mechanism for glucose oxidation in ethanol, involving sequential C–C cleavage steps: erythrose is formed in the first step, followed by further C–C bond breaking to yield glyoxal and glycolaldehyde. These two-carbon intermediates are subsequently oxidized to formic acid, which rapidly undergoes esterification to form methyl formate (Figure I.3). No other intermediates or CO_2 were detected in this system.

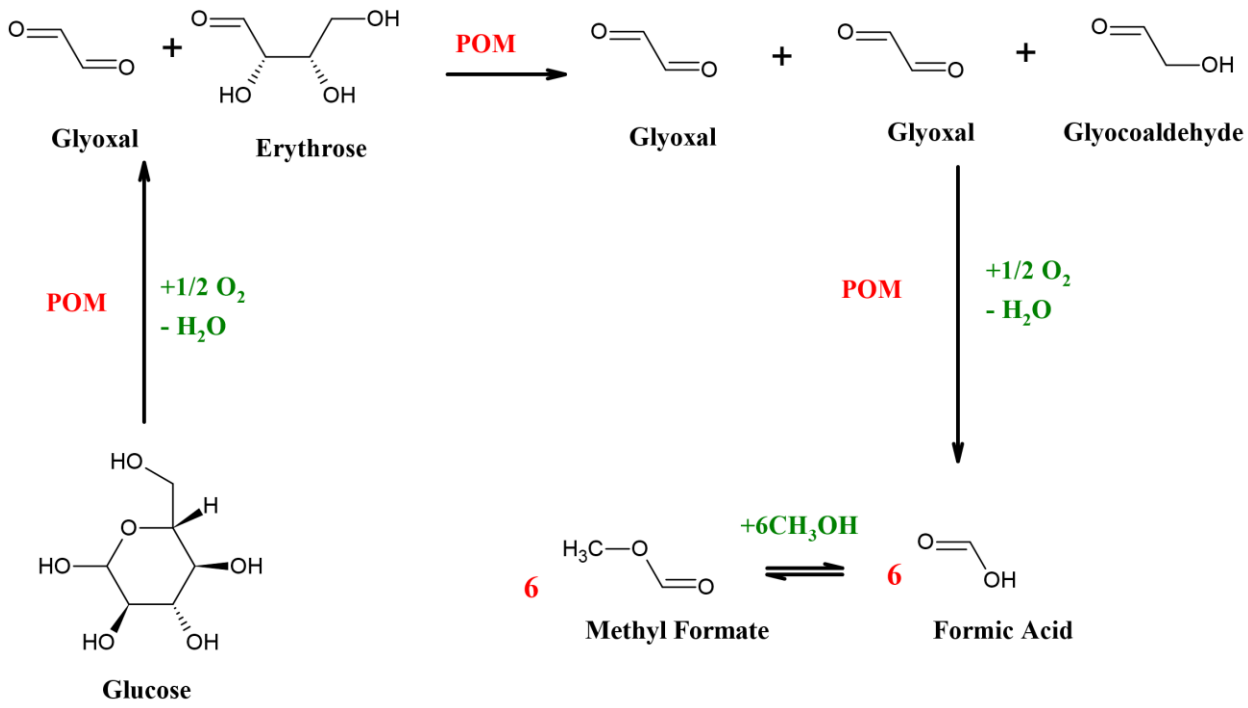

Figure I.3: Glucose oxidation in methanol over polyoxymethylene (POM) based catalysts [27]

Albert et al. [28] further investigated the role of vanadium species in glucose transformation by employing two commercial catalysts NH_4VO_3 (V^{5+} source) and $VOSO_4$ (V^{4+} source) alongside two HPAs, HPA-1 ($H_4PV_1Mo_{11}O_{40}$) and HPA-5, at 90°C and 20 bar O_2. At shorter reaction times (3 h), only HPA-5 displayed significant activity, yielding approximately 34% FA. Iron and manganese compounds have been explored as alternatives to vanadium-based systems. Hou et al. [29] proposed a mixture of iron (III) chloride and sulfuric acid ($FeCl_3$–H_2SO_4) as catalyst, conducting the reaction at 170°C and 30 bar O_2 for 50 min. Full glucose conversion was achieved with a FA yield of 53% in the liquid phase, accompanied by CO_2 production. Acetic acid and glycolic acid were identified as secondary products. The proposed mechanism involves glucose oxidation coupled with the reduction of Fe^{3+} to Fe^{2+}, which is subsequently re-oxidized by molecular oxygen.

All systems described above operate under homogeneous conditions. The use of manganese oxides, however, represents a transition toward heterogeneous catalysis. Li et al. [30] evaluated three manganese oxide materials, finding the highest FA yield of 81% for the MnO_x-100 sample prepared hydrothermally at 100 °C and tested at 160 °C, 30 bar O_2, over 2.5 h. A comprehensive summary of all discussed studies, including catalyst types, solvents, and reaction conditions, is provided in Table I.1.

The oxidative conversion of glucose to formic acid remains a formidable challenge from a heterogeneous catalysis standpoint. To date, stable heterogeneous catalytic systems are still lacking, and the most promising active species identified are based on vanadium, manganese, and molybdenum. It is worth noting that formic acid is also generated as a by-product during the synthesis of levulinic acid from biomass.

Table I.1: Overview of the catalytic systems used for formic acid production from glucose.

Catalyst	Solvent	Oxidant	Conversion %	Yield %	Time (h)	Temp (◦C)	ref
$Al(OTf)_3$	water	H_2O_2	85	6.8	12	70	[20]
CaO	water	H_2O_2	100	45	0.5	70	[21]
MgO	water	H_2O_2	90.5	78.6	4	50	[22]
HPA@SiO_2–S–N_2	ethanol	H_2O_2	78	-	12	70	[24]
hydrotalcite	ethanol	H_2O_2	38.7	5	6	70	[23]
Mg–Al oxide	water	H_2O_2	62	10.2	6	70	[31]
HPA-4	water	O_2	-	25.6	8	90	[25]
HPA-5	water	O_2	53.2	37.8	8	80	[26]
HPA-5	water	O_2	100	55	24	90	[27]
HPA-5	water	O_2	43	34.3	3	90	[28]
HPA-2	50% v/v (Glucose/ MeOH)	O_2	100	25	0.17	160	[32]
HPA-3	water	O_2	100	36	1	160	[33]
$FeCl_3$–H_2SO_4	water	O_2	100	53	0.83	170	[29]
MnO_x-100	water	O_2	100	81.1	2.5	160	[30]
$Mn_4Ce_{0.05}O_x$	water	O_2	-	63.4	3.5	160	[34]
Mn–Mo oxide	water	O_2	100	79	1.5	160	[35]

I.2. Production and valorization of 5-hydroxymethylfurfural HMF as a platform chemical

I. 2.1 HMF as a versatile platform chemical

HMF (Figure I.4) is a multifunctional molecule because it is at the same time an aromatic aldehyde, an aromatic alcohol and a furan ring system. HMF is a versatile platform chemical that can be

further transformed into a high value-added chemical. For these reasons it has been called a "sleeping giant" in the field of intermediate chemicals from bio-based feedstocks [36].Unfortunately, HMF is not stable for long periods and therefore it cannot be stored for extended periods. Furthermore, a high HMF purity is essential even for storage over short time periods because even small impurities promote rapid aging due to dimer and oligomer formation [37].

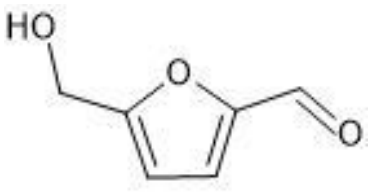

Figure I.4. 5-hydroxymethylfurfural (HMF) structure.

In principle, HMF synthesis appears straightforward, as it is produced via the acid-catalyzed triple dehydration of a hexose substrate; however, the reaction is considerably more complex in practice due to numerous competing pathways occurring simultaneously. From a mechanistic standpoint, the conversion of carbohydrates to HMF proceeds through a three-step sequence (Figure I.5): (i) Brønsted acid-catalyzed hydrolysis of glucan polysaccharides (e.g., cellulose or starch) to glucose monomers; (ii) Lewis acid-mediated isomerization of glucose to fructose; and (iii) Brønsted acid-catalyzed sequential dehydration of fructose through the elimination of three water molecules t o yield HMF. In parallel, several side reactions significantly reduce HMF yield, most notably the rehydration of HMF to levulinic acid and formic acid in equimolar quantities, as well as condensation and cross-polymerization reactions leading to insoluble humins. Therefore, maximizing HMF yield requires the simultaneous promotion of the desired reaction pathway and suppression of these competing processes through the judicious selection of reaction conditions and an appropriately tailored catalytic system.

HMF can be obtained not only from fructose, sucrose and inuline [38–41], but also from glucose via isomerisation to fructose [42–45], from polysaccharides (inulin, starch, or cellulose) [46–49] and directly from real biomasses too.

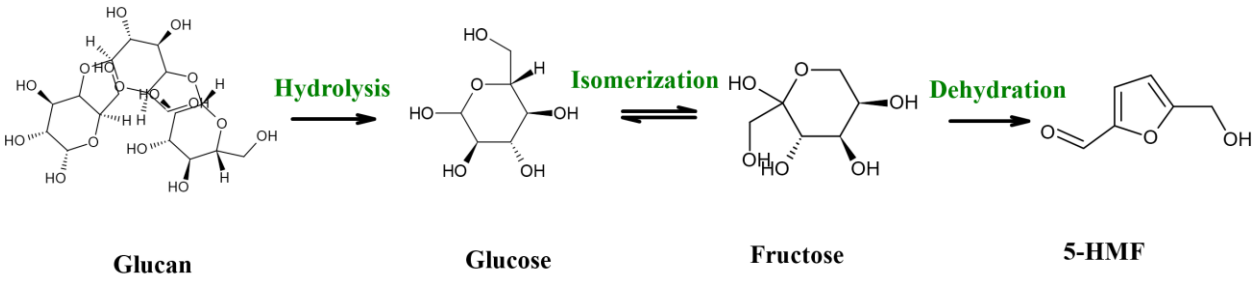

Figure I.5. Schemes of the reaction steps from glucan to HMF.

The direct use of real biomass can indeed lead to less energy consumption and less CO_2 emissions. In practice, using a raw plant biomass avoid the pretreatment steps that are required in preparing the purified bio-based feedstocks. Most studies have still focused on using feedstocks exhibiting simple and regular molecular structures, due to their easier catalytic mechanisms. However, from the viewpoint of practical applications, direct conversion of real biomass is highly desirable because they are the ideal feedstock to be used for any commercial unit to economically produce bio-based products. The first studies regarded edible biomasses, but for these there are very strong socio and economic issues and therefore the use of edible feedstocks appears unsustainable. The upgrading of lignocellulosic biomass wastes (e.g., wood, straw, energy crops, etc.) is a good opportunity because they avoid competition with the food sector and usually do not require as much as land to grow [50]. On the other hand, food wastes represent a massive annual dissipation of resources and incurs a high carbon footprint, as every year, the food chain results in large amounts of wastes and their valorization attracts great attention. The generation of commercial and industrial food wastes shows a growing trend globally.

I. 2.2 HMF valorization

HMF is a versatile platform chemical that can be converted into a broad spectrum of value-added products, including levulinic acid [51] , 2,5-furandicarboxylic acid (FDCA) [52], ethyl levulinate [53], and 2,5-dimethylfuran (DMF)[54]. However, HMF is an inherently unstable molecule, prone to participating in undesired side reactions that generate various by-products alongside the intended transformation products [55,56]. Selective conversion of HMF to value-added chemicals therefore requires carefully designed catalysts operating through CTH, HDO, or hydrogenolysis pathways using formic acid. A prime example is the selective hydrodeoxygenation of HMF to DMF [57] , a molecule that exhibits highly attractive physicochemical properties for use as a liquid transportation biofuel: a volumetric energy density of 30.0 MJ/L closely comparable to that of

gasoline a near-optimal boiling point, full miscibility with gasoline, and immiscibility with water. DMF has already been successfully tested in combustion engines [58], and can additionally serve as a feedstock for the production of p-xylene via the Diels–Alder reaction [59]. The reductive upgrading of HMF to DMF is therefore expected to play a central role in the future production of liquid fuels and chemicals from biomass. Ongoing studies exploring the use of pure DMF, DMF/gasoline blends, and DMF/diesel mixtures are aimed at characterizing their combustion and emission profiles for potential application in internal combustion engines [60–62]. Complete hydrogenation of HMF can further yield 2,5-bis(hydroxymethyl)tetrahydrofuran (BHTF) [63], an important intermediate in the production of resins, crown ethers, and heat-insulating materials [64–66]. BHTF is also a promising diol for the synthesis of shape-memory and self-healing polymers, as well as 1,6-hexanediol, another key polymer precursor [67].

Two distinct reaction pathways have been identified for DMF synthesis from HMF (Figure I.6). In the first pathway, HMF undergoes hydrogenolysis to 5-methylfurfural (5-MF), which is subsequently hydrogenated to 2-hydroxymethyl-5-methylfuran (HMMF); the latter is then converted to DMF via hydrogenolysis of its carbonyl group. In the second pathway, HMF is first hydrogenated to 2,5-bis(hydroxymethyl)furan (BHMF), which undergoes hydrogenolysis to HMMF and is subsequently transformed into DMF.

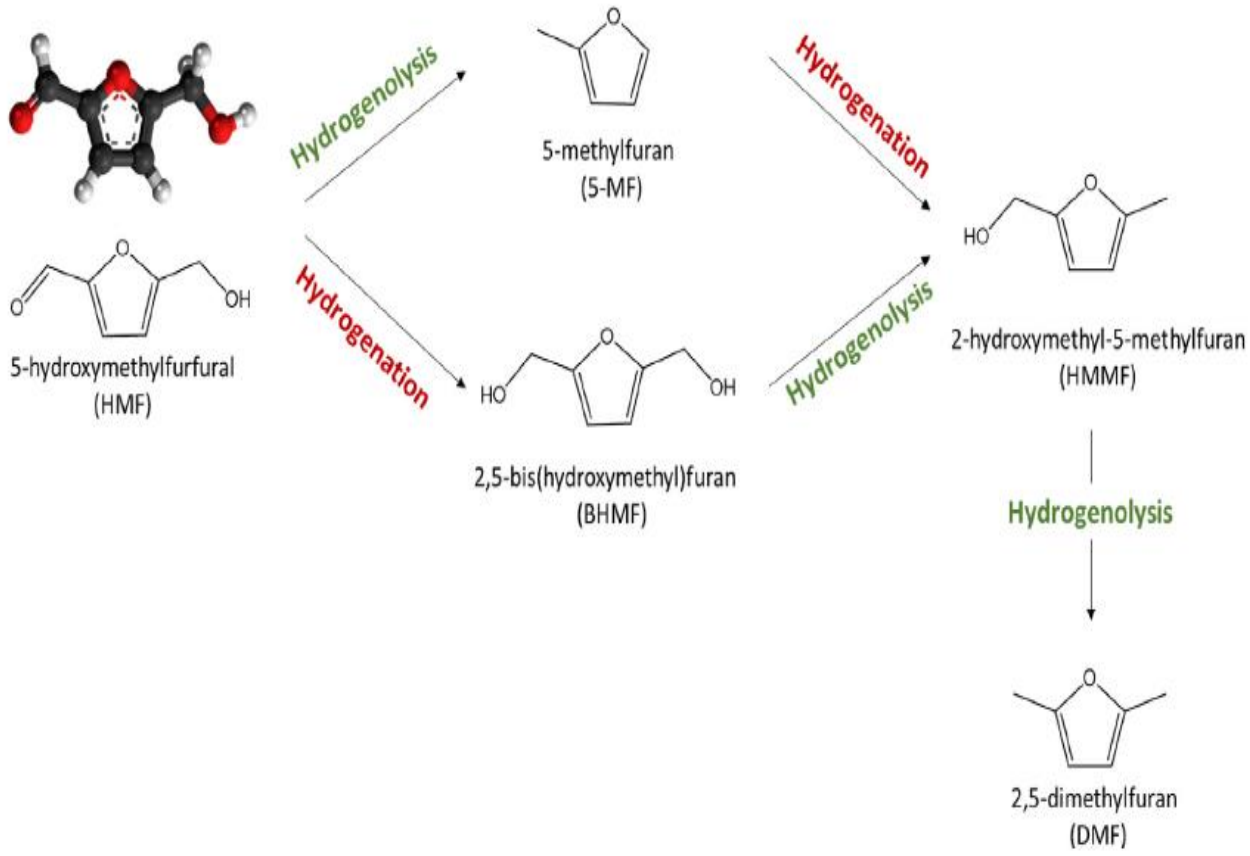

Figure I.6: Catalytic hydrogenation/hydrogenolysis of 5-HMF to 2,5-DMF.

The synthesis of DMF therefore requires hydrogenation/hydrodeoxygenation catalysts capable of activating in-situ hydrogen production from formic acid. Mitra et al. [63] investigated the HDO of HMF to DMF using FA as hydrogen donor over a Pd/C catalyst, achieving 95% HMF conversion and 95% DMF yield at 120°C after 15 h in dioxane as solvent. The same catalyst was subsequently evaluated in a THF/H_2SO_4 mixture [68], delivering complete HMF conversion and 95% DMF yield after 5 h at 110°C.

Bifunctional Pd nanoparticles supported on nitrogen-doped mesoporous carbon (Pd/NMC) have also been reported [69], yielding 61% HMF conversion and 39% DMF yield. The nitrogen content was found to play a promotional role, as the nitrogen-free mesoporous carbon-supported counterpart (Pd/CMC) reached only 21% HMF conversion and 13% DMF yield under the same conditions (160°C, 3 h, THF solvent). Both catalysts showed a marked improvement in activity when FA was combined with gaseous H_2: Pd/NMC achieved complete HMF conversion and 97% DMF yield, while Pd/CMC delivered 99% HMF conversion and 72% DMF yield.

Pd–Au/g-C_3N_4 has also been investigated [70], demonstrating good activity with an 86% DMF yield obtained in a water/ethyl acetate mixture after 1 h at room temperature. The same metal combination supported on zirconia was studied by Tao et al. [71] in 1,4-dioxane, achieving 99% HMF conversion and 98% DMF yield after 1.5 h at 140°C.

Among non-noble metal systems, the CoFe-111 catalyst [72] delivered a notable DMF yield of 90% with high HMF conversion under optimized conditions (240°C, 2 h, THF medium), along with good stability over four runs without significant activity loss. Yang et al. [73] investigated the bimetallic Ni–Co/C system, finding that a 2%Ni–20%Co/C catalyst achieved 99% HMF conversion and 90% DMF yield accompanied by some 5-MF in THF at 210°C after 24 h. Under the same conditions using molecular hydrogen, DMF yield dropped substantially to 61%. The formation of 2,5-hexanediol was also observed, increasing with higher nickel loadings and reaching 20% for the 7%Ni catalyst. Recyclability tests showed consistent HMF conversion over four cycles, but a gradual shift in selectivity away from DMF toward 5-MF, attributed to metal leaching. The bimetallic Ni–Cu/C system has also been evaluated [74]; a 10%Ni–10%Cu/C catalyst prepared by incipient wetness impregnation achieved complete HMF conversion and 80% DMF yield after 6 h at 200°C in isopropanol.

The catalytic transfer hydrogenation of HMF to BHMF was explored by Thananatthanachon et al. [75] using FA as hydrogen donor (HMF/FA = 1, in 5 mL THF, 40°C) over 0.1 mol% of a Ru catalyst ((cymene)Ru(TsDPEN)) and 0.5 mol% of an iridium catalyst (Cp*Ir(TsDPEN-H)) (Scheme I.8). Both catalysts achieved 99% BHMF yield within 1 to 2 h of reaction. The Ir-based catalysts were also found to be active in the upgrading of furfural (FF) to furfuryl alcohol (FFA) using formic acid as hydrogen donor, in the presence of 10 equivalents of Et_3N (6 h, 150°C, 0.1 eq. FA).

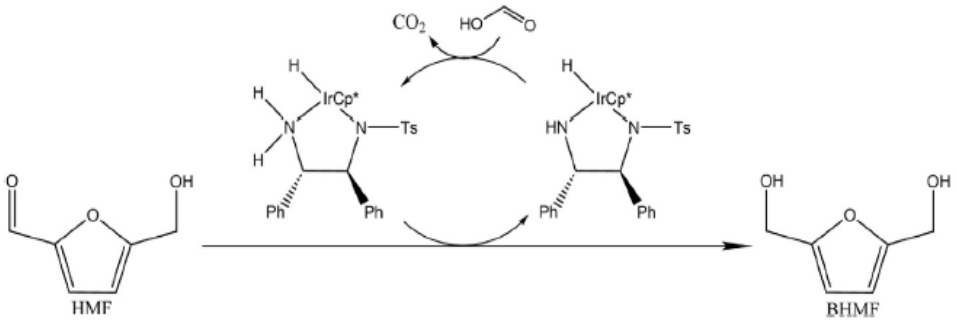

Figure I.8: CTH process of HMF using Cp*Ir(TsDPEN) catalyst with formic acid as hydrogen source [75].

The CTH reduction of HMF to 2,5-furandimethanol (FDM) is recognized as a valuable pathway for the production of building blocks for the biopolymer industry and macromolecular synthesis [76,77]. Xu et al. [78]reported this reaction over a stable cobalt-confined catalyst supported on mesoporous nitrogen-doped carbon (Co–NC-A), achieving 88% HMF conversion and 86% FDM yield at 160°C after 5 h in 1,4-dioxane. In a related study, Tuteja et al [79] investigated a palladium-supported zirconium phosphate catalyst (Pd/ZrP) for the hydrogenolysis of HMF to 1,6-hexanediol using formic acid as hydrogen donor and ethanol as solvent. The highest 1,6-hexanediol yield of 42.5% was obtained over a 7 wt% Pd/ZrP catalyst with near-complete HMF conversion after 21 h at 140°C.

Table I.2: Formic acid as hydrogen donor in the catalytic transfer hydrogenation of HMF.

Desired Product[b]	Solvent[a]	Catalysts[b]	Conversion[c] (%)	Yield (%)	Time (h)	Temperature (°C)	Ref
DMF	DO	Pd/C	95	95	15	120	[63]
DMF	THF + H_2SO_4	Pd/C	100	95	15	110	[68]
DMF	-	Pd/NMC	60.8	39.1	3	160	[69]
DMF	-	Pd/CMC	62.9	13.5	3	160	[69]
DMF	H_2O/EA	Pd-Au/g-C_3N_4	-	99	1	RT[h]	[70]
DMF	DO	Au–Pd/t-ZrO_2	99	98	1.5	140	[71]
DMF	THF	48Ni/SBA-15	100	58.8	5	220	[80]
DMF	THF	CoFe-111	100	92	2	240	[72]
DMF	THF	Ni–Co/C	99	90	24	210	[81]
DMF	i-PrOH	Ni–Cu/C	100	80	6	200	[74]
HDO	EtOH	$Pd/ZrPO_4$	97	43	21	140	[82]
FDM	i-PrOH	Co–NC-A	88.2	86.0	5	160	[78]
BHMF	THF	Cp*Ir(TsDPEN)	100	99	2	40	[78]
DMF	(THF)	Ni-Cu/SBA-15	100	71	5	220	[80][d]

[a] **DMF**: 2,5-dimethylfuran, **HDO**: 1,6-hexanediol, **FDM**: 2,5-furandimethanol, **BHMF**: 2,5-bis(hydroxymethyl)furan.
[b] **NMC**: N-doped mesoporous carbon, **CMC**: N-free mesoporous carbon, g-**C_3N_4**: graphitic carbon nitride.
[c] **DO**: 1,4-dioxane, **THF**: Tetrahydrofuran, **H_2SO_4**: sulfuric acid, **EA**: Ethyl acetate, **i-PrOH** isopropanol, **EtOH:** ethanol.
[d] **FMF**: 5-formyloxymethylfurfural was used as substrate in this work.

5-Formyloxymethylfurfural (FMF) is another furan compound structurally analogous to HMF, in which the hydroxyl group (–OH) is replaced by a formyloxy group (–OOCH). It is produced from HMF and chloromethyl furfural (CMF) [83,84] and can likewise serve as a precursor for DMF synthesis. FMF possesses several advantageous properties including low polarity, high chemical stability, and enhanced hydrophobicity that facilitate its separation from the reaction mixture by vacuum distillation [84–86]. Sun et al. [80] studied the hydrogenolysis and hydrogenation of both HMF and FMF with formic acid to produce DMF in THF solvent over monometallic Ni and bimetallic Ni–Cu/SBA-15 catalysts. Using FMF as the substrate afforded higher DMF yields within 5 h at 220°C compared to HMF, though a slight decline in DMF selectivity was observed after six consecutive reaction runs. A comprehensive summary of the described catalytic systems, reaction conditions, and results is provided in Table I.3.

I.3. Research aims

Biomass upgrading reactions involving hydrogen are of paramount importance for sustainable development, particularly in the context of biofuel and fuel additive production. The future viability of biorefineries depends on the efficient removal of oxygen from bio-derived molecules and on the availability of previously or in-situ generated green hydrogen. In this regard, liquid organic hydrogen carriers represent an attractive strategy for generating and utilizing hydrogen in-situ, circumventing the logistical challenges associated with H_2 gas transport and storage. Formic acid stands out as an excellent liquid organic carrier for biorefinery applications involving H_2, owing to its high volumetric hydrogen storage capacity, relatively low dehydrogenation temperature, and ability to participate directly as a hydrogen donor in catalytic transfer hydrogenation reactions.

The main objective of this thesis is to develop effective heterogeneous catalysts for the hydrodeoxygenation of 5-hydroxymethylfurfural (5-HMF) into valuable biofuel molecule, the 2,5-dimethylfuran (DMF) using formic acid as a hydrogen donor. This approach combines the conversion of biomass-derived compounds with the in-situ generation of hydrogen from formic acid, avoiding the use of external molecular hydrogen. The study focuses on designing catalysts with suitable metal composition and support properties to achieve high activity, good selectivity, and stable performance.

References

[1] M. Zhou, Y. Miao, Y. Gu, Y. Xie, Recent advances in reversible liquid organic hydrogen carrier systems: From hydrogen carriers to catalysts, Adv. Mater. 36 (2024) 2311355.

[2] F. Ammari, S. Ivanova, M. Angel, Tetrahedron Green Chem Formic acid as renewable reagent and product in biomass upgrading, 2 (2023). https://doi.org/10.1016/j.tgchem.2023.100020.

[3] M.J. Gilkey, B. Xu, Heterogeneous Catalytic Transfer Hydrogenation as an E ff ective Pathway in Biomass Upgrading, 5 (2016). https://doi.org/10.1021/acscatal.5b02171.

[4] R. Sun, Y. Liao, S. Bai, Environmental Science Heterogeneous catalysts for CO_2 hydrogenation to formic acid / formate : from nanoscale to, (2021) 1247–1285. https://doi.org/10.1039/d0ee03575k.

[5] K. Yang, J. Jiang, Computational design of a metal-based frustrated hydrogenation to methanol, (2020) 22802–22815. https://doi.org/10.1039/d0ta07051c.

[6] G. Peng, S.J. Sibener, G.C. Schatz, M. Mavrikakis, Surface Science CO_2 hydrogenation to formic acid on Ni (110), Surf. Sci. 606 (2012) 1050–1055. https://doi.org/10.1016/j.susc.2012.02.027.

[7] H. Li, D. Song, X. Wang, X. Li, G. Lei, Recent progress on heterogeneous catalytic formic acid decomposition for hydrogen production, Fuel. 383 (2025) 133824. https://doi.org/10.1016/j.fuel.2024.133824.

[8] S. Zhou, X. Sun, Q. Yao, M. Huang, L. Zhang, Z. Lu, International Journal of Hydrogen Energy Porous carbon-confined palladium nanoclusters for selective dehydrogenation of formic acid and hexavalent chromium reduction, Int. J. Hydrogen Energy. 104 (2025) 59–65. https://doi.org/10.1016/j.ijhydene.2024.05.143.

[9] H. Jung, S. Lee, J. Yang, S. Hyuk, H. Sook, Bioresource Technology Exploration of formate as a liquid organic hydrogen carrier in biohydrogen production through evolutionary and process engineering of hyperthermophilic archaeon, Bioresour. Technol. 425 (2025) 132318. https://doi.org/10.1016/j.biortech.2025.132318.

[10] H. Li, Y. Gui, J. Zhang, J. Li, Biomass and Bioenergy Simultaneous alkali / air activation for hierarchical pore development in biochar and its use as catalyst carrier for formic acid

dehydrogenation, Biomass and Bioenergy. 193 (2025) 107549. https://doi.org/10.1016/j.biombioe.2024.107549.

[11] S. Vasu, R.K. Rahman, R. Iyer, S. Freund, K. Wygant, energy carriers, Elsevier Inc., 2025. https://doi.org/10.1016/B978-0-443-21893-4.00003-9.

[12] Y. Hou, M. Niu, W. Wu, Catalytic Oxidation of Biomass to Formic Acid Using O_2 as an Oxidant, (2020). https://doi.org/10.1021/acs.iecr.0c01088.

[13] W.E.R. Eutemann, B. Aktiengesellschaft, F. Republic, Formic Acid, Ullmann's Encyclopedia of Industrial Chemistry. https://doi.org/10.1002/14356007.a12.

[14] Y. Lee, Y. Yu, H. Tanaya, J. Theerthagiri, S. Jun, A. Min, G. Kim, H. Chul, M. Yong, Pulsed laser-driven green synthesis of trimetallic AuPtCu nanoalloys for formic acid electro-oxidation in acidic environment, Fuel. 332 (2023) 126164. https://doi.org/10.1016/j.fuel.2022.126164.

[15] X. Wei, Y. Li, L. Chen, J. Shi, Formic Acid Electro-Synthesis by Concurrent Cathodic CO_2 Reduction and Anodic CH_3OH Oxidation Research Articles, (2021) 3148–3155. https://doi.org/10.1002/anie.202012066.

[16] P. Sarkar, S. Riyajuddin, A. Das, A. Hazra, K. Ghosh, S. Manirul, Mesoporous covalent organic framework : An active photo-catalyst for formic acid synthesis through carbon dioxide reduction under visible light, Mol. Catal. 484 (2020) 110730. https://doi.org/10.1016/j.mcat.2019.110730.

[17] S. Chatterjee, I. Dutta, K. Huang, Environmental Science Enabling storage and utilization of low-carbon electricity : power to formic acid, 1 (2021) 1194–1246. https://doi.org/10.1039/d0ee03011b.

[18] P.K. Sahoo, T. Zhang, S. Das, Oxidative Transformation of Biomass into Formic Acid, (2020) 1331–1343. https://doi.org/10.1002/ejoc.202001514.

[19] J. Dai, L. Peng, H. Li, Intensi fi ed ethyl levulinate production from cellulose using a combination of low loading H_2SO_4 and Al (OTf)$_3$, Catal. Commun. 103 (2018) 116–119. https://doi.org/10.1016/j.catcom.2017.10.007.

[20] K. Kong, D. Li, W. Ma, Q. Zhou, G. Tang, Z. Hou, Aluminum (III) triflate-catalyzed selective oxidation of glycerol to formic acid with hydrogen peroxide, Chinese J. Catal. 40

(2019) 534–542. https://doi.org/10.1016/S1872-2067(19)63319-X.

[21] A. Takagaki, W. Obata, T. Ishihara, Oxidative Conversion of Glucose to Formic Acid as a Renewable Hydrogen Source Using an Abundant Solid Base Catalyst, (2021) 954–959. https://doi.org/10.1002/open.202100074.

[22] L. Wu, Y. Yang, J. Cheng, X. Shi, H. Zhong, F. Jin, Highly Efficient Conversion of Carbohydrates into Formic Acid with a Heterogeneous MgO Catalyst at Near-Ambient Temperatures, (2022). https://doi.org/10.1021/acssuschemeng.2c04502.

[23] H.A. Kılıç, E. Kılıç, L. Erden, Y. Gök, Highly selective oxidation of glucose to formic acid over synthesized hydrotalcite - like catalysts under base free mild conditions, Res. Chem. Intermed. 48 (2022) 4079–4103. https://doi.org/10.1007/s11164-022-04811-9.

[24] Y. Mingming, L.I. Difan, Z. Xiuge, M.A. Wenbao, K. Kang, N.I. Wenxiu, G.U. Qingwen, Selective Oxidation of Glycerol with Hydrogen Peroxide Using Silica- Encapsulated Heteropolyacid Catalyst, 34 (2018) 886–895. https://doi.org/10.3866/PKU.WHXB201711151.

[25] J. Albert, Selective oxidation of lignocellulosic biomass to formic acid and high-grade cellulose using tailor-made polyoxometalate catalysts, (2017) 99–109. https://doi.org/10.1039/c7fd00047b.

[26] S. Maerten, C. Kumpidet, D. Voß, A. Bukowski, P. Wasserscheid, J. Albert, formate in perfect selectivity †, (2020) 4311–4320. https://doi.org/10.1039/d0gc01169j.

[27] T. Lu, Y. Hou, W. Wu, M. Niu, S. Ren, Z. Lin, V.K. Ramani, Catalytic oxidation of biomass to oxygenated chemicals with exceptionally high yields using $H_5PV_2Mo_{10}O_{40}$, Fuel. 216 (2018) 572–578. https://doi.org/10.1016/j.fuel.2017.12.044.

[28] J. Albert, M. Mendt, M. Mozer, D. Voß, Applied Catalysis A , General Explaining the role of vanadium in homogeneous glucose transformation reactions using NMR and EPR spectroscopy, Appl. Catal. A, Gen. 570 (2019) 262–270. https://doi.org/10.1016/j.apcata.2018.10.030.

[29] Y. Hou, Z. Lin, M. Niu, S. Ren, W. Wu, Conversion of Cellulose into Formic Acid by Iron (III)-Catalyzed Oxidation with O_2 in Acidic Aqueous Solutions, (2018). https://doi.org/10.1021/acsomega.8b01409.

[30] J. Li, L. Smith, Manganese oxide as an alternative to vanadium- based catalysts for e ff ective conversion of glucose to formic acid in water, (2022) 315–324. https://doi.org/10.1039/d1gc03637h.

[31] H.A. Kılıç, Y. Gök, Selective glucose oxidation to organic acids over synthesized bimetallic oxides at low temperatures, React. Kinet. Mech. Catal. 136 (2023) 267–286. https://doi.org/10.1007/s11144-022-02342-3.

[32] J. Reichert, J. Albert, Detailed Kinetic Investigations on the Selective Oxidation of Biomass to Formic Acid (OxFA Process) Using Model Substrates and Real Biomass, (2017). https://doi.org/10.1021/acssuschemeng.7b01723.

[33] D. Voß, R. Dietrich, M. Stuckart, J. Albert, Switchable Catalytic Polyoxometalate-Based Systems for Biomass Conversion to Carboxylic Acids, (2020). https://doi.org/10.1021/acsomega.0c02430.

[34] S. Xu, J. Yang, J. Li, F. Shen, Siyu Xu, Jirui Yang, Jialu Li, and Feng Shen *, (2023). https://doi.org/10.1021/acssuschemeng.2c04940.

[35] H. Guo, J. Li, S. Xu, J. Yang, G. Chong, F. Shen, Mo-modified MnO x for the efficient oxidation of high-concentration glucose to formic acid in water, Fuel Process. Technol. 242 (2023) 107662. https://doi.org/10.1016/j.fuproc.2023.107662.

[36] M. Bicker, J. Hirth, H. Vogel, Dehydration of fructose to 5-hydroxymethylfurfural in sub- and supercritical acetone, (2003) 280–284. https://doi.org/10.1039/b211468b.

[37] J. Artz, R. Palkovits, ScienceDirect Cellulose-based platform chemical : The path to application, Curr. Opin. Green Sustain. Chem. 14 (2018) 14–18. https://doi.org/10.1016/j.cogsc.2018.05.005.

[38] Æ.J.A. Dumesic, Solvent Effects on Fructose Dehydration to 5-Hydroxymethylfurfural in Biphasic Systems Saturated with Inorganic Salts, (2009) 297–303. https://doi.org/10.1007/s11244-008-9166-0.

[39] C. Moreau, A. Finiels, L. Vanoye, Dehydration of fructose and sucrose into 5-hydroxymethylfurfural in the presence of 1-H-3-methyl imidazolium chloride acting both as solvent and catalyst, 253 (2006) 165–169. https://doi.org/10.1016/j.molcata.2006.03.046.

[40] H. Zhao, Metal Chlorides in Ionic Liquid Solvents Convert Sugars to 5-Hydroxymethylfurfural, 1597 (2014). https://doi.org/10.1126/science.1141199.

[41] C. Eddine, C. Megías-sayago, S. Ivanova, A. Penkova, F. Ammari, M. Angel, J. Antonio, Applied Catalysis A , General Effect of the sulphonating agent on the catalytic behavior of activated carbons in the dehydration reaction of fructose in DMSO, Appl. Catal. A, Gen. 617 (2022) 118108. https://doi.org/10.1016/j.apcata.2021.118108.

[42] J.M.R. Gallo, D.M. Alonso, M.A. Mellmer, J.A. Dumesic, Production and upgrading of 5-hydroxymethylfurfural using heterogeneous catalysts and biomass-derived solvents, (2013) 85–90. https://doi.org/10.1039/c2gc36536g.

[43] R. Huang, W. Qi, R. Su, Z. He, Integrating enzymatic and acid catalysis to convert glucose into 5-hydroxymethylfurfural w, (2010). https://doi.org/10.1039/b921306f.

[44] J.B. Binder, R.T. Raines, Simple Chemical Transformation of Lignocellulosic Biomass into Furans for Fuels and Chemicals, (2009) 1979–1985. https://doi.org/10.1021/ja808537j

[45] M.E. Zakrzewska, E. Bogel-łukasik, R. Bogel-łukasik, Ionic Liquid-Mediated Formation of 5-Hydroxymethylfurfural s A Promising Biomass-Derived Building Block, (2011) 397–417. https://doi.org/10.1021/cr100171a

[46] X. Qi, M. Watanabe, T.M. Aida, R.L. Smith, Fast Transformation of Glucose and Di- / Polysaccharides into 5-Hydroxymethylfurfural by Microwave Heating in an Ionic Liquid / Catalyst System, 8579 (2010) 1071–1077. https://doi.org/10.1002/cssc.201000124.

[47] C. Li, Z. Zhang, Z.K. Zhao, Direct conversion of glucose and cellulose to 5-hydroxymethylfurfural in ionic liquid under microwave irradiation, Tetrahedron Lett. 50 (2009) 5403–5405. https://doi.org/10.1016/j.tetlet.2009.07.053.

[48] S. Hu, Z. Zhang, Y. Zhou, J. Song, H. Fan, B. Han, Direct conversion of inulin to 5-hydroxymethylfurfural in biorenewable ionic liquids, (2009) 873–877. https://doi.org/10.1039/b822328a.

[49] S. Zhao, M. Cheng, J. Li, J. Tian, X. Wang, ChemComm One pot production of 5-hydroxymethylfurfural with high yield from cellulose by a Brønsted – Lewis – surfactant-combined heteropolyacid catalyst w, (2011) 2176–2178.

https://doi.org/10.1039/c0cc04444j.

[50] Kamm, B., Gruber, P. R., & Kamm, M. (2007). *Biorefineries – Industrial processes and products*. In *Ullmann's Encyclopedia of Industrial Chemistry*. Wiley-VCH. https://doi.org/10.1002/14356007.l04_l01

[51] B. Girisuta, L.P.B.M. Janssen, H.J. Heeres, A kinetic study on the decomposition of 5-hydroxymethylfurfural into levulinic acid, *Green Chem.* 2006, *8* (8), 701–709. 701–709. https://doi.org/10.1039/b518176c.

[52] B. Siyo, M. Schneider, J. Radnik, M. Pohl, P. Langer, N. Steinfeldt, Applied Catalysis A : General Influence of support on the aerobic oxidation of HMF into FDCA over preformed Pd nanoparticle based materials, "Applied Catal. A, Gen. 478 (2014) 107–116. https://doi.org/10.1016/j.apcata.2014.03.020.

[53] Paquin, F., Rivnay, J., Salleo, A., Stingelin, N., & Silva-Acuña, C. (2015). Multi-phase microstructures drive exciton dissociation in neat semicrystalline polymeric semiconductors. *Journal of Materials Chemistry C, 3*(41), 10715–10722. https://doi.org/10.1039/c5tc02043c.

[54] Román-Leshkov, Y., Barrett, C. J., Liu, Z. Y., & Dumesic, J. A. (2007). Production of dimethylfuran for liquid fuels from biomass-derived carbohydrates. *Nature, 447*(7147), 982–985. https://doi.org/10.1038/nature05923.

[55] H. Cai, C. Li, A. Wang, T. Zhang, Biomass into chemicals : One-pot production of furan-based diols from carbohydrates via tandem reactions, Catal. Today. 234 (2014) 59–65. https://doi.org/10.1016/j.cattod.2014.02.029.

[56] Alamillo, R.; Tucker, M.; Chia, M.; Pagán-Torres, Y. J.; Dumesic, J. A. The Selective Hydrogenation of Biomass-Derived 5-Hydroxymethylfurfural Using Heterogeneous Catalysts. *Green Chem.* **2012**, *14* (5), 1413–1419. https://doi.org/10.1039/c2gc35039d.

[57] Wang, G.; Song, L. Alcohol to Alkyl Levulinates Catalyzed by Double. *Green Chem.* **2014**, *16*, 1436–1443. https://doi.org/10.1039/c3gc41693c.

[58] Braun, M.; Antonietti, M. Metal-Based Heterogeneous Catalysis. *Green Chem.* **2017**, *19*, 3813–3819. https://doi.org/10.1039/c7gc01055a.

[59] Chang, C.; Green, S. K.; Williams, C. L.; Dauenhauer, P. J.; Fan, W. Renewable p-Xylene

with H-BEA. *Green Chem.* **2014**, *16*, 585–588. https://doi.org/10.1039/c3gc40740c.

[60] Daniel, R.; Tian, G.; Xu, H.; Wyszynski, M. L.; Wu, X. Effect of Spark Timing and Load on a DISI Engine Fuelled with 2,5-Dimethylfuran. *Fuel* **2011**, *90* (2), 449–458. https://doi.org/10.1016/j.fuel.2010.10.008.

[61] Rothamer, D. A.; Jennings, J. H.; Cad, A. Study of the Knocking Propensity of 2,5-Dimethylfuran–Gasoline and Ethanol–Gasoline Blends. *Fuel* **2012**, *98*, 203–212. https://doi.org/10.1016/j.fuel.2012.03.049.

[62] Q. Zhang, G. Chen, Z. Zheng, H. Liu, J. Xu, M. Yao, Combustion and emissions of 2 , 5-dimethylfuran addition on a diesel engine with low temperature combustion, Fuel. 103 (2013) 730–735. https://doi.org/10.1016/j.fuel.2012.08.045.

[63] Mitra, J.; Zhou, X.; Rauchfuss, T. B. Pd/C-Catalyzed Reactions of HMF. *Green Chem.* **2015**, *17*, 307–313. https://doi.org/10.1039/c4gc01520g.

[64] J.M. Timko, D.J. Cram, Furanyl unit in host compounds, J. Am. Chem. Soc. 96 (1974) 7159–7160.

[65] Wang, T.; Zhang, J.; Xie, W.; Tang, Y.; Guo, D.; Ni, Y. Catalytic Transfer Hydrogenation of Biobased HMF to 2,5-Bis-(Hydroxymethyl)furan over Ru/Co_3O_4. *Catalysts* **2017**, *7* (3), 92. https://doi.org/10.3390/catal7030092.

[66] Y. Román-Leshkov, C.J. Barrett, Z.Y. Liu, J.A. Dumesic, Production of dimethylfuran for liquid fuels from biomass-derived carbohydrates, Nature. 447 (2007) 982–985. https://doi.org/10.1038/nature05923.

[67] C. Zeng, H. Seino, J. Ren, K. Hatanaka, N. Yoshie, Self-healing bio-based furan polymers cross-linked with various, Polymer (Guildf). 54 (2013) 5351–5357. https://doi.org/10.1016/j.polymer.2013.07.059.

[68] T. Thananatthanachon, T.B. Rauchfuss, Efficient production of the liquid fuel 2, 5-dimethylfuran from fructose using formic acid as a reagent, Angew. Chemie. 37 (2010) 6766–6768. https://doi.org/10.1002/anie.201002267

[69] B. Hu, L. Warczinski, X. Li, M. Lu, J. Bitzer, M. Heidelmann, T. Eckhard, Q. Fu, J. Schulwitz, M. Merko, M. Li, W. Kleist, H. Christof, M. Muhler, B. Peng, Catalysis Formic Acid-Assisted Selective Hydrogenolysis of 5-Hydroxymethylfurfural to 2 , 5-

Dimethylfuran over Bifunctional Pd Nanoparticles Supported on N-Doped Mesoporous Carbon Research Articles, (2021) 6807–6815. https://doi.org/10.1002/anie.202012816.

[70] P. Wu, D. Zhao, G. Lu, C. Cai, Supported Pd – Au bimetallic nanoparticles as an e ffi cient catalyst for the hydrodeoxygenation of vanillin with formic acid at room temperature †, (2022) 1096–1102. https://doi.org/10.1039/d1gc04240h.

[71] L. Tao, T. Yan, L. Tao, T. Yan, W. Li, Y. Zhao, Q. Zhang, Y. Liu, M.M. Wright, Toward an Integrated Conversion of 5-Hydroxymethylfurfural and Ethylene for the Production of Renewable p -Xylene Toward an Integrated Conversion of 5-Hydroxymethylfurfural and Ethylene for the Production of Renewable p -Xylene, *Chem* **2016**, *1* (3), 221–227. https://doi.org/10.1016/j.chempr.2018.07.007.

[72] J. Zhao, M. Liu, G. Fan, L. Yang, F. Li, E ffi cient Transfer Hydrogenolysis of 5 - Hydromethylfurfural to 2 , 5- Dimethylfuran over CoFe Bimetallic Catalysts Using Formic Acid as a Sustainable Hydrogen Donor, (2021). https://doi.org/10.1021/acs.iecr.1c01029.

[73] P. Yang, Q. Xia, X. Liu, Y. Wang, Catalytic transfer hydrogenation / hydrogenolysis of 5-hydroxymethylfurfural to 2 , 5-dimethylfuran over Ni-Co / C catalyst, Fuel. 187 (2017) 159–166. https://doi.org/10.1016/j.fuel.2016.09.026.

[74] W. Fu, Zhaolin; Wang, Z.; Lin, Weigang; Song, Conversion of furan derivatives for preparation of biofuels over Ni-Cu / C catalyst Conversion of furan derivatives for preparation of biofuels over Ni – Cu / C catalyst, (2017). https://doi.org/10.1080/15567036.2017.1310959.

[75] T. Thananatthanachon, T.B. Rauchfuss, Efficient Route to Hydroxymethylfurans from Sugars via Transfer Hydrogenation, *Angew. Chem. Int. Ed.* **2010**, *49* (7), 1139–1141. https://doi.org/10.1002/cssc.201000209.

[76] Endot, N. A., Junid, R., & Jamil, M. S. S. (2021). Insight into biomass upgrade: A review on hydrogenation of 5-hydroxymethylfurfural (HMF) to 2,5-dimethylfuran (DMF). Molecules, 26(22), 6848. https://doi.org/10.3390/molecules26226848

[77] S. Goswami, S. Dey, S. Jana, Design and synthesis of a unique ditopic macrocyclic fluorescent receptor containing furan ring as a spacer for the recognition of dicarboxylic acids, 64 (2008) 6358–6363. https://doi.org/10.1016/j.tet.2008.04.086.

[78] L. Xu, R. Nie, X. Chen, Y. Li, Y. Jiang, X. Lu, Formic acid enabled selectivity boosting in transfer hydrogenation of 5-hydroxymethylfurfural to 2,5-furandimethanol on highly dispersed Co–Nx sites, Catal. Sci. Technol. 11 (2021) 1451–1457. https://doi.org/10.1039/d0cy01969k.

[79] J. Tuteja, H. Choudhary, S. Nishimura, K. Ebitani, Direct Synthesis of 1 , 6-Hexanediol from HMF over a Heterogeneous Pd / ZrP Catalyst using Formic Acid as Hydrogen Source, 1292 (2014) 96–100. https://doi.org/10.1002/cssc.201300832.

[80] Y. Sun, C. Xiong, Q. Liu, J. Zhang, X. Tang, X. Zeng, S. Liu, L. Lin, Catalytic Transfer Hydrogenolysis/Hydrogenation of Biomass-Derived 5-Formyloxymethylfurfural to 2, 5-Dimethylfuran over Ni-Cu Bimetallic Catalyst with Formic Acid As a Hydrogen Donor, Ind. Eng. Chem. Res. 58 (2019) 5414–5422. https://doi.org/10.1021/acs.iecr.8b05960.

[81] P. Yang, Q. Xia, X. Liu, Y. Wang, Catalytic transfer hydrogenation/hydrogenolysis of 5-hydroxymethylfurfural to 2,5-dimethylfuran over Ni-Co/C catalyst, Fuel. 187 (2017) 159–166. https://doi.org/10.1016/j.fuel.2016.09.026.

[82] J. Tuteja, H. Choudhary, S. Nishimura, K. Ebitani, Direct synthesis of 1,6-hexanediol from HMF over a heterogeneous Pd/ZrP catalyst using formic acid as hydrogen source, ChemSusChem. 7 (2014) 96–100. https://doi.org/10.1002/cssc.201300832.

[83] Y. Jiang, W. Chen, Y. Sun, Z. Li, X. Tang, X. Zeng, L. Lin, One-pot conversion of biomass-derived carbohydrates into 5- [(formyloxy) methyl] furfural : A novel alternative platform chemical, Ind. Crop. Prod. 83 (2016) 408–413. https://doi.org/10.1016/j.indcrop.2016.01.004.

[84] C. Xiong, Y. Sun, J. Du, W. Chen, Z. Si, H. Gao, X. Tang, X. Zeng, Efficient conversion of fructose to 5- [(formyloxy) methyl] furfural by reactive extraction and in-situ esterification, 35 (2018) 1312–1318. https://doi.org/10.1007/s11814-018-0025-9.

[85] Y. Sun, C. Xiong, Q. Liu, J. Zhang, X. Tang, X. Zeng, S. Liu, L. Lin, Catalytic Transfer Hydrogenolysis / Hydrogenation of Biomass- Derived 5 - Formyloxymethylfurfural to 2 , 5 - Dimethylfuran Over Ni − Cu Bimetallic Catalyst with Formic Acid As a Hydrogen Donor, (2019). https://doi.org/10.1021/acs.iecr.8b05960.

[86] Y. Jiang, W. Chen, Y. Sun, Z. Li, X. Tang, X. Zeng, L. Lin, S. Liu, One-pot conversion of biomass-derived carbohydrates into 5-[(formyloxy)methyl]furfural: A novel alternative

platform chemical, Ind. Crops Prod. 83 (2016) 408–413.
https://doi.org/10.1016/j.indcrop.2016.01.004.

CHAPTER II:

EXPERIMENTAL TECHNIQUES

This chapter first presents the methods of synthesis of Pd-based catalysts supported on graphitic carbon nitride studied during this work. The experimental techniques for characterization of catalysts, catalytic tests and operating conditions of hydrodeoxygenation of HMF will then be presented.

II.1. Support and catalysts synthesis

II.1.1. Graphitic carbon nitrides properties and method of preparation

Graphitic carbon nitride (g-C_3N_4), an easy-gained sustainable and environmentally friendly material, has attracted growing interest as graphene-like structure that reveals good electrical, thermal, and mechanical properties [1–6]. Abundant amine groups on the surface of g-C_3N_4 provide compatibility for anchoring metal nanoparticles [7]. The presence of nitrogen groups on the surface of carbon support can reduce the size and enhance the stability of nanoparticles [8–12]. These characteristics allow g-C_3N_4 an ideal support for anchoring PdNPs as palladium-based catalyst.

For g-C_3N_4 preparation, a Mixtures of melamine (Sigma-Aldrich®) and urea (Sigma-Aldrich®) in different weight ratio are used as precursors for carbon nitride supports synthesis. In a typical preparation, the required amount of both precursors is dispersed in 20 mL of ethanol (Supelco®) for 30 min at room temperature (25 °C). Then the suspension is transferred to a rotary evaporator for solvent elimination at 150 mBar and 45 °C. This treatment ensures high homogeneity of the initial precursors mixtures before their submission to thermal decomposition at two different temperatures, 550 and 600 °C for 2 h with heating ramp of 2 °C/min. The obtained samples receive the labels **MxUy-T**, where x and y refer to melamine and urea ratios, respectively and T is the decomposition temperature.

The samples prepared from melamine or urea as precursor received the labels **M-T** and **U-T.**

II.1.1. Pd/C_3N_4 catalysts synthesis

Palladium based catalysts were prepared by impregnation.

Impregnation is a widely used method in catalysis for depositing active catalytic components onto a support material. This technique plays a crucial role in the preparation of heterogeneous catalysts.

This method involves the introduction of a precursor solution containing the active catalytic component into the pores of a support material. The precursor is then converted into the active catalytic species through various treatments such as drying, calcination, and reduction. The significance of impregnation lies in its ability to control the dispersion and

loading of the active component on the support, which directly affects the catalyst's performance.

- ✓ Preparation of Precursor Solution: The active catalytic component is dissolved in a suitable solvent to form a solution.
- ✓ Impregnation: The support material is immersed in the precursor solution.
- ✓ Washing: The impregnated supports washed with ultrapure water to remove excess precursor.
- ✓ Drying, calcination and reduction: The impregnated support is dried and calcined to convert the precursor into the active catalytic species.

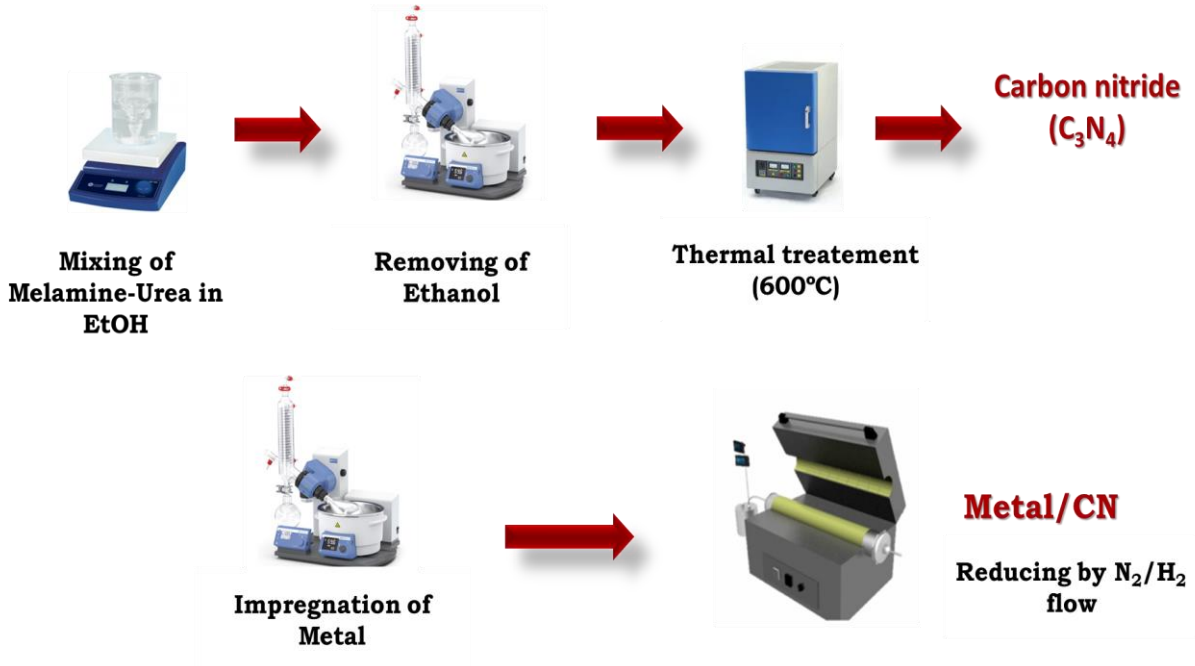

Figure II.1: Preparation of the supports and the catalysts

For Pd-based catalysts preparation by impregnation, the necessary amount of palladium nitrate (Johnson-Matthey®, 7.83% assay) corresponding to 5wt% metal loading is dissolved in 20 mL of distilled water and mixed afterwards with the support. After solvent evaporation the final solid is dried at 100 °C overnight and reduced under 100 mL/min H_2/N_2 (v/v=1/1) flow at 300 °C for 2 h with 2 °C/min heating ramp**.** The prepared catalysts are listed in tableII.1

Table II.1: List of prepared catalysts

Catalyst	Used precursor	T of decomposition (°C)	M:U ratio
5Pd-M–550	**Melamine**	**550**	**/**
5Pd-M–600	**Melamine**	**600**	**/**
5Pd-M_1U_3–550	**Melamine-Urea**	**550**	**1:3**
5Pd-M_1U_3–600	**Melamine-Urea**	**600**	**1:3**
5Pd-M_3U_1–550	**Melamine-Urea**	**550**	**3:1**
5Pd-M_3U_1–600	**Melamine-Urea**	**600**	**3:1**

* For the synthesis of Pd–Co and Pd–Ni bimetallic catalysts, the M1U3-600 sample (hereafter denoted CN) was selected as the support. Palladium was subsequently co-impregnated with either cobalt or nickel onto this support. with a total metal loading of 5 wt%. The resulting bimetallic catalysts are labeled as $5Pd_xCo_\gamma$–CN and $5Pd_xNi_\gamma$–CN, where x and y represent the respective mass fractions of palladium and the second metal in the total metal content. After impregnation, the catalysts were reduced under a N_2/H_2 gas flow in a tubular furnace, ensuring the formation of metallic species and stabilization of the bimetallic nanoparticles (Figure II.1). This approach allows systematic variation of the metal composition while maintaining a constant overall loading, enabling the study of the effect of bimetallic combinations on catalytic performance, the prepared bimetallic catalysts are listed in table II.2.

Table II.2: List of the prepared bimetallic catalysts.

	Pd:M1 Weight Ratio	Pd:M2 Weight Ratio	Total metal content (wt%)
1	1:1	-	5.00
2	2:1	-	5.00
3	3:1	-	5.00
4	1:3	-	5.00
5	-	1:1	5.00
6	-	2:1	5.00
7	-	3:1	5.00
8	-	1:3	5.00
9	-	-	5.00
10	-	-	5.00

II.2. Characterization Techniques

II.2.1. Powder X-Ray Diffraction (XRD)

X-Ray Diffraction (XRD) is a widely used technique for determining the crystalline structure, phase composition, and particle size of solid materials. In heterogeneous catalysts, XRD provides essential information about the structure of the support, the crystallinity of carbon nitride, and the size and dispersion of metal nanoparticles. This information is critical for correlating the structural properties of the catalysts with their catalytic performance [13,14].

In this thesis, XRD measurements were carried out using a PANalytical X´Pert Pro diffractometer with Cu Kα radiation (λ = 1.5404 Å), operated at 45 kV and a cathode current of 40 mA. The data were recorded in the 2θ range of 5–90°, with a step size of 0.05° and a step time of 300 s.

The recorded diffraction patterns were used to determine the d-spacings of the C_3N_4 (002) and (100) planes. In addition, the average metal particle size (Dp) was estimated using the Debye–Scherrer equation:

$$\mathbf{Dp} = \frac{\mathbf{K.\lambda}}{\boldsymbol{\beta}.\cos\boldsymbol{\theta}} \qquad \textbf{(Eq. II.1)}$$

where, Dp is the particle size, K=0.9 is the shape factor that depends on the plane arrangement and particle shape, λ=1.5404 Å is the X-ray wavelength, θ is the diffraction angle, and β is the full width at half maximum (FWHM) of the corresponding diffraction peak.

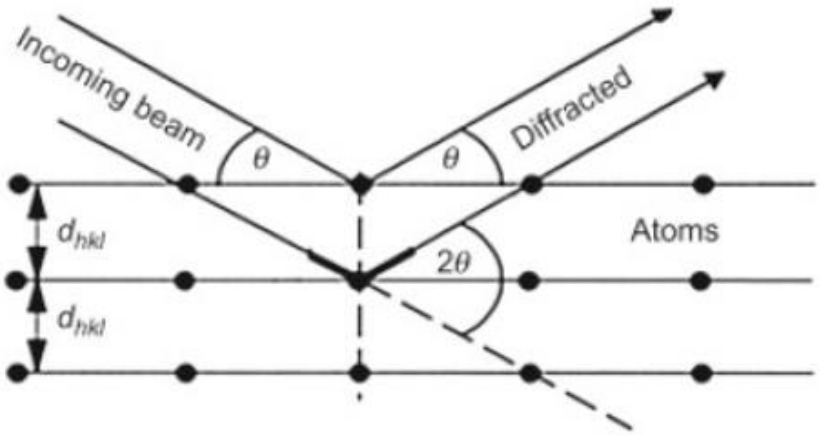

Figure II.2 :Diffraction phenomena [15]

XRD analysis in this work provided critical insights into the crystallinity of the carbon nitride supports and the dispersion and size of palladium particles, which are key factors influencing the catalytic activity in formic acid dehydrogenation and 5-HMF hydrodeoxygenation reactions.

II.1.2 CHN Elemental Analysis

CHN elemental analysis was used to determine the carbon, hydrogen, and nitrogen contents of the prepared carbon nitride materials. This technique provides important information about the chemical composition and the degree of condensation of the carbon nitride structure. A high nitrogen content is characteristic of polymeric carbon nitride and confirms the formation of a nitrogen-rich framework. The carbon to nitrogen (C/N) ratio can be used to evaluate structural changes caused by synthesis conditions or post-treatments. Variations in hydrogen content may indicate the presence of surface functional groups or incomplete condensation. Overall, CHN analysis helps to confirm the successful synthesis of carbon nitride and supports the interpretation of its structural and catalytic properties.

In this work, carbon, hydrogen, and nitrogen elemental analyses were performed using a LECO TruSpec CHN elemental analyzer to determine the chemical composition of the prepared materials.

II.1.3 Inductively coupled plasma–optical emission spectroscopy (ICP-OES)

It is an analytical technique widely used to determine the elemental composition of materials, particularly the metal content. The method is based on the excitation of atoms and ions in a high-temperature plasma, followed by the measurement of their characteristic optical emission. ICP-OES allows accurate and reliable quantification of metals, even at low concentrations [16,17].

The metal content of the prepared catalysts was determined by inductively coupled plasma–optical emission spectroscopy (ICP-OES) using an iCAP 7200 ICP-OES Duo spectrometer (Thermo Fisher Scientific). Prior to analysis, the samples were subjected to microwave-assisted acid digestion. The digestion was carried out on an ETHOS EASY platform (Milestone) using a 1:1 (v/v) mixture of hydrochloric acid (HCl) and nitric acid (HNO_3) at 230 °C for 15 minutes.

II.1.4 Textural Properties by N_2 Adsorption

The textural properties of catalysts, such as specific surface area, pore volume, and pore size distribution, play a crucial role in determining their catalytic performance. These properties influence how reactant molecules can access active sites, how products diffuse out, and how metals are dispersed on the support. Materials with high specific surface area and well-defined pore structures generally provide better accessibility and higher catalytic efficiency. Nitrogen adsorption–desorption is a widely used technique to measure these properties. In this method, nitrogen gas is adsorbed onto the surface of the sample at low temperatures, and the amount of gas adsorbed at different relative pressures is recorded. The specific surface area is typically calculated using the Brunauer–Emmett–Teller (BET) method, while the pore volume and pore size distribution can be determined using the Barrett–Joyner–Halenda (BJH) model.

The shape of the adsorption isotherm is governed by the porous texture of the material under investigation. As illustrated in Figure II.4, the IUPAC classification distinguishes six types of physisorption isotherms, among which Types I, II, IV, and VI are most commonly encountered in the characterization of catalytic materials. Type I isotherms are characteristic of microporous solids with relatively small external surfaces, while Type II isotherms are typically associated with macroporous or non-porous materials exhibiting unrestricted monolayer–multilayer adsorption. Type VI isotherms reflect stepwise multilayer adsorption on highly uniform, nearly non-porous surfaces. Type IV isotherms, on the other hand, are attributed to mesoporous materials and are distinguished by a characteristic hysteresis loop arising from capillary condensation within the mesopores. Given that the catalysts prepared in this study predominantly exhibit mesoporosity, Type IV isotherms are of particular relevance and will therefore be discussed in the following chapter.

In this thesis, the textural properties of the samples were measured using a Micromeritics TRISTAR II instrument. Prior to the analysis, all samples were degassed at 150 °C for 2 hours to remove moisture and other adsorbed gases. These measurements allowed us to compare the structural features of the different supports and understand their influence on metal dispersion and catalytic performance in formic acid dehydrogenation and 5-HMF hydrodeoxygenation reactions.

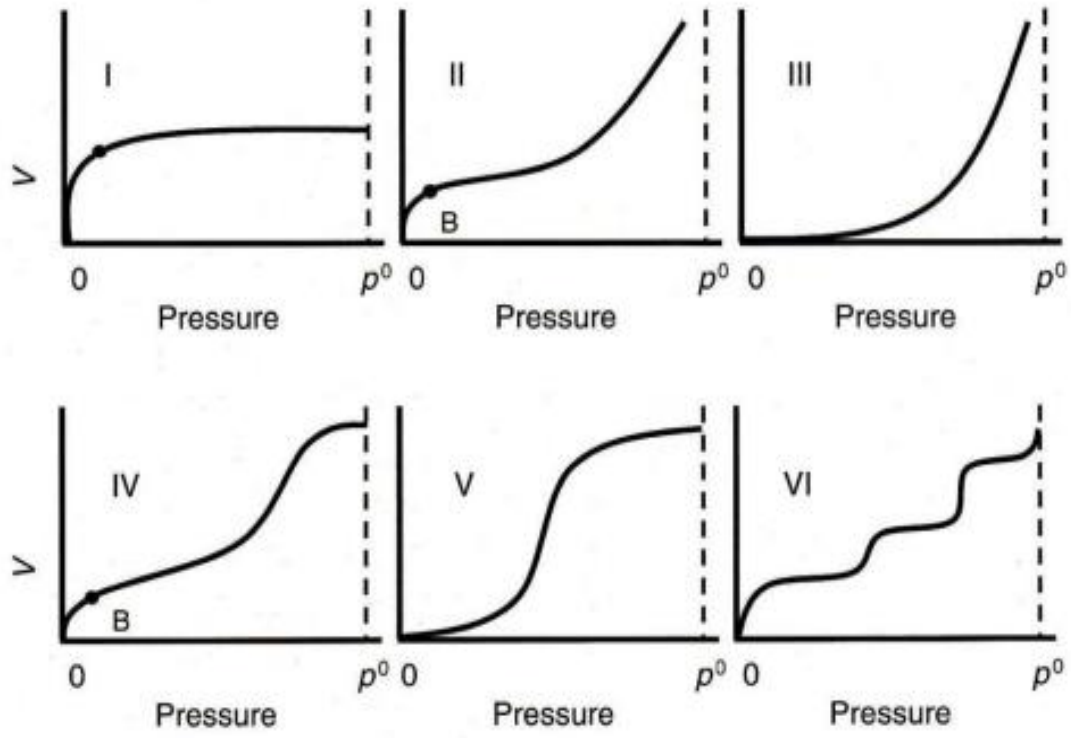

Figure II.3: Adsorption Isotherm types according to IUPAC classifications.

II.1.5 UV–Visible Diffuse Reflectance Spectroscopy (UV–Vis DRS)

UV–Visible diffuse reflectance spectroscopy (UV–Vis DRS) is a powerful technique for studying the optical and electronic properties of solid materials. It provides information about the presence and oxidation state of metal species, their coordination environment, and the interaction between metals and supports. In heterogeneous catalysts, UV–Vis DRS can be used to monitor the formation of metallic nanoparticles, metal clusters, or oxide species, and to detect changes in electronic structure that may affect catalytic activity [18,19]. In this thesis, UV–Vis DRS measurements were performed using a commercial AVASPEC optical spectrometer (Avantes) equipped with an optical fiber solid sensor. Spectra were recorded in the wavelength range of 100–1000 nm using a DH-2000 light source and a CCD detector. Barium sulfate ($BaSO_4$) was used as a reference material to correct for background reflection.

The data obtained from UV–Vis DRS allowed us to identify the nature of the palladium species supported on carbon nitride, distinguish between metallic and oxidized forms, and assess possible interactions between the metal and the support. This information is essential for

understanding the differences in catalytic performance observed during formic acid dehydrogenation and 5-HMF hydrodeoxygenation, as electronic properties and metal-support interactions directly influence reaction rates and selectivity.

II.1.6 X-Ray Photoelectron Spectroscopy (XPS)

X-Ray Photoelectron Spectroscopy (XPS) is a widely used technique for analyzing the surface composition and chemical states of elements in a material. It is particularly useful for heterogeneous catalysts because it provides information on the oxidation state of metals, the chemical environment of surface atoms, and the interactions between the metal and the support. XPS works on the principle of the photoelectric effect: when a material is irradiated with X-rays, electrons are ejected from the surface. By measuring the kinetic energy of these electrons, the binding energy of atoms can be determined, which gives information about their chemical state and surface concentration [20–22].

The photoemission mechanism in X-ray Photoelectron Spectroscopy (XPS) can be described using a three-step model:

- ✓ Step 1: Electron excitation (Intrinsic process): A core-level electron absorbs incident X-ray energy and is excited from its initial energy level to a higher virtual orbital state.
- ✓ Step 2: Electron transport (Extrinsic process): The excited photoelectron migrates through the material toward the sample surface, undergoing possible interactions and energy losses.
- ✓ Step 3: Electron escapes into vacuum.

The photoelectron escapes from the sample surface into the vacuum and is collected by the spectrometer for kinetic energy analysis.

XPS analysis in this work allowed the identification of palladium oxidation states and surface composition, providing insights into metal–support interactions and their influence on the catalytic activity in formic acid dehydrogenation and 5-HMF hydrodeoxygenation reactions.

X-Ray Photoelectron Spectroscopy (XPS) is a widely used technique for analyzing the surface composition and chemical states of elements in a material. It is particularly useful for heterogeneous catalysts because it provides information on the oxidation state of metals, the chemical environment of surface atoms, and the interactions between the metal and the support.

XPS works on the principle of the photoelectric effect: when a material is irradiated with X-rays, electrons are ejected from the surface. By measuring the kinetic energy of these electrons, the binding energy of atoms can be determined, which gives information about their chemical state and surface concentration [20–22].

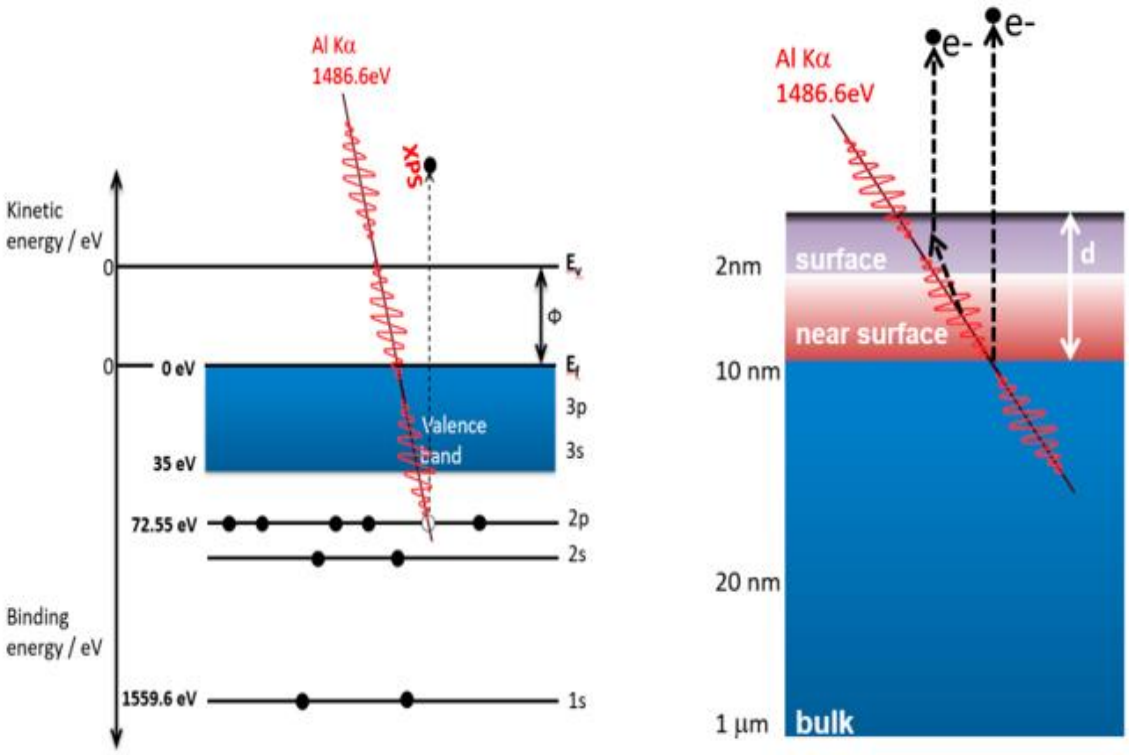

Figure II.4: Schematic Representation of the XPS Photoemission Process

II.1.7 Pyrolysis

Reduction of the metal-based catalysts were carried out using a laboratory-scale tubular furnace for controlled thermal treatment. The experiments were performed in a horizontal IBERFLUID furnace (Model FK 1000), equipped with a continuous horizontal tubular steel reactor with an internal diameter of 7.8 cm. The samples were placed in ceramic vessels of 50 mL volume, positioned in the temperature-controlled zone at the center of the reactor.

During reduction, nitrogen gas was used as an inert atmosphere to prevent oxidation of the support and the metal precursors. For the reduction step, hydrogen gas was introduced to convert the metal species to their metallic state. The flow of each gas was controlled

independently using Bronkhorst mass flow controllers located at the reactor inlet, allowing precise regulation of gas composition.

To avoid clogging in the exhaust line and to collect condensed products, two cold steel traps were installed along the gas outlet. The use of nitrogen ensures controlled thermal decomposition of the precursors, while hydrogen stabilizes the metal nanoparticles in their active metallic form.

A schematic diagram of the pyrolysis and reduction setup is shown in Figure II.7. This procedure allows precise control of temperature, gas composition, and flow, which is essential for obtaining catalysts with well-dispersed metals, preserved support structure, and optimized catalytic performance.

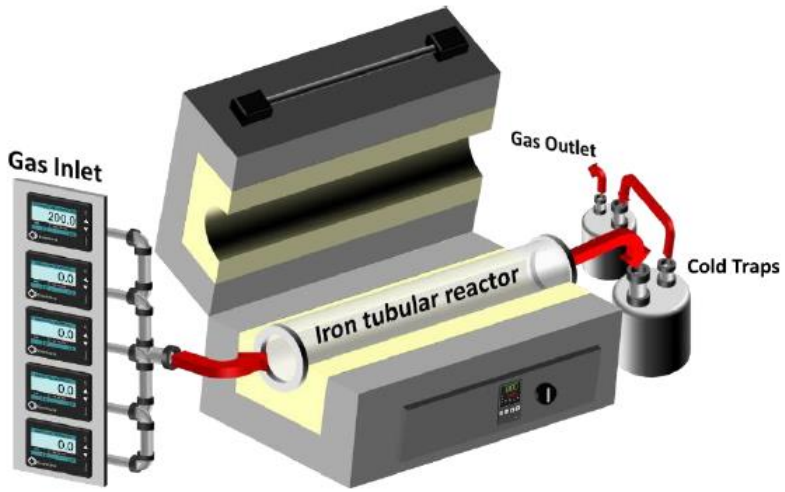

Figure II.5: Representative scheme of the reduction furnace.

II.3. Catalytic activity measurements and analysis

The catalytic reactions were carried out in a stainless-steel Parr 4848 autoclave reactor; a high-pressure batch reactor commonly used for laboratory-scale chemical reactions. The reactor has a robust stainless-steel construction that allows safe operation under elevated pressures and temperatures. It is equipped with a PID (Proportional–Integral–Derivative) temperature controller for precise temperature regulation, and a mechanical stirrer to ensure uniform mixing of reactants and catalysts throughout the reaction volume. The reactor was coupled with a Vaisala M170 CO_2 detector, which enables real-time monitoring of carbon

dioxide evolution during the reaction. This is particularly important for reactions such as formic acid dehydrogenation, where CO_2 production is a key indicator of reaction progress and catalyst performance. The detector operates on the principle of infrared absorption, providing continuous and accurate measurement of CO_2 concentration in the gas phase. This setup allows precise control of reaction conditions, including temperature, pressure, and mixing, while simultaneously monitoring gas evolution, ensuring reproducible and reliable catalytic testing.



Figure II.6: Stainless-steel Parr 4848 autoclave reactor

The Parr reactor offers several advantages for hydrogen-generating reactions. Its high-pressure capability allows the safe handling of gases produced during reactions, such as hydrogen from formic acid decomposition, while the robust stirring and temperature control ensure homogeneous reaction conditions. The ability to couple the reactor with online gas detectors, like the Vaisala M170, enables precise monitoring of gas evolution, facilitating kinetic studies and evaluation of reaction selectivity. In this study, the reactor setup allowed accurate measurement of hydrogen and carbon dioxide production during formic acid

dehydrogenation, as well as the controlled hydrodeoxygenation of 5-hydroxymethylfurfural (5-HMF) to 2,5-dimethylfuran (2,5-DMF), ensuring reliable and reproducible catalytic testing.

II.3.2. Analytical method for products separation and analysis

To analyze the reaction products and determine conversion and selectivity, Gas Chromatography coupled with Mass Spectroscopy (GC–MS) and High-Performance Liquid Chromatography (HPLC) were used in combination. These complementary techniques allow separation, identification, and quantification of reactants and products in catalytic reactions.

Gas Chromatography–Mass Spectroscopy (GC–MS) separates volatile compounds in a gas chromatograph based on boiling points and interactions with the column's stationary phase. The separated compounds are then identified and quantified using a mass spectrometer, which provides molecular weight and fragmentation patterns. GC–MS is highly sensitive and ideal for low-molecular-weight, thermally stable, and volatile products, such as 2,5-dimethylfuran (2,5-DMF) formed from 5-HMF hydrodeoxygenation.

High-Performance Liquid Chromatography (HPLC) separates compounds dissolved in a liquid mobile phase based on interactions with a stationary phase under high pressure. HPLC is particularly suitable for polar, non-volatile, or thermally sensitive compounds, such as 5-hydroxymethylfurfural (5-HMF), formic acid, and other intermediates. It allows accurate quantification without the need for derivatization.

Using GC–MS and HPLC together enables comprehensive analysis: GC–MS detects volatile products, while HPLC monitors polar or thermally labile intermediates. This approach allows precise determination of reactant conversion, product distribution, and reaction selectivity, providing a complete understanding of catalytic performance.

For the estimation of reactant conversion and product selectivity, the generated gas pressure during the reactions was continuously recorded and used to calculate the total gas volume and CO_2 concentration, based on the measurements from the Vaisala M170 CO_2 detector at known gas pressure and reactor volume. In some experiments, the gaseous products generated during dehydrogenation were collected in a gas sampling bag and analyzed using an Agilent 7890A Gas Chromatograph (GC), equipped with a Molsieve 5A column, a Hayesep Q column, and a flame ionization detector (FID). This allowed accurate quantification of the gaseous components, including hydrogen and carbon dioxide.

The resulting liquid phase was filtered on polyvinylidene fluoride (PVDF) syringe membrane filter (0.22 µm pore size) for separation of the catalyst and analyzed by High Pressure Liquid Chromatography (HPLC) Infinity 1260 instrument, equipped with Hi-plex H 300×7.7mm column, refractive index (RI) and diode array (DAD) detectors and GC-MS Agilent 8860 GC system, equipped with HP-5 30.0m ×320 µm ×0.25 µm capillary column and MSD 5977 detector.

HPLC measurements allows the direct deduction of formic acid, bicarbonates HCO_3^-, carbonates CO_3^{2-} and HMF concentration while the use of the latter as internal standard consent the estimation of the HDO products (5-HMF 5-hydroxymethylfurfural, 2,5-dimethylfuran (2,5-DMF), 5-methyl furfural (5- MF) and 5-methyl furfuryl alcohol (5-MFA)) concentrations. The carbon balance has been calculated and the difference between the final and initial C moles give an idea on the loss of HMF during the reaction in condensed products, labelled as humins in this study.

For the calculations of conversion, selectivity, yields, carbon balances in FAD and HDO reactions and the normalization of the catalytic activity over exposed active sites (turnover number (TON) and turnover frequency (TOF)) the following equations have been used:

$$Formic\ acid\ Conversion\ (\%) = \frac{moles\ of\ initial\ FA - moles\ of\ final\ FA}{moles\ of\ initial\ FA}.100 \quad (Eq.II.1)$$

$$FAD\ Carbon\ Balance\ (\%) = \frac{C\ moles\ Final}{C\ moles\ initial}.100 \quad (Eq.II.2)$$

TON and TOF are used to compare similar results from the literature and are calculated using the following formulas:

$$TON = \frac{moles\ of\ limitant\ reactif\ converted}{moles\ of\ palladium * Dispersion} \quad (Eq.\ II.3)$$

$$TOF\ (h^{-1}) = \frac{TON}{time\ (h)} \quad (Eq.\ II.4)$$

$$5\text{-}HMF\ Conversion\ (\%) = \frac{moles\ of\ initial\ (5-HMF) - moles\ of\ final\ (5-HMF)}{moles\ of\ initial\ (5-HMF)}.100 \quad (Eq.II.5)$$

$$Yield\ (\%) = \frac{moles\ of\ product}{moles\ of\ intial\ (5-HMF)} . 100 \qquad (Eq.\ II.6)$$

$$Selectivity\ (\%) = \frac{moles\ of\ HDO\ product}{moles\ of\ analyzed\ products\ by\ GC-MS} . 100 \qquad (Eq.\ II.7)$$

$$Humins\ (\%) = 100 - \frac{Final\ carbon\ moles}{Initial\ carbon\ moles} . 100 \qquad (Eq.\ II.8)$$

$$HDO\ Carbon\ balance\ (\%) = \frac{final\ moles\ of\ analyzed\ products\ by\ GC-MS}{initial\ 5-HMF\ moles} . 100 \qquad (Eq.\ II.9)$$

For the estimation of conversion and selectivity, the generated gas pressure was recorded and used for total gas volume and CO_2 concentration calculation on the base of Vaisala detector measurements over a known gas pressure and volume. The resulting liquid phase was filtered for separation of the catalyst and analyzed by High Pressure Liquid Chromatography (HPLC) Infinity 1260 instrument, equipped with Hi-plex H 300 x7.7 mm column, refractive index (RI) and diode array (DAD) detectors and GC-MS Agilent 8860 GC system, equipped with HP-5 30.0 m × 320 μm ×0.25 μm capillary column and MSD 5977 detector.

HPLC Calibration

To establish the relationship between peak area and concentration, a calibration procedure was performed using high-performance liquid chromatography (HPLC). Stock solutions of formic acid (FA) and 5-hydroxymethylfurfural (5-HMF) were individually prepared at a concentration of 1 M using ultrapure water as the solvent. In addition, sodium bicarbonate ($NaHCO_3$) was used to prepare a 1 M stock solution representing the bicarbonate (HCO_3^-) system. Each stock solution was accurately prepared in a volumetric flask to ensure precise molarity and homogeneity.

From each 1 M stock solution, a series of standard working solutions were prepared by appropriate volumetric dilution with ultrapure water in 100 mL volumetric flasks to obtain the

desired calibration range. All solutions were freshly prepared prior to analysis to minimize degradation and ensure reproducibility.

For chromatographic analysis, a 1 mL aliquot of each standard solution was transferred into an HPLC vial and injected under identical instrumental conditions. The resulting chromatographic peak areas were recorded for each analyte. These data were then used to construct calibration curves by plotting peak area versus known concentration, enabling quantification of FA, 5-HMF, and HCO_3^- in unknown samples under the same analytical conditions.

GC–MS Calibration

Quantitative analysis of the reaction products was performed using gas chromatography–mass spectrometry (GC–MS). Tetrahydrofuran (THF) was used as the solvent for all calibration standards, while n-octane was employed as the internal standard due to its chemical stability, suitable volatility, and effective chromatographic separation from the target analytes.

Calibration curves were established for 5-hydroxymethylfurfural (5-HMF), 2,5-dimethylfuran (2,5-DMF), 5-methylfurfural (5-MF), and 5-methylfurfuryl alcohol (5-MFA). For this purpose, the masses of THF and n-octane were kept constant in all calibration mixtures, while the mass of each target compound was systematically varied to obtain the desired concentration range. All solutions were prepared gravimetrically using an analytical balance to ensure high accuracy and reproducibility.

Each calibration mixture was analyzed under identical GC–MS conditions. The analytical response was expressed as the ratio of the peak area of each analyte to that of n-octane, and plotted as a function of the corresponding analyte concentration to construct calibration curves. This internal standard approach compensates for variations in injection volume, sample handling, and instrumental response, ensuring reliable quantification.

References

[1] K.S. Novoselov, A.K. Geim, S. V Morozov, D. Jiang, Y. Zhang, S. V Dubonos, I. V Grigorieva, A.A. Firsov, Electric field effect in atomically thin carbon films, Science (80-.). 306 (2004) 666–669. https://doi.org/10.1126/science.1102896

[2] H. Liu, J. Wang, Z. Feng, Y. Lin, L. Zhang, D. Su, Facile Synthesis of Au Nanoparticles Embedded in an Ultrathin Hollow Graphene Nanoshell with Robust Catalytic Performance., Small. 11 (2015) 5059–5064. https://doi.org/10.1002/smll.201501231

[3] C. Zhou, C. Lai, D. Huang, G. Zeng, C. Zhang, M. Cheng, L. Hu, J. Wan, W. Xiong, M. Wen, Highly porous carbon nitride by supramolecular preassembly of monomers for photocatalytic removal of sulfamethazine under visible light driven, Appl. Catal. B Environ. 220 (2018) 202–210. https://doi.org/10.1016/j.apcatb.2017.08.050

[4] W.-W. Tang, G.-M. Zeng, J.-L. Gong, J. Liang, P. Xu, C. Zhang, B.-B. Huang, Impact of humic/fulvic acid on the removal of heavy metals from aqueous solutions using nanomaterials: a review, Sci. Total Environ. 468 (2014) 1014–1027. https://doi.org/10.1016/j.scitotenv.2013.09.044

[5] J.-H. Deng, X.-R. Zhang, G.-M. Zeng, J.-L. Gong, Q.-Y. Niu, J. Liang, Simultaneous removal of Cd (II) and ionic dyes from aqueous solution using magnetic graphene oxide nanocomposite as an adsorbent, Chem. Eng. J. 226 (2013) 189–200. https://doi.org/10.1016/j.cej.2013.04.070

[6] M.Q. Wen, T. Xiong, Z.G. Zang, W. Wei, X.S. Tang, F. Dong, Synthesis of MoS_2/g-C_3N_4 nanocomposites with enhanced visible-light photocatalytic activity for the removal of nitric oxide (NO), Opt. Express. 24 (2016) 10205–10212. https://doi.org/10.1364/oe.24.010205

[7] B. Vellaichamy, P. Periakaruppan, Catalytic hydrogenation performance of an in situ assembled Au@ gC_3N_4–PANI nanoblend: synergistic inter-constituent interactions boost the catalysis, New J. Chem. 41 (2017) 7123–7132. https://doi.org/10.1039/C7NJ01085K

[8] X.-H. Li, X. Wang, M. Antonietti, Mesoporous gC_3 N_4 nanorods as multifunctional supports of ultrafine metal nanoparticles: hydrogen generation from water and reduction of nitrophenol with tandem catalysis in one step, Chem. Sci. 3 (2012) 2170–

2174. https://doi.org/10.1039/C2SC20289A

[9] M. Boronat, A. Corma, F. Illas, J. Radilla, T. Ródenas, M.J. Sabater, Mechanism of selective alcohol oxidation to aldehydes on gold catalysts: Influence of surface roughness on reactivity, J. Catal. 278 (2011) 50–58. https://doi.org/10.1016/j.jcat.2010.11.013

[10] J.-L. Gong, B. Wang, G.-M. Zeng, C.-P. Yang, C.-G. Niu, Q.-Y. Niu, W.-J. Zhou, Y. Liang, Removal of cationic dyes from aqueous solution using magnetic multi-wall carbon nanotube nanocomposite as adsorbent, J. Hazard. Mater. 164 (2009) 1517–1522. https://doi.org/10.1016/j.jhazmat.2008.09.072

[11] C. Zhang, C. Lai, G. Zeng, D. Huang, C. Yang, Y. Wang, Y. Zhou, M. Cheng, Efficacy of carbonaceous nanocomposites for sorbing ionizable antibiotic sulfamethazine from aqueous solution, Water Res. 95 (2016) 103–112. https://doi.org/10.1016/j.watres.2016.03.014

[12] Y. Zhang, G.M. Zeng, L. Tang, J. Chen, Y. Zhu, X.X. He, Y. He, Electrochemical sensor based on electrodeposited graphene-Au modified electrode and nanoAu carrier amplified signal strategy for attomolar mercury detection, Anal. Chem. 87 (2015) 989–996. https://doi.org/10.1021/ac503472p

[13] A.A. Bunaciu, E.G. UdriŞTioiu, H.Y. Aboul-Enein, X-ray diffraction: instrumentation and applications, Crit. Rev. Anal. Chem. 45 (2015) 289–299. https://doi.org/10.1080/10408347.2014.949616

[14] E.S. Ameh, A review of basic crystallography and x-ray diffraction applications, Int. J. Adv. Manuf. Technol. 105 (2019) 3289–3302. https://doi.org/10.1007/s00170-019-04508-1

[15] M. Ghasempour-Mouziraji, J. Lagarinhos, D. Afonso, R.A. de Sousa, A review study on metal powder materials and processing parameters in Laser Metal Deposition, Opt. Laser Technol. 170 (2024) 110226. https://doi.org/10.1016/j.optlastec.2023.110226

[16] C. Douvris, T. Vaughan, D. Bussan, G. Bartzas, R. Thomas, How ICP-OES changed the face of trace element analysis: Review of the global application landscape, Sci. Total Environ. 905 (2023) 167242. https://doi.org/10.1016/j.scitotenv.2023.167242

[17] I. Rezić, I. Steffan, ICP-OES determination of metals present in textile materials, Microchem. J. 85 (2007) 46–51. https://doi.org/10.1016/j.microc.2006.06.010

[18] J. Torrent, V. Barrón, Diffuse reflectance spectroscopy, Methods Soil Anal. Part 5—Mineralogical Methods. 5 (2008) 367–385. https://doi.org/10.2136/sssabookser5.5.c13

[19] H. Zhang, X. Wang, J. Wang, Q. Chen, H. Huang, L. Huang, S. Cao, X. Ma, UV–visible diffuse reflectance spectroscopy used in analysis of lignocellulosic biomass material, Wood Sci. Technol. 54 (2020) 837–846. https://doi.org/10.1007/s00226-020-01199-w

[20] P.S. Bagus, E.S. Ilton, C.J. Nelin, The interpretation of XPS spectra: Insights into materials properties, Surf. Sci. Rep. 68 (2013) 273–304. https://doi.org/10.1016/j.surfrep.2013.03.001

[21] D.N.G. Krishna, J. Philip, Review on surface-characterization applications of X-ray photoelectron spectroscopy (XPS): Recent developments and challenges, Appl. Surf. Sci. Adv. 12 (2022) 100332. https://doi.org/10.1016/j.apsadv.2022.100332

[22] J.F. Watts, J. Wolstenholme, An introduction to surface analysis by XPS and AES, John Wiley & Sons, 2019. https://doi.org/10.1002/9781119417651.ch7

CHAPTER III:

RESULTS OF CATALYSTS CHARACTERIZATION

We present the results of characterization obtained for the different catalysts and for monometallic Pd and bimetallic PdCo, PdNi separately. (ICP-OSS, XRD, UV-vis, N2 adsorption and XPS, however, some catalysts, those that have shown the best performance in catalysis, will be studied much more thoroughly.

III.1. Characterization of monometallic Pd-based catalysts

III.1.1 Chemical analysis by ICP-OES spectrometry

The actual metal content on Pd catalysts measured by ICP-OES spectrometry is compared to the total theoretical value of 5 % in Table III.1.

All samples get over the targeted value due more probably to loss of support during the reduction treatment of the catalysts. The use of nitrate as palladium precursor might induce the formation of gaseous species like CO, NO, CO_2 and NO_2 which diminish the quantity of carbon nitride and increases the final Pd content. The real Pd contents change randomly and do not show any specific relation with the type and mix of precursors used for supports preparation. On the contrary, the supports prepared at 600ºC stabilize the carbon nitride against additional transformation during the reduction treatments, exception made by 5Pd- M_1U_3-600 sample.

Table III.1: ICP-OES analysis of the Pd-MxUy-T catalysts

	Pd Content (%)
5Pd-M-550	6.8
5Pd-M-600	6.6
5Pd-M_1U_3-550	7.8
5Pd-M_1U_3-600	8.2
5Pd-M_3U_1-550	11
5Pd-M_3U_1-600	6.2

III.1.2 Elemental analysis

The CNH analysis and calculated C/N and C/H ratios and production yield for all synthesized C_3N_4 samples are summarized in Table III.2. All samples show close C/N values, lower to the theoretical one (0.75) suggesting the formation of nitrogen rich C_3N_4 structures with a presence

of some amino (-NH/NH_2) groups as additional inevitable defects caused by errors during the thermal condensation and some preferential gasification of C atoms [1,2]. This defects are frequently associated to carbon vacancies, a defect suggested by our lower C/N value [3]. In addition, the interaction between amino groups could produce two kinds of cyano defects (=N-C≡N and -HN-C≡N) produced from terminal (-NH/NH_2) groups and strings like N atoms stacking trough H bond. This effect is potentiated by extra N agents during the condensation like urea addition to melamine in our case [4].

Table III.2: CNH analysis and solid yield.

Sample	Yield	%C	%N	%H	Formulas*	C/N	C/H
M-550	44	37.27	60.66	1.71	$C_3N_{4.8}H_{0.14}$	0.61	21.7
M-600	60	37.42	60.35	2.12	$C_3N_{4.8}H_{0.17}$	0.62	17.7
M_1U_3-550	12	37.34	60.10	1.99	$C_3N_{4.8}H_{0.16}$	0.62	18.8
M_1U_3-600	10	38.28	60.18	1.21	$C_3N_{4.7}H_{0.09}$	0.63	31.6
M_3U_1-550	42	37.22	60.54	1.78	$C_3N_{4.9}H_{0.14}$	0.61	20.9
M_3U_1-600	38	37.45	60.66	1.54	$C_3N_{4.8}H_{0.12}$	0.61	24.3
5Pd-M-550	-	32	55.36	1.87	$C_3N_{5.17}H_{0.17}$	0.58	17.24
5Pd-M-600	-	33.16	56.50	2.11	$C_3N_{5.08}H_{0.19}$	0.59	15.73
5Pd-M_1U_3-550	-	31.98	54.09	1.59	$C_3N_{5.08}H_{0.15}$	0.59	20.15
5Pd-M_1U_3-600	-	33.11	56.19	1.91	$C_3N_{5.08}H_{0.17}$	0.59	17.31
5Pd-M_3U_1-550	-	31.37	52.90	2.00	$C_3N_{5.08}H_{0.19}$	0.59	15.64
5Pd-M_3U_1-600	-	33.81	56.27	1.79	$C_3N_5H_{0.16}$	0.60	18.90

* calculated assuming C content as 3.

Nevertheless, the obtained final solid weight yield and C/H ratio are very different. Both, the thermal treatment (calcination) temperature and change in precursors (melamine/urea) ratio have a significant effect on the observed values. The use of raw melamine results in higher solid' yield (60% for M-600). However, the increase of urea precursor lowers the final yield of C_3N_4. The increase of the calcination temperature decreases the yield of the obtained solid, exception made by M-600. The M_1U_3-600 shows around 90% of mass loss after calcination. This is ascribed to the difference between melamine (345°C) and urea (132.7 °C) melting

temperatures. In fact, the increase in temperature promotes the gas formation resulting in higher C elimination and N enrichment in the final solid.

The C/H ratio changes more randomly with the precursors and calcination temperature. The M_1U_3-600 gives a high value of 31.60 while the M-600 support showed around the half (17.7). The addition of more urea in the initial mixture could induce as stated above a cyano group defect formation resulting in that high value of C/H ratio. This process induces higher electron density over the nitrogen atom and could affect significantly the palladium deposition and activity in formic acid dehydrogenation reaction. In summary the obtained elemental analysis indicate materials close to "C_3N_4" formula of "melon" type graphitic g-C_3N_4 with carbon vacancies and possible amino or cyano functionalities [5]. The obtained colour of the synthesized carbon nitride varied from pale yellow for the samples prepared at 550°C to yellow for those at 600°C. This colour changes are attributed to the presence of terminal hydrogen species and the formation of shorter polymeric chains.

*After metal introduction **carbon and nitrogen content decreased in comparison to the parent support to 31-34% of C and 52-57% of N** due to the oxidation by metal nitrate precursor. C/N slightly diminishes indicating slight N enrichment of the surface.

III.1.3. Textural properties by N_2 adsorption

The textural properties of both, supports and monometallic Pd-based catalysts were determined by N_2 adsorption-desorption measurements. All MxUy-T and 5Pd-MxUy-T samples showed a IV-H3 type isotherms, according to IUPAC classification [6]. The hysteresis loop, represented in Figure III.1, indicates mesoporous materials with slit-shaped pores in discoid particle aggregates [7].

The calculated textural parameters vary with the precursor ratio and calcination temperature (Table IV.4). The synthesized samples from raw melamine, M-550 and M-600, exhibit poor specific surface area (BET) values. On the contrary, the presence of urea increases both, surface area and porous volume. While the improvement in textural properties for M_3U_1 appears less significant, **the use of melamine/urea ratio of 1/3, increases surface and pore volume almost three times with respect to raw melamine** (S_{BET} and V_t= 98.3 m^2/g, 0.215 cm^3/g for M_1U_3-600 *vs.* 22.5 m^2/g and 0.069 cm^3/g for M-600).

The pore average diameter appears randomly affected in respect to initial precursor ratio but shows a decreasing tendency with the temperature of C_3N_4 condensation due more probably to loss of intraparticular volume at higher temperature and particles sintering. In general, the presence of oxygen in urea, leads to the formation of CO_2 during its thermal decomposition, promoting the development of porosity [8] through mesoporous surface area enlargement and new micro/mesopores creation. In addition, the use of urea increases the possibility for heteroatoms incorporation (N or O containing functional groups), suggesting the presence of sites with different electron density.

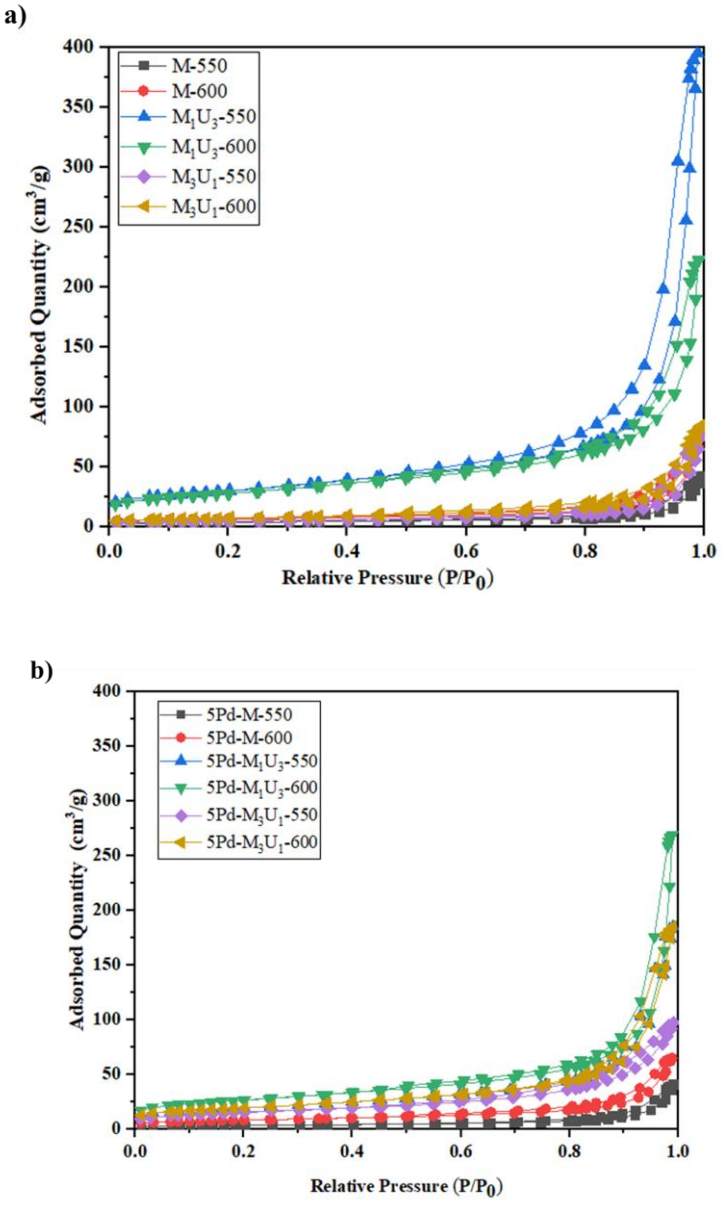

Figure III.1: N_2-physisorption of the prepared a) supports and b) Pd-based catalysts.

Table III.3: Textural properties of the prepared supports and catalysts

Sample	S_{BET} (m^2/g)	S_{Mic} (m^2/g)	S_{Ext} (m^2/g)	S_{Ext}/S_{BET}	S_{mic}/S_{Ext}	V_t (cm^3/g)	Pore diameter (nm)
M-550	**13**	**3**	**10**	**0.76**	**0.31**	**0.041**	**12.7**
M-600	**23**	**6**	**17**	**0.76**	**0.30**	**0.069**	**12.4**
M_1U_3-550	**106**	**21**	**85**	**0.80**	**0.25**	**0.396**	**14.9**
M_1U_3-600	**98**	**19**	**79**	**0.80**	**0.25**	**0.215**	**8.8**
M_3U_1-550	**17**	**4**	**13**	**0.76**	**0.32**	**0.070**	**16.5**
M_3U_1-600	**25**	**6**	**19**	**0.77**	**0.29**	**0.077**	**12.4**
5Pd-M-550	**12**	**2**	**10**	**0.82**	**0.23**	**0.037**	**12.7**
5Pd-M-600	**29**	**5**	**24**	**0.82**	**0.21**	**0.075**	**10.5**
5Pd-M_1U_3-550	**68**	**12**	**56**	**0.83**	**0.20**	**0.218**	**12.8**
5Pd-M_1U_3-600	**94**	**17**	**77**	**0.82**	**0.22**	**0.229**	**9.8**
5Pd-M_3U_1-550	**54**	**7**	**47**	**0.86**	**0.16**	**0.120**	**8.8**
5Pd-M_3U_1-600	**20**	**4**	**16**	**0.82**	**0.21**	**0.054**	**10.9**

After palladium incorporation**, the total pores volume and average pore diameter decrease with the S_{micro}/S_{ext} ratio, suggesting smaller pores filling with metal particles**. However, the textural parameters increased, i.e. 5Pd-M_3U_1-550 sample with BET surface change from 17 to 54 m^2/g after impregnation. This could be explained by the fact that **some Pd particles have diffused between the C_3N_4 layers increasing the mesoporous surfaces**. Similarly to the support series, 5Pd-M_1U_3-600 shows the highest surface area (94 m^2/g) inversely related to the mean pore diameter. The 5Pd-M-550, on the other hand, shows the lowest surface area (12 m^2/g).

III.1.4. XRD results

The X-ray diffractograms of all synthesized catalysts are shown in Figure 2. Carbon nitride and metallic Pd characteristic diffractions are observed for all samples. The diffractions centered at 2θ around 13° and 27° correspond to (100) and (002) planes of hexagonal graphitic C_3N_4 (JCPDS 01-087-1526) [9,10]. The former diffraction corresponds to the *d-spacing* of in-plane organization of the triazine or heptazine based structural units (indicated as *c* in Table 3 while the latter correspond to the stacking perpendicular to that plane (parameter *a* in Table 3). The *a* parameter appears less affected by precursor ratio and temperature while the *c* parameter variation indicates loss of crystallinity for the samples prepared with urea due to the appearance of N-related defects originating difficulties in growing of large size layers and resulting in poor crystalline materials [3].

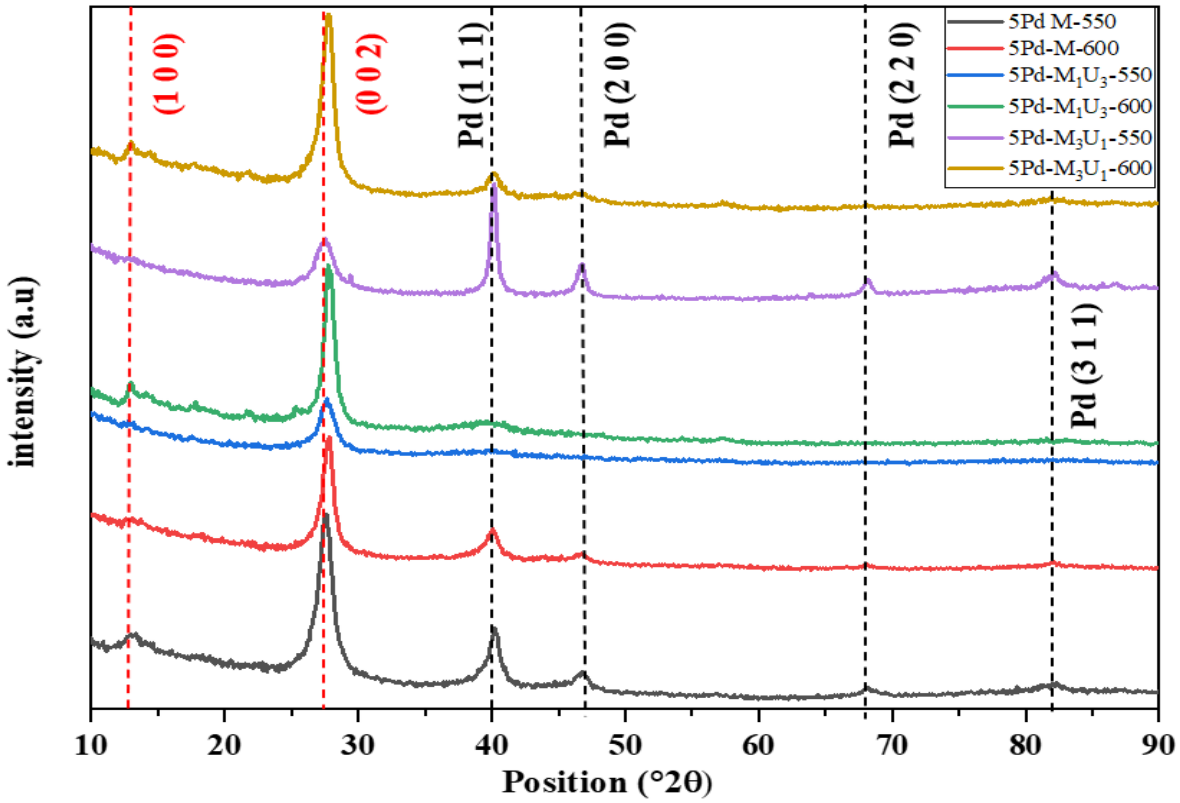

Figure III.2:X-ray diffractograms of 5Pd-M_xU_y-T

As the urea precursor content increased, the (002) planes shift to lower angles suggesting the presence of voids and defects within the unit cell increasing vacant orbital number. Pd

structure indexed as fcc cubic (JCPDS 03-065-6174) shows all principal diffractions at 2θ= 39.97°, 46.61°, 68.03°, and 81.90° assigned to (111), (200), (220), and (311) planes, respectively [9]. Within the series, the metal presence is confirmed over the (111) plane, it is the only visible diffraction for 5Pd M_1U_3-550 and 5Pd M_1U_3-600 samples. The size of Pd nanoparticles calculated using Debye-Scherrer equation over Pd (111) plane is summarized in Table 3. 5Pd-M_1U_3-550 and 5Pd-M_1U_3-600 shows the smallest particle size with an average of 3.6 and 2.8 nm, respectively. However, the 5Pd-M_3U_1-550 has a large particle size with an average of 15.4 nm.

Table III.4: Structural parameters, Pd particle size and Pd content of the prepared catalysts

	c (Å)	a (A°)	Pd (nm)	Pd, wt%*	Dispersion (%)
5Pd-M-550	6.68	3.24	6.7	6.8	24.49
5Pd-M-600	6.62	3.22	9.1	6.6	18.34
5Pd-M_1U_3-550	n.d.	3.23	3.6	7.8	55.86
5Pd-M_1U_3-600	6.82	3.20	2.8	8.2	44.05
5Pd-M_3U_1-550	n.d.	3.24	15.4	11	11.15
5Pd-M_3U_1-600	6.78	3.12	9.1	6.2	18.34
C_3N_4-M	6.86	3.21	-	-	-

n.d. not detected, *measured by ICP, - not determined

Also, in table III.3 the dispersion values are reported, in fact, dispersion is calculated based on metal content determined by ICP-OES and palladium particle size calculated from XRD.

The actual Pd content on the formed catalysts measured by ICP-OES is compared to the theoretical value of 5% in Table 3. All samples get over the targeted value due more probably to loss of support during the reduction treatment of the catalysts. The use of nitrate as palladium precursor might induce the formation of gaseous species like CO, NO, CO_2 and NO_2 which diminish the quantity of carbon nitride and increases the final Pd content. The real Pd contents change randomly and do not show any specific relation with the type and mix of precursors used for supports preparation. On the contrary, **the supports prepared at 600ºC stabilize the carbon nitride against additional transformation during the reduction treatments, exception made by 5Pd-M_1U_3-600 sample.** The highest specific surface area of this sample allows better metal/carbon interaction promoting gas formation and higher support loss.

III.1.5. UV-Vis spectroscopy:

The UV–vis DRS analysis provides information on the optical property of support and their corresponding Pd catalysts. The UV–Vis spectra of all M_xU_y-T and Pd-M_xU_y-T samples are presented in Figure III.3a

The typical absorption edge (figure III.3a) within or near the visible range of the spectrum is observed and attributed to n→π* transition for the C_3N_4 sample and is accompanied with a small shoulder at 467 nm assigned to NH_2 transitions[11].

The adsorption edge blue shifts with the addition of urea and with the increase of the temperature of C_3N_4 synthesis. The differences spectra (Fig. 3b MxUy-T sample minus M-T spectra) shows a disappearance of the band assigned to NH_2 together with edge blue shifting around 420 nm (blue arrow band). This change is due from one side to -NH_2 conversion into cyano defects as suggested above and H content decrease but also to the decrease in crystallinity for the samples resulting in higher band gaps and edge shifting.

It has been reported that porous nanosheet structures containing cyano groups limits visible adsorption of C_3N_4 producing a blue shift of the absorption edge and increasing the band gap [12]. In addition, the difference spectra show also an important change around 350 nm (red arrow band) assigned to the formation of single and double pore type structures with a low number of repeating triazine basic units. This contribution is especially affected by the crystallinity and the presence of N-containing defects[13].

After coupling with Pd (Fig. 3c) a decrease in intensity of the bands is observed and associated to the loss of reflectance in our system and due to the color change of the sample (dark grey to dark brownish). The adsorption edge varies between the samples without clear trend due to the addition of Pd levels in the HOMO-LUMO gap of C3N4 and their position change as a function of Pd particles size. Nevertheless, similar changes to that observed for the supports are observed in the difference spectra (Fig. 3d 5 Pd/MxUy-T minus corresponding MxUy-T sample) for the bands centered in 300–400 nm range. The Pd plasmon (green arrow band) appears as a positive low intensity band at around 500 nm accompanied by a sharp band at 220 nm (brown arrow band) attributed to N-to-Pd electron transfer suggesting the positioning of the Pd particles close to N atoms.

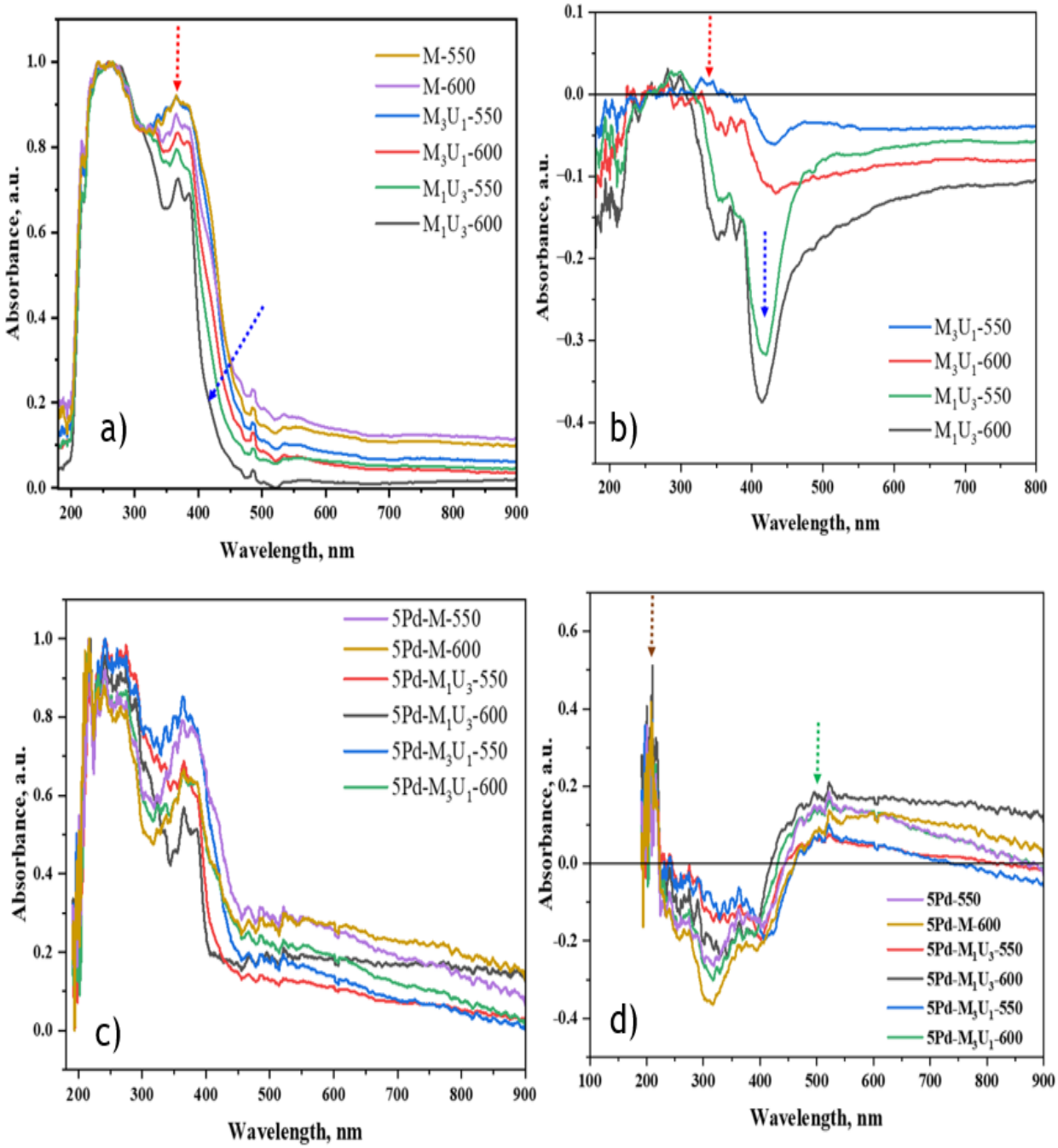

Figure III.3: UV-VIS spectra of a) M_xU_y-T and c) 5Pd M_xU_y-T samples

III.2. Characterization of bimetallic catalysts

III.2.1. Chemical analysis by ICP-OES spectrometry

The CNH analysis and calculated C/N and C/H ratios and production yield for all synthesized C_3N_4 samples are summarized in Table III.2. All samples show close C/N values, lower to the theoretical one (0.75) suggesting the formation of nitrogen rich C_3N_4 structures with a presence

of some amino (-NH/NH_2) groups as additional inevitable defects caused by errors during the thermal condensation and some preferential gasification of C atoms [1,2]. This defects are frequently associated to carbon vacancies, a defect suggested by our lower C/N value [3]. In addition, the interaction between amino groups could produce two kinds of cyano defects (=N-C≡N and -HN-C≡N) produced from terminal (-NH/NH_2) groups and strings like N atoms stacking trough H bond. This effect is potentiated by extra N agents during the condensation like urea addition to melamine in our case [4].

Table III.2: CNH analysis and solid yield.

Sample	Yield	%C	%N	%H	Formulas*	C/N	C/H
M-550	44	37.27	60.66	1.71	$C_3N_{4.8}H_{0.14}$	0.61	21.7
M-600	60	37.42	60.35	2.12	$C_3N_{4.8}H_{0.17}$	0.62	17.7
M_1U_3-550	12	37.34	60.10	1.99	$C_3N_{4.8}H_{0.16}$	0.62	18.8
M_1U_3-600	10	38.28	60.18	1.21	$C_3N_{4.7}H_{0.09}$	0.63	31.6
M_3U_1-550	42	37.22	60.54	1.78	$C_3N_{4.9}H_{0.14}$	0.61	20.9
M_3U_1-600	38	37.45	60.66	1.54	$C_3N_{4.8}H_{0.12}$	0.61	24.3
5Pd-M-550	-	32	55.36	1.87	$C_3N_{5.17}H_{0.17}$	0.58	17.24
5Pd-M-600	-	33.16	56.50	2.11	$C_3N_{5.08}H_{0.19}$	0.59	15.73
5Pd-M_1U_3-550	-	31.98	54.09	1.59	$C_3N_{5.08}H_{0.15}$	0.59	20.15
5Pd-M_1U_3-600	-	33.11	56.19	1.91	$C_3N_{5.08}H_{0.17}$	0.59	17.31
5Pd-M_3U_1-550	-	31.37	52.90	2.00	$C_3N_{5.08}H_{0.19}$	0.59	15.64
5Pd-M_3U_1-600	-	33.81	56.27	1.79	$C_3N_5H_{0.16}$	0.60	18.90

* calculated assuming C content as 3.

Nevertheless, the obtained final solid weight yield and C/H ratio are very different. Both, the thermal treatment (calcination) temperature and change in precursors (melamine/urea) ratio have a significant effect on the observed values. The use of raw melamine results in higher solid' yield (60% for M-600). However, the increase of urea precursor lowers the final yield of C_3N_4. The increase of the calcination temperature decreases the yield of the obtained solid, exception made by M-600. The M_1U_3-600 shows around 90% of mass loss after calcination. This is ascribed to the difference between melamine (345°C) and urea (132.7 °C) melting

temperatures. In fact, the increase in temperature promotes the gas formation resulting in higher C elimination and N enrichment in the final solid.

The C/H ratio changes more randomly with the precursors and calcination temperature. The M_1U_3-600 gives a high value of 31.60 while the M-600 support showed around the half (17.7). The addition of more urea in the initial mixture could induce as stated above a cyano group defect formation resulting in that high value of C/H ratio. This process induces higher electron density over the nitrogen atom and could affect significantly the palladium deposition and activity in formic acid dehydrogenation reaction. In summary the obtained elemental analysis indicate materials close to "C_3N_4" formula of "melon" type graphitic g-C_3N_4 with carbon vacancies and possible amino or cyano functionalities [5]. The obtained colour of the synthesized carbon nitride varied from pale yellow for the samples prepared at 550°C to yellow for those at 600°C. This colour changes are attributed to the presence of terminal hydrogen species and the formation of shorter polymeric chains.

*After metal introduction **carbon and nitrogen content decreased in comparison to the parent support to 31-34% of C and 52-57% of N** due to the oxidation by metal nitrate precursor. C/N slightly diminishes indicating slight N enrichment of the surface.

III.2.2. Elemental analysis

The actual metal content on Pd catalysts measured by ICP-OES spectrometry is compared to the total theoretical value of 5 % in Table III.1.

All samples get over the targeted value due more probably to loss of support during the reduction treatment of the catalysts. The use of nitrate as palladium precursor might induce the formation of gaseous species like CO, NO, CO_2 and NO_2 which diminish the quantity of carbon nitride and increases the final Pd content. The real Pd contents change randomly and do not show any specific relation with the type and mix of precursors used for supports preparation. On the contrary, the supports prepared at 600ºC stabilize the carbon nitride against additional transformation during the reduction treatments, exception made by 5Pd- M_1U_3-600 sample.

Table III.1: ICP-OES analysis of the Pd-MxUy-T catalysts

	Pd Content (%)

5Pd-M-550	6.8
5Pd-M-600	6.6
5Pd-M_1U_3-550	7.8
5Pd-M_1U_3-600	8.2
5Pd-M_3U_1-550	11
5Pd-M_3U_1-600	6.2

III.2.3 XRD-analysis

The textural properties of both, supports and monometallic Pd-based catalysts were determined by N_2 adsorption-desorption measurements. All MxUy-T and 5Pd-MxUy-T samples showed a IV-H3 type isotherms, according to IUPAC classification [6]. The hysteresis loop, represented in Figure III.1, indicates mesoporous materials with slit-shaped pores in discoid particle aggregates [7].

The calculated textural parameters vary with the precursor ratio and calcination temperature (Table IV.4). The synthesized samples from raw melamine, M-550 and M-600, exhibit poor specific surface area (BET) values. On the contrary, the presence of urea increases both, surface area and porous volume. While the improvement in textural properties for M_3U_1 appears less significant, **the use of melamine/urea ratio of 1/3, increases surface and pore volume almost three times with respect to raw melamine** (S_{BET} and V_t= 98.3 m^2/g, 0.215 cm^3/g for M_1U_3-600 *vs.* 22.5 m^2/g and 0.069 cm^3/g for M-600).

The pore average diameter appears randomly affected in respect to initial precursor ratio but shows a decreasing tendency with the temperature of C_3N_4 condensation due more probably to loss of intraparticular volume at higher temperature and particles sintering. In general, the presence of oxygen in urea, leads to the formation of CO_2 during its thermal decomposition, promoting the development of porosity [8] through mesoporous surface area enlargement and new micro/mesopores creation. In addition, the use of urea increases the possibility for heteroatoms incorporation (N or O containing functional groups), suggesting the presence of sites with different electron density.

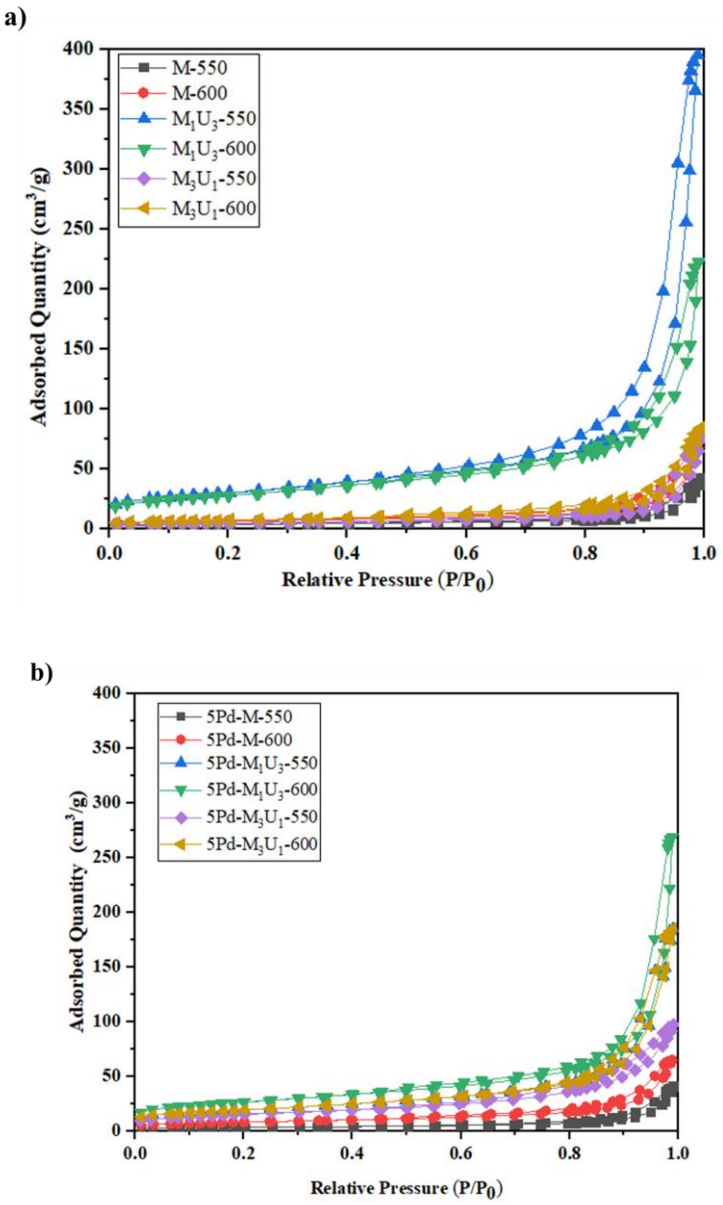

Figure III.1: N_2-physisorption of the prepared a) supports and b) Pd-based catalysts.

Table III.3: Textural properties of the prepared supports and catalysts

Sample	S_{BET} (m^2/g)	S_{Mic} (m^2/g)	S_{Ext} (m^2/g)	S_{Ext}/S_{BET}	S_{mic}/S_{Ext}	V_t (cm^3/g)	Pore diameter (nm)
M-550	**13**	**3**	**10**	**0.76**	**0.31**	**0.041**	**12.7**
M-600	**23**	**6**	**17**	**0.76**	**0.30**	**0.069**	**12.4**

M_1U_3-550	**106**	**21**	**85**	**0.80**	**0.25**	**0.396**	**14.9**
M_1U_3-600	**98**	**19**	**79**	**0.80**	**0.25**	**0.215**	**8.8**
M_3U_1-550	**17**	**4**	**13**	**0.76**	**0.32**	**0.070**	**16.5**
M_3U_1-600	**25**	**6**	**19**	**0.77**	**0.29**	**0.077**	**12.4**
5Pd-M-550	**12**	**2**	**10**	**0.82**	**0.23**	**0.037**	**12.7**
5Pd-M-600	**29**	**5**	**24**	**0.82**	**0.21**	**0.075**	**10.5**
5Pd-M_1U_3-550	**68**	**12**	**56**	**0.83**	**0.20**	**0.218**	**12.8**
5Pd-M_1U_3-600	**94**	**17**	**77**	**0.82**	**0.22**	**0.229**	**9.8**
5Pd-M_3U_1-550	**54**	**7**	**47**	**0.86**	**0.16**	**0.120**	**8.8**
5Pd-M_3U_1-600	**20**	**4**	**16**	**0.82**	**0.21**	**0.054**	**10.9**

After palladium incorporation**, the total pores volume and average pore diameter decrease with the S_{micro}/S_{ext} ratio, suggesting smaller pores filling with metal particles**. However, the textural parameters increased, i.e. 5Pd-M_3U_1-550 sample with BET surface change from 17 to 54 m^2/g after impregnation. This could be explained by the fact that **some Pd particles have diffused between the C_3N_4 layers increasing the mesoporous surfaces**. Similarly to the support series, 5Pd-M_1U_3-600 shows the highest surface area (94 m^2/g) inversely related to the mean pore diameter. The 5Pd-M-550, on the other hand, shows the lowest surface area (12 m^2/g).

III.2.4 XPS-analysis

III.3. Partial Conclusion

The combined physicochemical characterization of monometallic Pd and bimetallic PdCo and PdNi catalysts supported on graphitic carbon nitride evidences a strong interdependence between synthesis parameters, defect chemistry, textural development, and metal–support interactions.

The characterization results demonstrated that both the synthesis conditions of carbon nitride supports and the incorporation of metallic species strongly influence the structural, textural, and electronic properties of the prepared catalysts. The melamine/urea ratio and calcination temperature enabled effective tuning of the support porosity, resulting in BET surface areas ranging from 13–23 $m^2\ g^{-1}$ for melamine-derived samples to 98–106 $m^2\ g^{-1}$ for urea-rich materials. The introduction of urea promoted mesoporosity and significantly increased pore volume, providing favorable conditions for metal dispersion.

Elemental and structural analyses confirmed the formation of carbon-rich, nitrogen-defective g-C_3N_4 materials with C/N ratios close to 0.61–0.63, while XRD results demonstrated the preservation of the graphitic carbon nitride framework after metal incorporation. Metal loading induced a contraction of the interlayer spacing, evidencing strong metal–support interactions. Palladium particle sizes varied between 2.8 and 15.4 nm, with the smallest nanoparticles obtained on urea-rich supports and in bimetallic systems, indicating improved stabilization and dispersion.

Optical and surface analyses revealed that defect engineering through synthesis conditions modified the electronic structure of g-C_3N_4 by generating nitrogen vacancies and cyano defects, leading to changes in band-gap energy and charge-transfer properties. XPS results further demonstrated electronic interactions between Pd and the support, as well as between Pd and the secondary metals (Co or Ni), evidenced by negative shifts of 0.5–1.5 eV in Pd binding energies. These findings confirm the occurrence of electron transfer phenomena and the formation of electronically modified active sites.

Generally, the characterization study established clear structure-property relationships, showing that high surface area, enhanced porosity, small Pd particle size, and strong metal–support interactions are key features of the most promising catalysts. These physicochemical characteristics are expected to play a decisive role in determining the catalytic performance in formic acid dehydrogenation and HMF hydrodeoxygenation reactions discussed in the following chapter.

References

[1] A. Thomas, A. Fischer, F. Goettmann, M. Antonietti, J.-O. Müller, R. Schlögl, J.M. Carlsson, Graphitic carbon nitride materials: variation of structure and morphology and their use as metal-free catalysts, J. Mater. Chem. 18 (2008) 4893–4908. https://doi.org/10.1039/B800274F

[2] J. Zhu, P. Xiao, H. Li, S.A.C. Carabineiro, Graphitic carbon nitride: synthesis, properties, and applications in catalysis, ACS Appl. Mater. Interfaces. 6 (2014) 16449–16465. https://doi.org/10.1021/am502925j

[3] O. Iqbal, H. Ali, N. Li, A.I. Al-sulami, K.F. Alshammari, H.S.M. Abd-rabboh, Y. Al-hadeethi, I. Ud, A.I. Alharthi, R. Altamimi, A. Zada, Z. Wang, A. Hayat, M. Zahid, A review on the synthesis , properties , and characterizations of graphitic carbon nitride (g-C_3N_4) for energy conversion and storage applications, Mater. Today Phys. 34 (2023) 101080. https://doi.org/10.1016/j.mtphys.2023.101080.

[4] H. Tan, X. Gu, P. Kong, Z. Lian, B. Li, Z. Zheng, Applied Catalysis B : Environmental Cyano group modi fi ed carbon nitride with enhanced photoactivity for selective oxidation of benzylamine, 242 (2019) 67–75. https://doi.org/10.1016/j.apcatb.2018.09.084.

[5] B. V Lotsch, M. Dçblinger, J. Sehnert, L. Seyfarth, J. Senker, O. Oeckler, W. Schnick, Diffraction , Solid-State NMR Spectroscopy , and Theoretical Calculations — Structural Characterization of a Carbon Nitride Polymer, (2007) 4969–4980. https://doi.org/10.1002/chem.200601759.

[6] K.S. F. Rouquerol, J. Rouquerol, Assessment of Mesoporosity,Adsorption by Powders and Porous Solids, Elsevier. (1994) 191–217. https://doi.org/10.1016/B978-0-12-598920-6.50008-7.

[7] B. Fan, L. Xing, Q. He, F. Zhou, X. Yang, T. Wu, G. Tong, D. Wang, W. Wu, Selective synthesis and defects steering superior microwave absorption capabilities of hollow graphitic carbon nitride micro-polyhedrons, Chem. Eng. J. 435 (2022) 135086. https://doi.org/10.1016/j.cej.2022.135086.

[8] J.M. Chem, Polycondensation of thiourea into carbon nitride semiconductors as visible, (2012) 8083–8091. https://doi.org/10.1039/c2jm00097k.

[9] C.H. Hak, L.C. Sim, M / g-C_3N_4 (M =Ag , Au , and Pd) composite : synthesis via sunlight photodeposition and application towards the degradation of bisphenol A, 4 (2018) 25401–25412. https://doi.org/10.1007/s11356-018-2632-8

[10] Y. Wu, M. Wen, Y. Kuwahara, Palladium Nanoparticles Supported on Titanium-Doped Graphitic Carbon Nitride for Formic Acid Dehydrogenation, (2017) 860–867. https://doi.org/10.1002/asia.201700041.

[11] Y. Li, C. Mo, J. Li, D. Yu, Pyrazine–nitrogen–rich exfoliated C4N nanosheets as efficient metal–free polymeric catalysts for oxygen reduction reaction, J. Energy Chem.

49 (2020) 243–247. https://doi.org/10.1016/j.jechem.2020.02.046

[12] Y. Wang, P. Du, H. Pan, L. Fu, Y. Zhang, J. Chen, Y. Du, Increasing Solar Absorption of Atomically Thin 2D Carbon Nitride Sheets for Enhanced Visible-Light Photocatalysis, 1807540 (2019) 1–8. https://doi.org/10.1002/adma.201807540.

[13] S. Zhai, P. Guo, J. Zheng, P. Zhao, B. Suo, Y. Wan, Density functional theory study on the stability, electronic structure and absorption spectrum of small size g-C3N4 quantum dots, Comput. Mater. Sci. 148 (2018) 149–156. https://doi.org/10.1016/j.commatsci.2018.02.023

[14] S.Y. Shen, T.S. Zhao, J.B. Xu, Y.S. Li, Synthesis of PdNi catalysts for the oxidation of ethanol in alkaline direct ethanol fuel cells, J. Power Sources. 195 (2010) 1001–1006. https://doi.org/10.1016/j.jpowsour.2009.08.079

[15] R. Li, Z. Wei, T. Huang, A. Yu, Ultrasonic-assisted synthesis of Pd–Ni alloy catalysts supported on multi-walled carbon nanotubes for formic acid electrooxidation, Electrochim. Acta. 56 (2011) 6860–6865. https://doi.org/10.1016/j.electacta.2011.05.097

[16] M.A. Matin, A. Kumar, R.R. Bhosale, M.A.H.S. Saad, F.A. Almomani, M.J. Al-Marri, PdZn nanoparticle electrocatalysts synthesized by solution combustion for methanol oxidation reaction in an alkaline medium, RSC Adv. 7 (2017) 42709–42717. https://doi.org/10.1039/C7RA07013F

[17] W. Wang, S. Ji, H. Wang, R. Wang, Nanoporous PdNi/C Electrocatalyst Prepared by Dealloying High-Ni-content PdNi Alloy for Formic Acid Oxidation, Fuel Cells. 12 (2012) 1129–1133. https://doi.org/10.1002/fuce.201200098.

CHAPTER IV:

CATALYTIC RESULTS

Dimethylfuran is a promising liquid fuel that can be derived from sustainable biomass sources. Obtaining dimethylfuran from biomass through an efficient catalytic hydrodeoxygenation process is an effective way to achieve carbon neutrality. In this research field, the present work aims at developing Pd-based catalysts for formic acid-assisted selective conversion of 5-hydroxymethylfurfural to dimethylfuran. Thus, a systematic comparative study was performed by variation of the method of preparation of support, the effect of Pd doping by cobalt and nickel on the catalytic performance was also studied.

In this chapter, we present separately the catalytic results of two reactions:

1) Formic acid dehydrogenation
2) HMF hydrodeoxygenation

IV.1. Formic acid dehydrogenation

For this reaction, we have chosen to present first the results obtained on Pd catalysts and then those obtained on bimetallic catalysts.

IV.1.1. Pd-based catalysts

The catalytic activity of all prepared Pd nanoparticles supported on carbon nitride in formic acid dehydrogenation in terms of formic acid conversion and generated gas pressure is presented in Figure IV.1.

Only two catalysts reach almost complete formic acid dehydrogenation, **5Pd-M_1U_3-600 and 5Pd-M_1U_3-550 with 98% and 96% conversion respectively**. Here it is the place to mention that those catalysts showed **higher Pd loadings (around 8 wt.%).** Nevertheless, the highest Pd loading it is not necessary an indication for high conversion, 5Pd-M_3U_1-550 sample present one of the lowest conversion for a very high metal content 11 wt.% Pd. On the other hand, these two samples present the lowest particle size suggesting that **the conversion is guided by the availability of the sites on the surface.**

The increase in the calcination temperature of the support also positively affects formic acid dehydrogenation. **The FA conversion increased from 51 to 88% for 5Pd-M-550 and 5Pd-M-600 sample, respectively**. In this particular case it appears more an **effect of support surface increase and C/H ratio decrease** that of Pd loadings and size. The initial hydrogen generation rates (slope of the pressure curve at initial time of reaction) are very different for both samples, indicating not only a different initial rate but also a different rate of deactivation

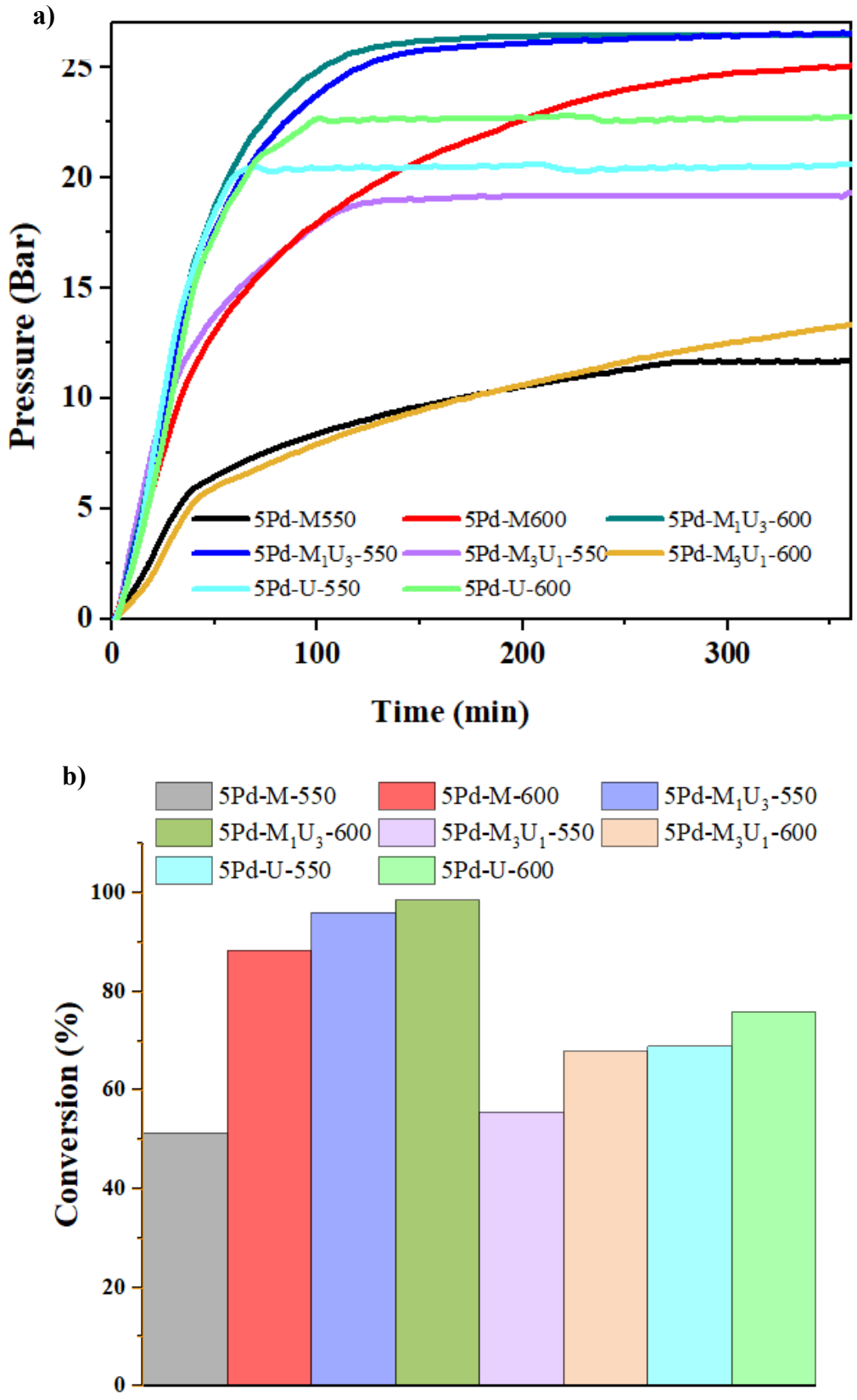

Figure IV.1: a) Generated gas pressure and b) formic acid conversion over different 5Pd-MxUy -T catalysts (T=150°C, time=6h, m_{cata} =100mg, V=20mL and C_{FA} =1M)

(when the curve tend to a constant value). It appears that **the increase of aromaticity (lower C/H ratio) results in higher electron density transfer from N to Pd (also observed by the important band at 220 nm for the 5Pd-M-600 sample) having a positive effect on hydrogen production**.

For the samples prepared from urea precursor, the 5Pd-U-550 catalyst reached equilibrium within 65 minutes, generating a total gas pressure of 20.6 bar and achieving corresponding to 69% of formic acid conversion. **5Pd-U-600 catalyst requires a longer reaction time (95 min) to reach equilibrium but produced a higher total gas pressure and conversion (75%).** It has been reported that carbon nitride synthesized from urea at 500–600°C typically exhibits a BET surface area ranging from 32 to 52 m^2/g and pore sizes between 40 and 58 nm [1,2]. In contrast, the 5Pd-M-550 and 5Pd-M_3U_1-600 samples, present lower BET surface areas of 12 m^2/g and 20 m^2/g, explaining its lower catalytic performance.

Table IV.1: Total gas volume, CO_2 concentration in liquid ((bi)carbonates and in gas phase and carbon balance.

Catalyst	Total Volume (CO_2 +H_2) mL	CO_2 Volume (mL)	C (bi)carbonate (M)	Carbon Balance (%)
5Pd-M-550	246	101	0.002	73
5Pd-M-600	560	238	0.018	67
5Pd-M_1U_3-550	608	268	0.028	67
5Pd-M_1U_3-600	624	270	0.011	65
5Pd-M_3U_1-550	259	91.4	0.019	66
5Pd-M_3U_1-600	438	182	0.012	75
5Pd-U-550	384	155	0.006	68
5Pd-U-600	435.	178	0.010	64

The total gas volume and CO_2 concentration in liquid ((bi)carbonates) and in gas phase are listed in Table 4. Only H_2 and CO_2 are expected in gas phase with an equimolar ratio. The estimated highest total gas in respect to the measured CO_2 **indicates some dissolution of CO_2 as (bi)carbonates in the continuous phase and also the loss of CO_2 by "fizzing" during the opening of the reactor** due to the change in equilibrium conditions at atmospheric pressure. This process is responsible for the carbon balance decrease to 70-75 % for all samples. The presence of basic functional groups on support surface favours the simultaneous protonation and reduction of CO_2 to carbonates. [3,4].

IV.1.1.1. Effect of tetrahydrofuran (THF) solvent

We further evaluated the effect of using of **the tetrahydrofuran (THF) as solvent** on the catalytic activity of a selected 5Pd-M3U1-600 catalyst, the obtained results are compared to those obtained using water as solvent (figure IV.2) and the values are summarized in table IV.2.

Table IV.2. Generated total volume of gas and CO_2 concentration for the reactions performed in water and THF

	Total Volume (ml)	**CO_2 volume (ml)**	**CO_2/CO ratio**
5Pd-M_1U_3-600 H_2O	438.4	175.93	95/5
5Pd-M_1U_3-600 THF	483.2	138.21	90/10

The generated pressure in THF is lower to that generated in water due to the difference in boiling point of the solvents and the higher dissolution of hydrogen. The formic acid conversion is similar (92 %) with some differences observed in the generated total gas and CO_2. Slightly **higher volume of CO was produced in THF** but still the reaction remains very selective to CO_2. From these results, we can confirm that the estimated highest total gas in respect to the measured CO_2 observed previously, was not only responsible for the carbon balance decrease to 70-75 % for all samples but also for the **small amount of formed CO formed through dehydration measured only for 5Pd-M_3U_1-600 sample** in Table IV.2).

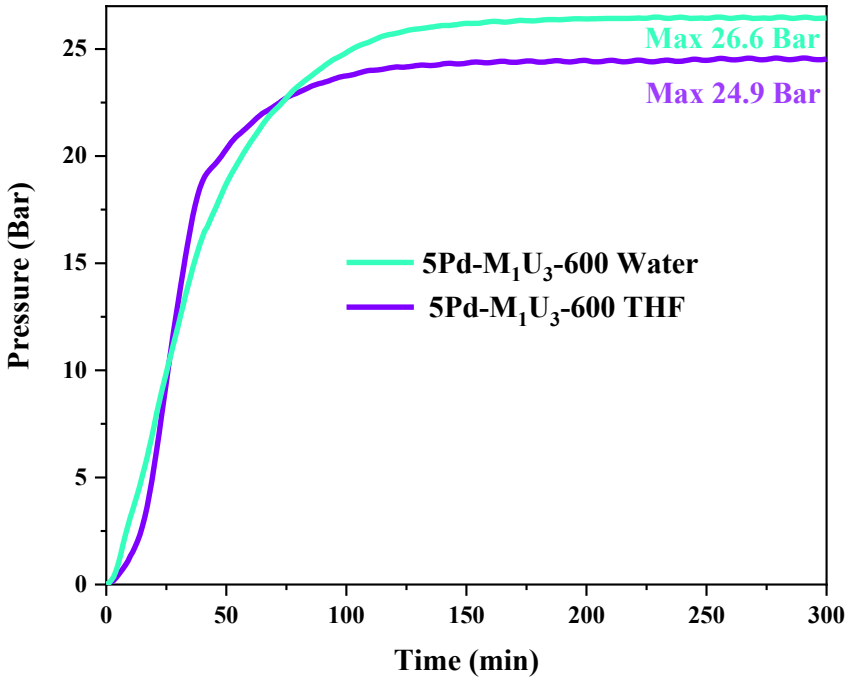

Figure VI.2. Comparison of formic acid dehydrogenation reaction in water and THF solvents

IV.1.1.2. Reactivity-structure correlation

If we represent the FA conversion variation vs. textural properties of the samples a clear tendency is observed, higher the BET surface higher the conversion (Figure 5a). The only exception is made by 5Pd-M_3U_1-550 sample resulting in poor conversion in respect to its surface area. This sample presents the lowest average pore diameter of all samples and the highest Pd particle size (Figure 5b) for the highest Pd loading indicating that the dehydrogenation reaction is much more sensitive to particle size and dispersion than to the metal loading. **The higher surface of the support and higher nitrogen content benefits the dispersion of Pd resulting in very active catalysts**.

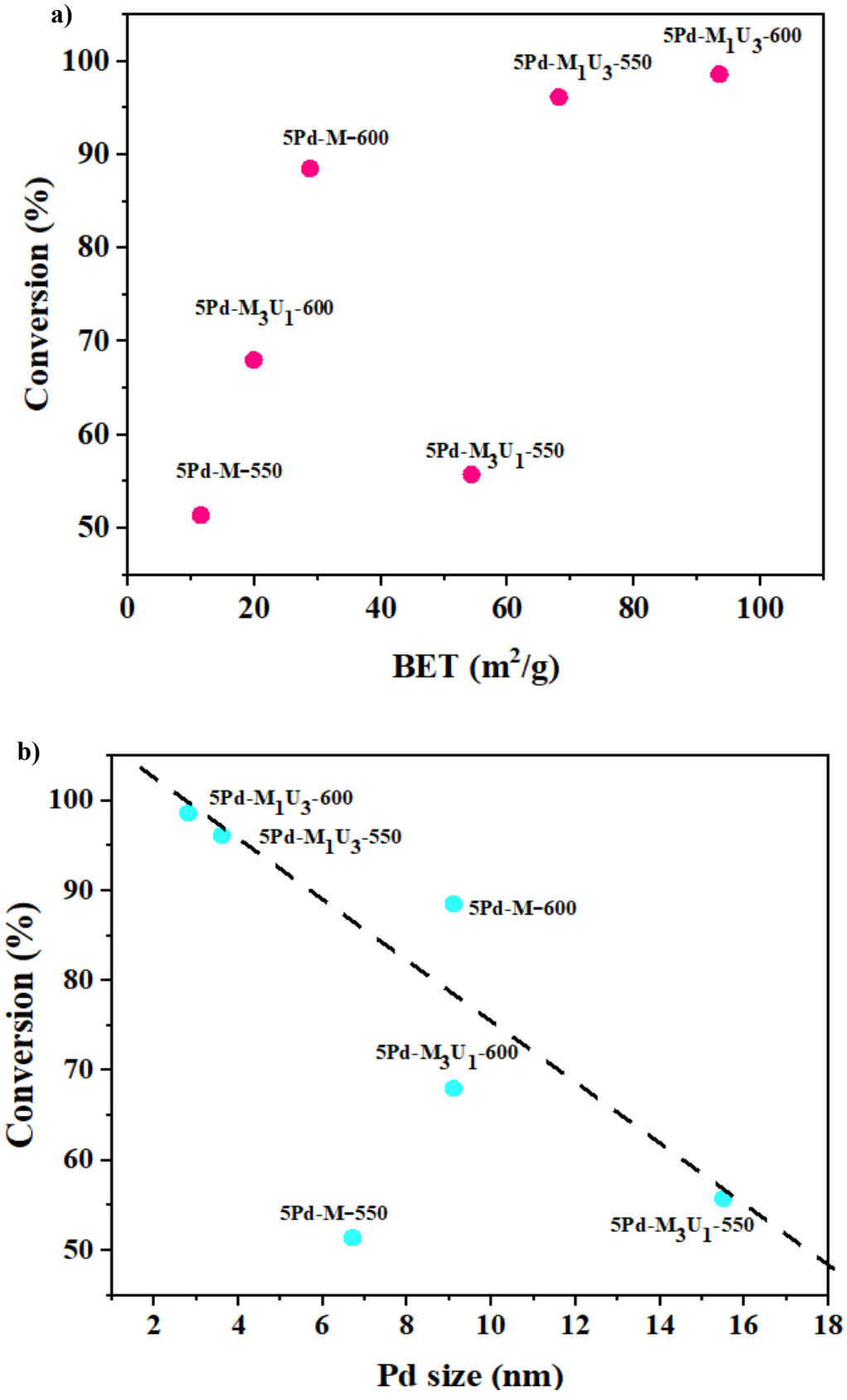

Figure IV.3: a) FA conversion vs. BET surface area and b) FA conversion vs. Pd particle size.

In summary we can conclude that **the support improves palladium dispersion and anchoring and enhances the mass transfer of formic acid to and out of active sites**.

On the other hand, **higher dispersion and higher C/H ratio increase the electrons density of the metal particles by assuring the electron transfer from N-atoms in the π-conjugated systems directly to Pd** [5]. On the contrary, the real metal loading appears less important, 5Pd-M_3U_1-550 catalyst possess the highest palladium content (11.13 wt%) but exhibited low formic acid conversion.

Based on the obtained data and literature [6–9], we can suggest that the adsorption of FA molecules on the catalyst surface needs higher surface. The adsorbed formates are the proposed intermediates of dehydrogenation reaction [10–14] and are formed after O-H bond cleavage, resulting in stable bidentate ($HCOO_B$) or monodentate ($HCOO_M$) formates on the active surface. Then, CO_2 and H_2 are formed after C-H bond cleavage in the final stage. The rapid increase of the gas pressure in the initial stage indicates a high initial velocity of H_2/CO_2 formation, where the desorption of the gases is more rapid than the adsorption of the reactants. Nevertheless, **at higher temperature the adsorption prevails over the desorption causing a catalyst deactivation.** The catalysts that show higher initial rate of reaction are the catalysts that reach higher conversion working in a range where the adsorption and desorption rates are similar. Any change that produces a different velocities of adsorption/desorption results in catalyst deactivation and lower final formic acid conversion. The transfer of electron density in the heterojunction between the semiconductor C_3N_4 and metal enriches Pd electron density and helps the desorption of the products.

Although difficult to compare to other catalyst due to the disparity of used conditions and formulation, in Table 5 we present some similar works published in the literature. Some of the values (TON) are directly indicated in these studies, while others were re-calculated by us using the relationship mentioned above.

Table. IV.3. TON and TOF for different palladium-based catalysts.

Catalyst	Reaction conditions	BET specific surface area (m^2/g)	TON	TOF[1] (h^{-1})	Ref
5Pd-M-550	6.8wt%, T=150°C, 100mg, C_{FA}= 1M	11	651	217	This work
5Pd-M-600	6.6wt%, T=150°C, 100mg, C_{FA}= 1M	29	1573	524	This work
5Pd-M_1U_3-550	7.8wt%, T=150°C, 100mg, C_{FA}= 1M	68	467	156	This work
5Pd-M_1U_3-600	8.2wt%, T=150°C, 100mg, C_{FA}= 1M	93	581	194	This work
5Pd-M_3U_1-550	11wt%, T=150°C, 100mg, C_{FA}= 1M	54	956	319	This work
5Pd-M_3U_1-600	6.2wt%, T=150°C, 100mg, C_{FA}= 1M	20	1275	425	This work
Pd/g-C_3N_4	1.1wt%, 25 °C, 2h, 100 mg, 1FA:9SF 6M	65	383	128	[15]
Pd/mp-g-C_3N_4	3.2 wt%,60 °C, 2h, 40 mg, SF[2] 4M	23	520	173	[16]
Pd/mp-g-C_3N_4	9.5wt%, 25 °C, 3h, 50 mg, FA 1M	123	92	31	[17]
Pd/C_3N_4	5wt%, 60 °C, 200 min, 100 mg, 1FA:9SF 1M	-	259	86	[18]
Pd/C_3N_4	5wt%,60 °C, 200 min, 100 mg, FA 1M	-	73	24	[18]
Pd-Ru/C_3N_4	5wt%,60 °C, 200 min, 100 mg, FA 1M	-	61	20	[18]
Pd-Pt/g-C_3N_4	1.01wt%, 25 °C, 2h, 100 mg, 1FA:9SF[2] 6M	65	478	159	[15]

[1]TOF are calculated at 3h in all cases, [2]SF: Sodium formate.

The turnover frequency TOF (TOF=TON/h) is calculated at 3h, for our catalysts. The obtained TON and TOF for our catalysts suppurates the published values in the literature due more likely to the higher reaction temperature used. Clearly, the lowest dispersion and lower loading is beneficial for the calculation of the specific activity, with 5Pd-M-600 sample the most active one. Within the series, the catalysts treated at 600ºC shows higher specific activity and we choose to use that series in hydrodeoxygenation reaction.

IV.1.2 Bimetallic catalysts

For this reaction, we have chosen to present first the results obtained on Pd catalysts and then those obtained on bimetallic catalysts.

IV.1.1. Pd-based catalysts

The catalytic activity of all prepared Pd nanoparticles supported on carbon nitride in formic acid dehydrogenation in terms of formic acid conversion and generated gas pressure is presented in Figure IV.1.

Only two catalysts reach almost complete formic acid dehydrogenation, **5Pd-M$_1$U$_3$-600 and 5Pd-M$_1$U$_3$-550 with 98% and 96% conversion respectively**. Here it is the place to mention that those catalysts showed **higher Pd loadings (around 8 wt.%).** Nevertheless, the highest Pd loading it is not necessary an indication for high conversion, 5Pd-M$_3$U$_1$-550 sample present one of the lowest conversion for a very high metal content 11 wt.% Pd. On the other hand, these two samples present the lowest particle size suggesting that **the conversion is guided by the availability of the sites on the surface.**

The increase in the calcination temperature of the support also positively affects formic acid dehydrogenation. **The FA conversion increased from 51 to 88% for 5Pd-M-550 and 5Pd-M-600 sample, respectively**. In this particular case it appears more an **effect of support surface increase and C/H ratio decrease** that of Pd loadings and size. The initial hydrogen generation rates (slope of the pressure curve at initial time of reaction) are very different for both samples, indicating not only a different initial rate but also a different rate of deactivation

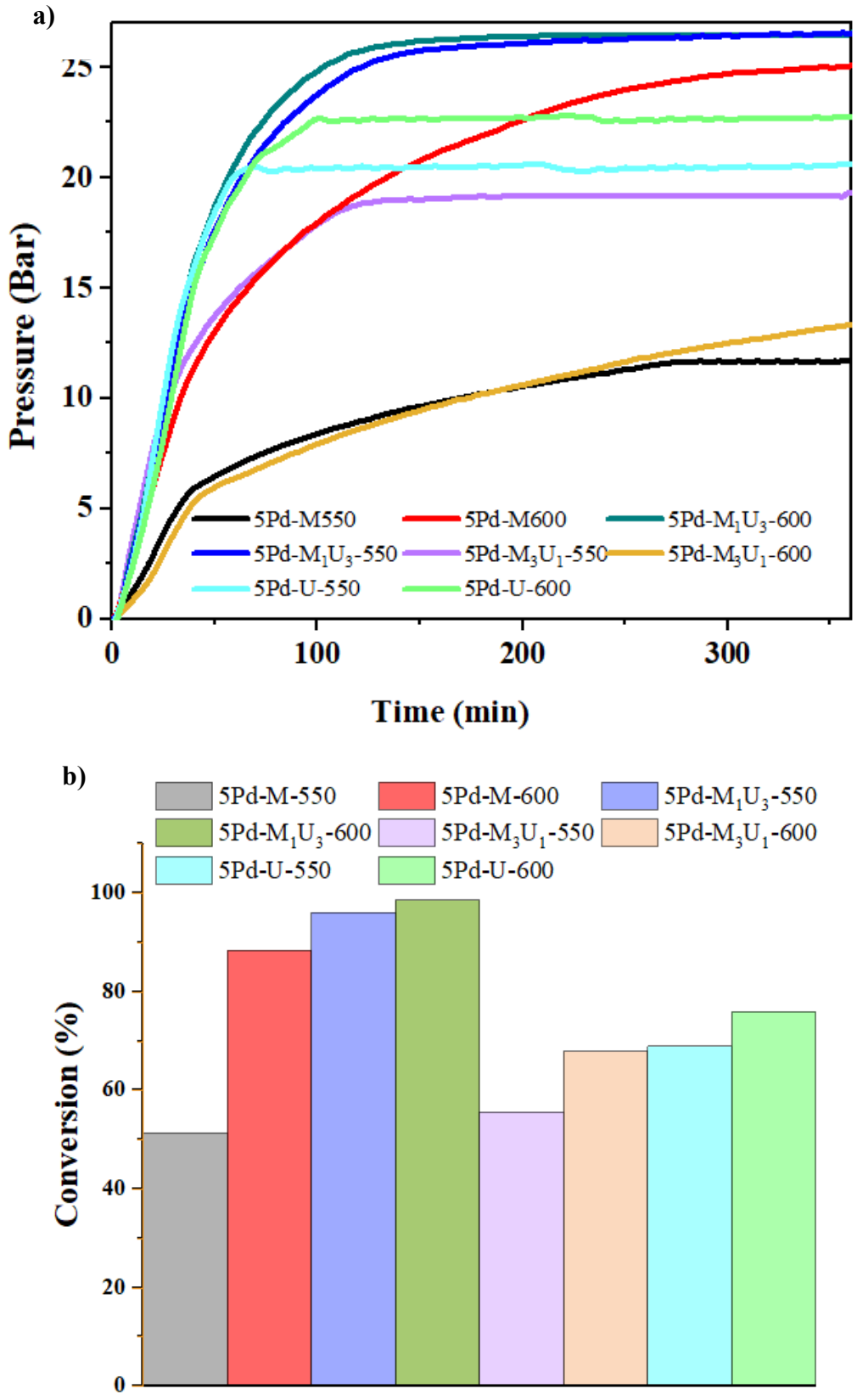

Figure IV.1: a) Generated gas pressure and b) formic acid conversion over different 5Pd-MxUy -T catalysts (T=150°C, time=6h, m_{cata} =100mg, V=20mL and C_{FA} =1M)

(when the curve tend to a constant value). It appears that **the increase of aromaticity (lower C/H ratio) results in higher electron density transfer from N to Pd (also observed by the important band at 220 nm for the 5Pd-M-600 sample) having a positive effect on hydrogen production**.

For the samples prepared from urea precursor, the 5Pd-U-550 catalyst reached equilibrium within 65 minutes, generating a total gas pressure of 20.6 bar and achieving corresponding to 69% of formic acid conversion. **5Pd-U-600 catalyst requires a longer reaction time (95 min) to reach equilibrium but produced a higher total gas pressure and conversion (75%).** It has been reported that carbon nitride synthesized from urea at 500–600°C typically exhibits a BET surface area ranging from 32 to 52 m^2/g and pore sizes between 40 and 58 nm [1,2]. In contrast, the 5Pd-M-550 and 5Pd-M_3U_1-600 samples, present lower BET surface areas of 12 m^2/g and 20 m^2/g, explaining its lower catalytic performance.

Table IV.1: Total gas volume, CO_2 concentration in liquid ((bi)carbonates and in gas phase and carbon balance.

Catalyst	Total Volume (CO_2 +H_2) mL	CO_2 Volume (mL)	C (bi)carbonate (M)	Carbon Balance (%)
5Pd-M-550	246	101	0.002	73
5Pd-M-600	560	238	0.018	67
5Pd-M_1U_3-550	608	268	0.028	67
5Pd-M_1U_3-600	624	270	0.011	65
5Pd-M_3U_1-550	259	91.4	0.019	66
5Pd-M_3U_1-600	438	182	0.012	75
5Pd-U-550	384	155	0.006	68
5Pd-U-600	435.	178	0.010	64

The total gas volume and CO_2 concentration in liquid ((bi)carbonates) and in gas phase are listed in Table 4. Only H_2 and CO_2 are expected in gas phase with an equimolar ratio. The estimated highest total gas in respect to the measured CO_2 **indicates some dissolution of CO_2 as (bi)carbonates in the continuous phase and also the loss of CO_2 by "fizzing" during the opening of the reactor** due to the change in equilibrium conditions at atmospheric pressure. This process is responsible for the carbon balance decrease to 70-75 % for all samples. The presence of basic functional groups on support surface favours the simultaneous protonation and reduction of CO_2 to carbonates. [3,4].

IV.1.1.1. Effect of tetrahydrofuran (THF) solvent

We further evaluated the effect of using of **the tetrahydrofuran (THF) as solvent** on the catalytic activity of a selected 5Pd-M3U1-600 catalyst, the obtained results are compared to those obtained using water as solvent (figure IV.2) and the values are summarized in table IV.2.

Table IV.2. Generated total volume of gas and CO_2 concentration for the reactions performed in water and THF

	Total Volume (ml)	**CO_2 volume (ml)**	**CO_2/CO ratio**
5Pd-M_1U_3-600 H_2O	438.4	175.93	95/5
5Pd-M_1U_3-600 THF	483.2	138.21	90/10

The generated pressure in THF is lower to that generated in water due to the difference in boiling point of the solvents and the higher dissolution of hydrogen. The formic acid conversion is similar (92 %) with some differences observed in the generated total gas and CO_2. Slightly **higher volume of CO was produced in THF** but still the reaction remains very selective to CO_2. From these results, we can confirm that the estimated highest total gas in respect to the measured CO_2 observed previously, was not only responsible for the carbon balance decrease to 70-75 % for all samples but also for the **small amount of formed CO formed through dehydration measured only for 5Pd-M_3U_1-600 sample** in Table IV.2).

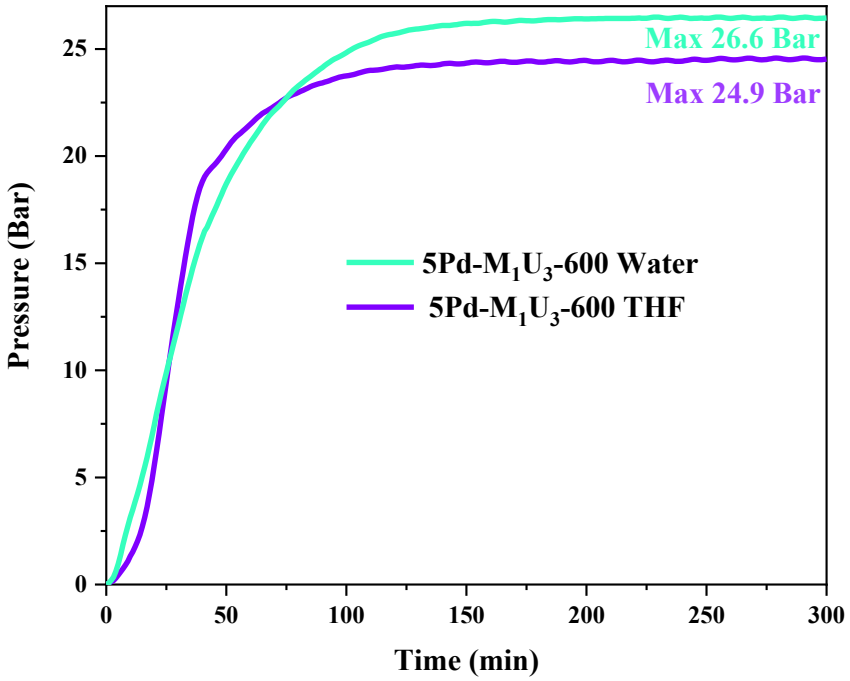

Figure VI.2. Comparison of formic acid dehydrogenation reaction in water and THF solvents

IV.1.1.2. Reactivity-structure correlation

If we represent the FA conversion variation vs. textural properties of the samples a clear tendency is observed, higher the BET surface higher the conversion (Figure 5a). The only exception is made by 5Pd-M_3U_1-550 sample resulting in poor conversion in respect to its surface area. This sample presents the lowest average pore diameter of all samples and the highest Pd particle size (Figure 5b) for the highest Pd loading indicating that the dehydrogenation reaction is much more sensitive to particle size and dispersion than to the metal loading. **The higher surface of the support and higher nitrogen content benefits the dispersion of Pd resulting in very active catalysts**.

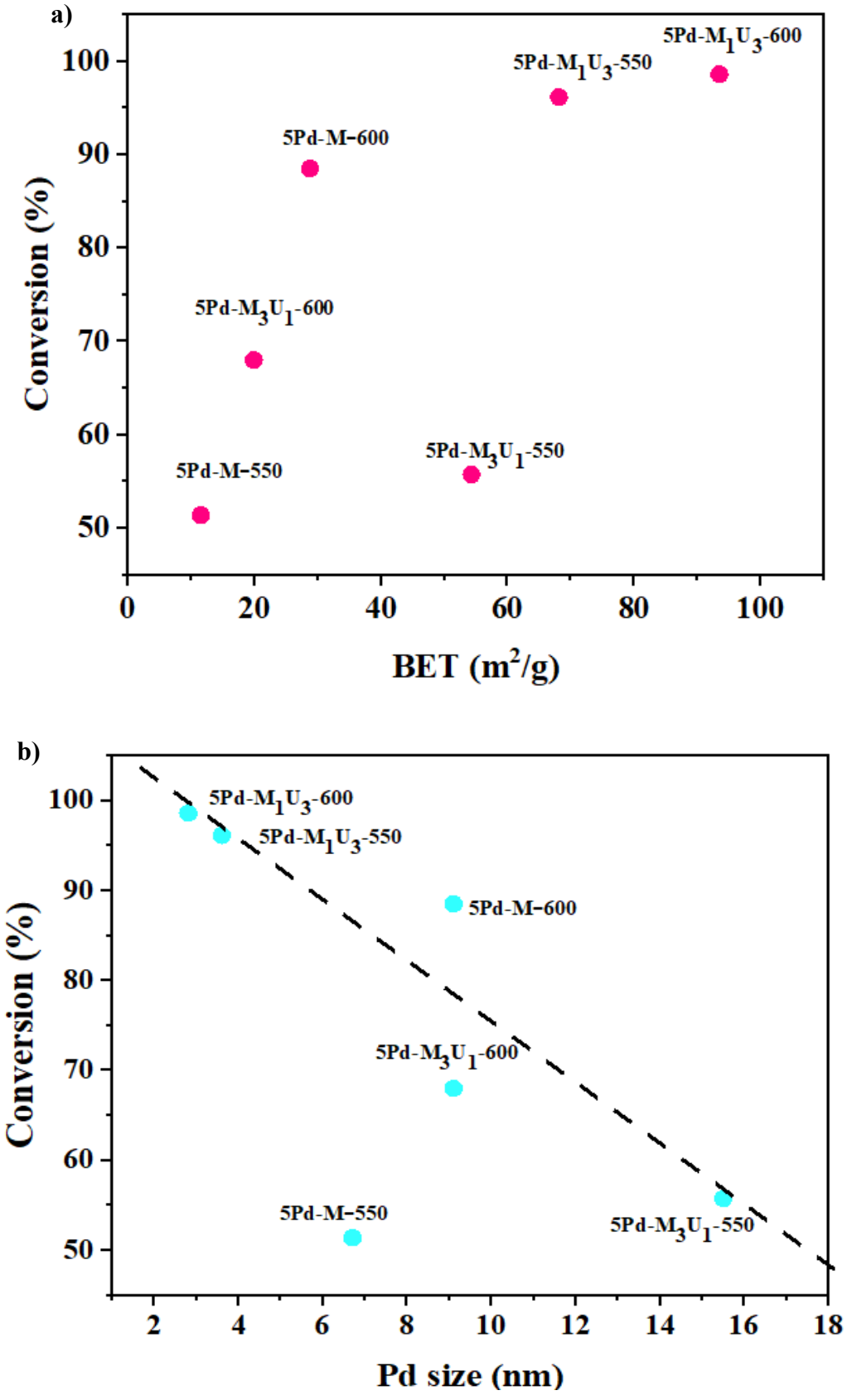

Figure IV.3: a) FA conversion vs. BET surface area and b) FA conversion vs. Pd particle size.

In summary we can conclude that **the support improves palladium dispersion and anchoring and enhances the mass transfer of formic acid to and out of active sites**.

On the other hand, **higher dispersion and higher C/H ratio increase the electrons density of the metal particles by assuring the electron transfer from N-atoms in the π-conjugated systems directly to Pd** [5]. On the contrary, the real metal loading appears less important, 5Pd-M_3U_1-550 catalyst possess the highest palladium content (11.13 wt%) but exhibited low formic acid conversion.

Based on the obtained data and literature [6–9], we can suggest that the adsorption of FA molecules on the catalyst surface needs higher surface. The adsorbed formates are the proposed intermediates of dehydrogenation reaction [10–14] and are formed after O-H bond cleavage, resulting in stable bidentate ($HCOO_B$) or monodentate ($HCOO_M$) formates on the active surface. Then, CO_2 and H_2 are formed after C-H bond cleavage in the final stage. The rapid increase of the gas pressure in the initial stage indicates a high initial velocity of H_2/CO_2 formation, where the desorption of the gases is more rapid than the adsorption of the reactants. Nevertheless, **at higher temperature the adsorption prevails over the desorption causing a catalyst deactivation.** The catalysts that show higher initial rate of reaction are the catalysts that reach higher conversion working in a range where the adsorption and desorption rates are similar. Any change that produces a different velocities of adsorption/desorption results in catalyst deactivation and lower final formic acid conversion. The transfer of electron density in the heterojunction between the semiconductor C_3N_4 and metal enriches Pd electron density and helps the desorption of the products.

Although difficult to compare to other catalyst due to the disparity of used conditions and formulation, in Table 5 we present some similar works published in the literature. Some of the values (TON) are directly indicated in these studies, while others were re-calculated by us using the relationship mentioned above.

Table. IV.3. TON and TOF for different palladium-based catalysts.

Catalyst	Reaction conditions	BET specific surface area (m^2/g)	TON	TOF[1] (h^{-1})	Ref
5Pd-M-550	6.8wt%, T=150°C, 100mg, C_{FA}= 1M	11	651	217	This work
5Pd-M-600	6.6wt%, T=150°C, 100mg, C_{FA}= 1M	29	1573	524	This work
5Pd-M_1U_3-550	7.8wt%, T=150°C, 100mg, C_{FA}= 1M	68	467	156	This work
5Pd-M_1U_3-600	8.2wt%, T=150°C, 100mg, C_{FA}= 1M	93	581	194	This work
5Pd-M_3U_1-550	11wt%, T=150°C, 100mg, C_{FA}= 1M	54	956	319	This work
5Pd-M_3U_1-600	6.2wt%, T=150°C, 100mg, C_{FA}= 1M	20	1275	425	This work
Pd/g-C_3N_4	1.1wt%, 25 °C, 2h, 100 mg, 1FA:9SF 6M	65	383	128	[15]
Pd/mp-g-C_3N_4	3.2 wt%,60 °C, 2h, 40 mg, SF[2] 4M	23	520	173	[16]
Pd/mp-g-C_3N_4	9.5wt%, 25 °C, 3h, 50 mg, FA 1M	123	92	31	[17]
Pd/C_3N_4	5wt%, 60 °C, 200 min, 100 mg, 1FA:9SF 1M	-	259	86	[18]
Pd/C_3N_4	5wt%,60 °C, 200 min, 100 mg, FA 1M	-	73	24	[18]
Pd-Ru/C_3N_4	5wt%,60 °C, 200 min, 100 mg, FA 1M	-	61	20	[18]
Pd-Pt/g-C_3N_4	1.01wt%, 25 °C, 2h, 100 mg, 1FA:9SF[2] 6M	65	478	159	[15]

[1]TOF are calculated at 3h in all cases, [2]SF: Sodium formate.

The turnover frequency TOF (TOF=TON/h) is calculated at 3h, for our catalysts. The obtained TON and TOF for our catalysts suppurates the published values in the literature due more likely to the higher reaction temperature used. Clearly, the lowest dispersion and lower loading is beneficial for the calculation of the specific activity, with 5Pd-M-600 sample the most active one. Within the series, the catalysts treated at 600ºC shows higher specific activity and we choose to use that series in hydrodeoxygenation reaction.

IV.2. HMF hydrodeoxygenation

IV.2.1. Pd-based catalysts

For the HDO reaction, we have selected tetrahydrofuran (THF) as a solvent in order to prevent 5-HMF side reactions, such as rehydration and polymerization and to increase the solubility of the generated hydrogen in the continuous phase to facilitate the hydrogenation/hydrogenolysis reactions. That is why, the FAD reaction was repeated over 5Pd-M_1U_3-600 sample in (THF) solvent (Figure S1). The generated pressure in THF is lower to that generated in water due to the difference in boiling point of the solvents and the higher dissolution of hydrogen. The FA conversion is similar (92%) with some differences observed in the generated total gas and CO_2. Slightly higher volume of CO was produced in THF but still the reaction remain very selective to CO_2. **As in water the extension of the FAD reaction is high and the produced hydrogen is sufficient to carry out the planned HDO experiment, exceeding the initial HMF concentration.**

There are two known pathways for the formation of **2,5-dimethylfuran (2,5-DMF)** summarized in Scheme 1. The first one involves 5-HMF hydrogenolysis to 5-methylfuran (5-MF) further hydrogenated to 5-methylfurfuryl alcohol (5-MFA), which is further converted to 2,5-DMF through hydrogenolysis of its carbonyl group (C=O). In the second pathway HMF is hydrogenated to 2,5-bis (hydroxymethyl)furan (BHMF), the latte converted to 5-MFA by hydrogenolysis and furtherly transformed to 2,5-DMF.

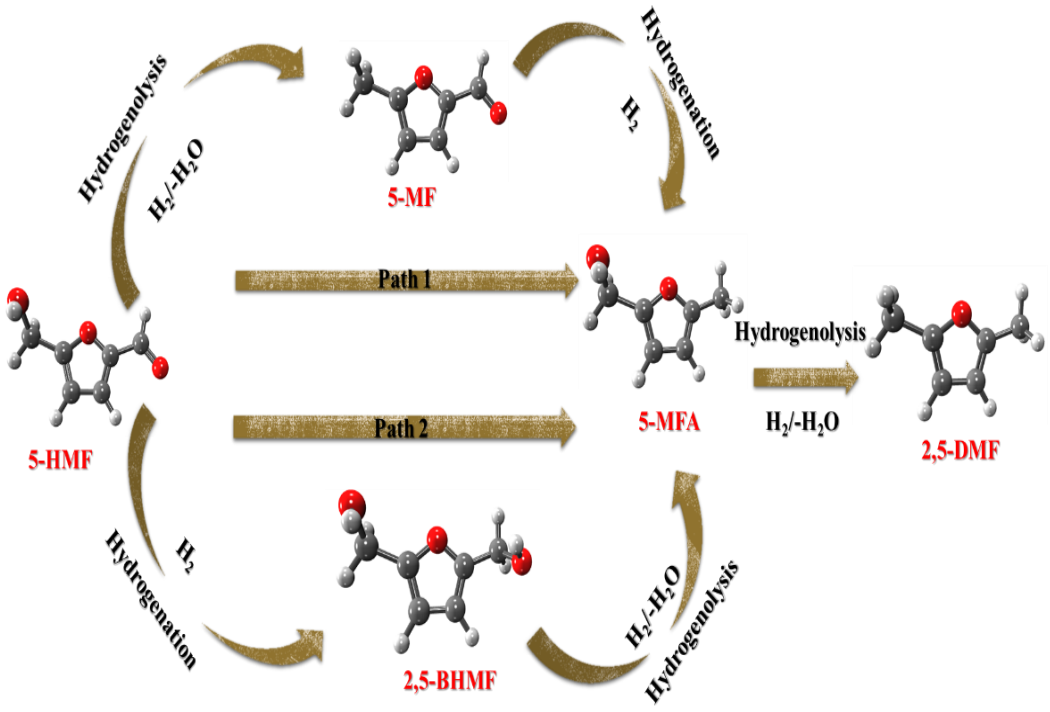

Figure IV.7: Pathways to HMF transformation to 2,5 DMF

The efficiency of 5Pd-M-600, 5Pd-M_1U_3-600 and 5Pd-M_3U_1-600 in catalytic hydrodeoxygenation/hydrogenation of 5-HMF to 2,5-DMF in THF solvent in the presence of FA as H_2 donor is presented in Figure IV.8.

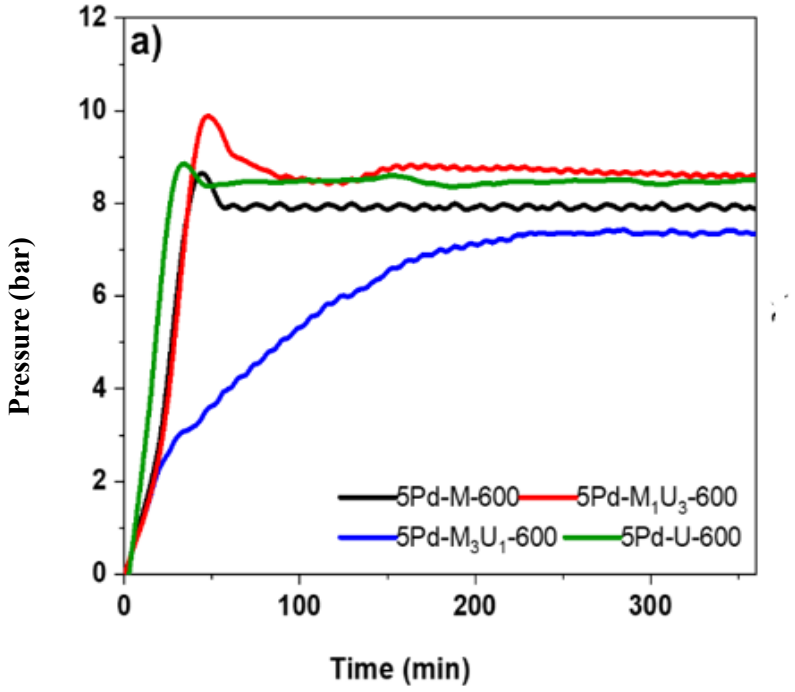

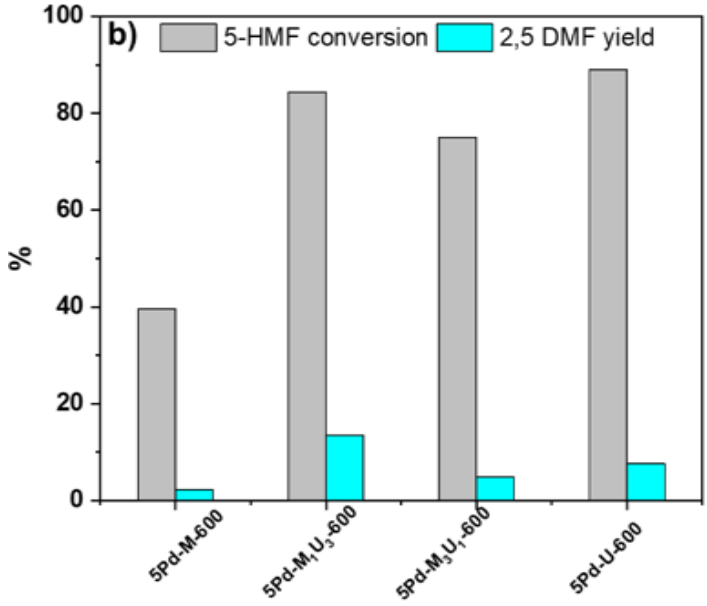

Figure IV.8: a) Generated gas pressure and b) 5-HMF conversion and 2,5-DMF yield over different 5Pd-MxUy -600 catalysts (T=150°C, time=6h, m_{cata} =100mg, V=20mL and n_{FA} /$n_{5\text{-}HMF}$ =10)

The generated total gas pressure was comparable for 5Pd-M_1U_3-600, 5Pd-M-600 and 5Pd-U-600 samples reaching 8-9 bars. However, the 5Pd-M_3U_1-600 sample exhibited lower gas pressure and reached equilibrium at relatively longer times in comparison to the other samples. All samples showed lower pressure in comparison to the FAD reaction suggesting the use of hydrogen in the moment of production. The highest HMF conversion and 2-5 DMF was observed for the 5Pd-U-600 and 5Pd-M_1U_3-600 samples followed by 5Pd-M_3U_1-600 and 5Pd-M-600. For all samples (Figure 7) along with the target products 2,5-DMF, the 5-MF and 5-MFA are detected as intermediates as well as humins resulted from 5-HMF condensation, which explains the high conversion of 5-HMF and poor 2,5-DMF yields. The 2,5-BHMF was not detected during the analysis, thus confirming that the reaction of the hydrogenation of 5-HMF goes principally through the first pathway, in accordance with the literature which reported the 5-MF pathway over palladium-based catalysts [19–22].

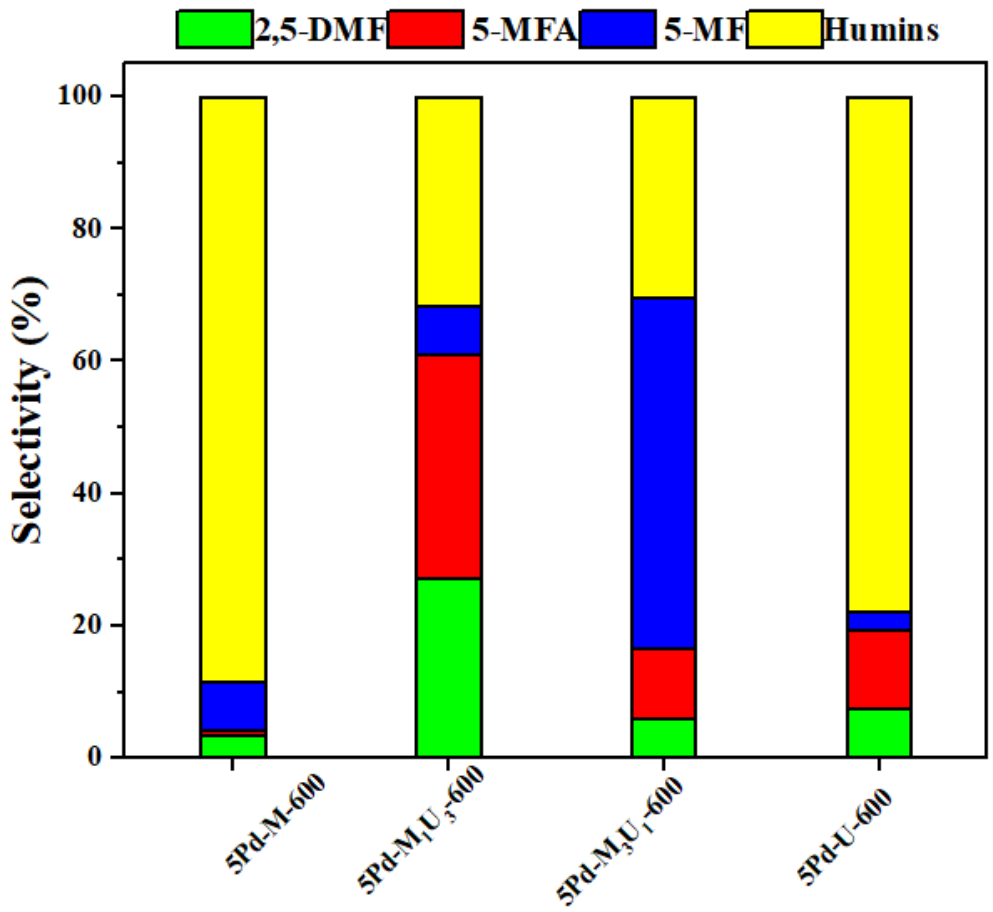

Figure IV.9: Products selectivity over different 5Pd-MxUy -600 catalysts (T=150°C, time=6h, m_{cata} =100mg, V=20mL and n_{FA} /$n_{5\text{-}HMF}$ =10)

On the other hand, the 5-HMF transformation to 2,5-DMF performances appears to depend on support composition. It was found that the presence of urea along with melamine for the preparation of the support highly improved the utile 5-HMF conversion resulting in more reaction products and low humins fraction. The presence of more cyano groups and Pd atoms positioned close to N-atoms, as suggested by UV-VIS, for these samples could be the reason for this. A confirmation of this statement is the very different product distribution for 5Pd-M_3U_1 and 5Pd-M-600, samples with similar particle size, Pd dispersion and metal loading (6.6wt.% for 5Pd-M-600 *vs* 6.2wt.% for 5Pd-M_3U_1).

Also the specific surface plays in favor of the product selectivity, the higher the specific area the higher the HDO products yields. 5Pd-M_1U_3-600 sample with its higher surface facilitates the adsorption of 5-HMF and orients the reaction to 2,5-DMF and/or intermediates (5-MF and 5-MFA) suppressing the humins formation. **The small Pd size can be also considered as**

important factor for 5-HMF hydrodeoxygenation, especially in the transformation of the 5-MF and 5-MFA into 2,5-DMF. Indeed, 5Pd-M_1U_3-600 catalyst **which shows the smallest Pd size shows the highest 2,5- DMF yield**. The 5Pd-U-600 catalyst demonstrated higher 2,5-DMF yield (7.6%) in comparison to 5Pd-M-600 (2.3%) but present the same product distribution forming mainly humins.

IV.2.2. Bimetallic catalysts

For the HDO reaction, we have selected tetrahydrofuran (THF) as a solvent in order to prevent 5-HMF side reactions, such as rehydration and polymerization and to increase the solubility of the generated hydrogen in the continuous phase to facilitate the hydrogenation/hydrogenolysis reactions. That is why, the FAD reaction was repeated over 5Pd-M_1U_3-600 sample in (THF) solvent (Figure S1). The generated pressure in THF is lower to that generated in water due to the difference in boiling point of the solvents and the higher dissolution of hydrogen. The FA conversion is similar (92%) with some differences observed in the generated total gas and CO_2. Slightly higher volume of CO was produced in THF but still the reaction remain very selective to CO_2. **As in water the extension of the FAD reaction is high and the produced hydrogen is sufficient to carry out the planned HDO experiment, exceeding the initial HMF concentration.**

There are two known pathways for the formation of **2,5-dimethylfuran (2,5-DMF)** summarized in Scheme 1. The first one involves 5-HMF hydrogenolysis to 5-methylfuran (5-MF) further hydrogenated to 5-methylfurfuryl alcohol (5-MFA), which is further converted to 2,5-DMF through hydrogenolysis of its carbonyl group (C=O). In the second pathway HMF is hydrogenated to 2,5-bis (hydroxymethyl)furan (BHMF), the latte converted to 5-MFA by hydrogenolysis and furtherly transformed to 2,5-DMF.

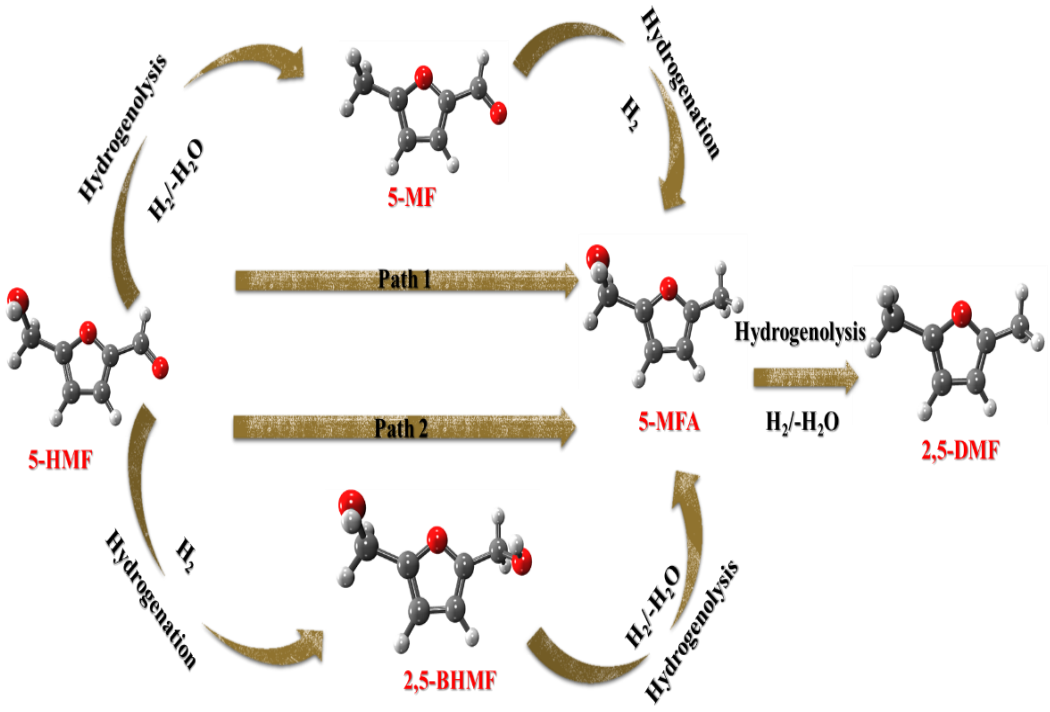

Figure IV.7: Pathways to HMF transformation to 2,5 DMF

The efficiency of 5Pd-M-600, 5Pd-M_1U_3-600 and 5Pd-M_3U_1-600 in catalytic hydrodeoxygenation/hydrogenation of 5-HMF to 2,5-DMF in THF solvent in the presence of FA as H_2 donor is presented in Figure IV.8.

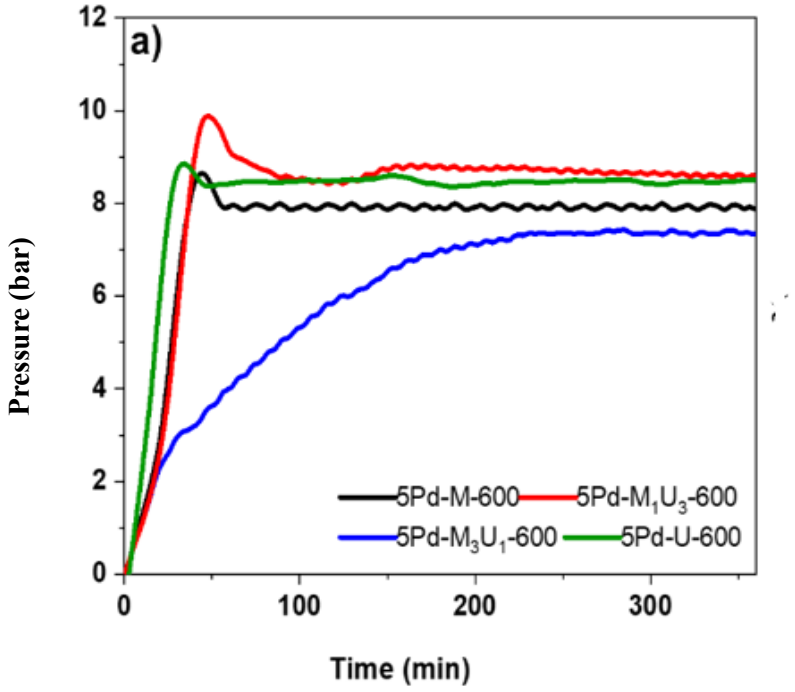

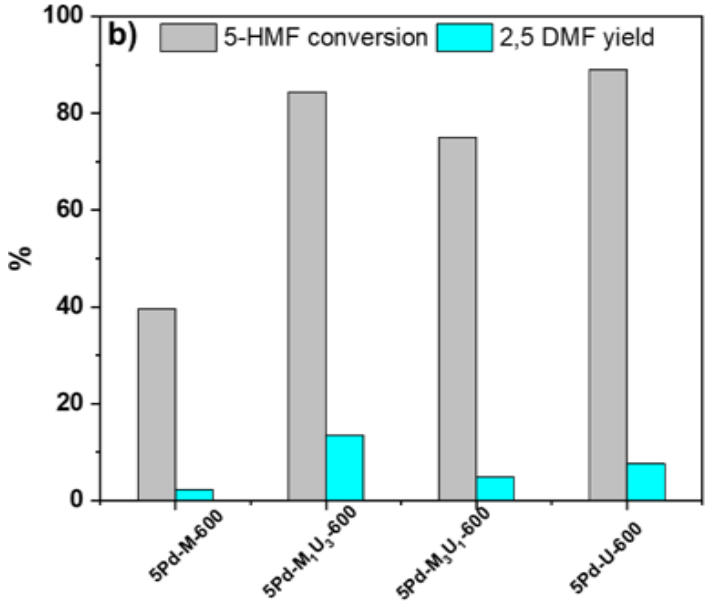

Figure IV.8: a) Generated gas pressure and b) 5-HMF conversion and 2,5-DMF yield over different 5Pd-MxUy -600 catalysts (T=150°C, time=6h, m_{cata} =100mg, V=20mL and n_{FA} /$n_{5\text{-}HMF}$ =10)

The generated total gas pressure was comparable for 5Pd-M_1U_3-600, 5Pd-M-600 and 5Pd-U-600 samples reaching 8-9 bars. However, the 5Pd-M_3U_1-600 sample exhibited lower gas pressure and reached equilibrium at relatively longer times in comparison to the other samples. All samples showed lower pressure in comparison to the FAD reaction suggesting the use of hydrogen in the moment of production. The highest HMF conversion and 2-5 DMF was observed for the 5Pd-U-600 and 5Pd-M_1U_3-600 samples followed by 5Pd-M_3U_1-600 and 5Pd-M-600. For all samples (Figure 7) along with the target products 2,5-DMF, the 5-MF and 5-MFA are detected as intermediates as well as humins resulted from 5-HMF condensation, which explains the high conversion of 5-HMF and poor 2,5-DMF yields. The 2,5-BHMF was not detected during the analysis, thus confirming that the reaction of the hydrogenation of 5-HMF goes principally through the first pathway, in accordance with the literature which reported the 5-MF pathway over palladium-based catalysts [19–22].

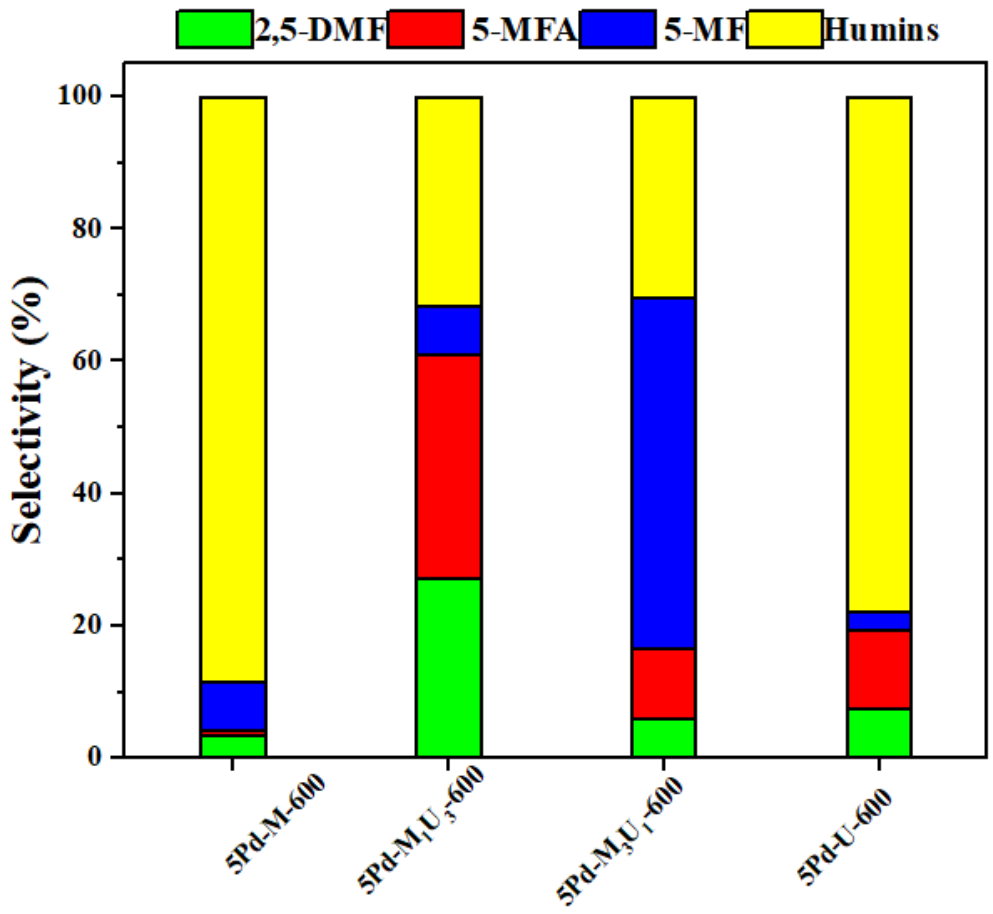

Figure IV.9: Products selectivity over different 5Pd-MxUy -600 catalysts (T=150°C, time=6h, m_{cata} =100mg, V=20mL and n_{FA} /$n_{5\text{-}HMF}$ =10)

On the other hand, the 5-HMF transformation to 2,5-DMF performances appears to depend on support composition. It was found that the presence of urea along with melamine for the preparation of the support highly improved the utile 5-HMF conversion resulting in more reaction products and low humins fraction. The presence of more cyano groups and Pd atoms positioned close to N-atoms, as suggested by UV-VIS, for these samples could be the reason for this. A confirmation of this statement is the very different product distribution for 5Pd-M_3U_1 and 5Pd-M-600, samples with similar particle size, Pd dispersion and metal loading (6.6wt.% for 5Pd-M-600 *vs* 6.2wt.% for 5Pd-M_3U_1).

Also the specific surface plays in favor of the product selectivity, the higher the specific area the higher the HDO products yields. 5Pd-M_1U_3-600 sample with its higher surface facilitates the adsorption of 5-HMF and orients the reaction to 2,5-DMF and/or intermediates (5-MF and 5-MFA) suppressing the humins formation. **The small Pd size can be also considered as**

important factor for 5-HMF hydrodeoxygenation, especially in the transformation of the 5-MF and 5-MFA into 2,5-DMF. Indeed, 5Pd-M_1U_3-600 catalyst **which shows the smallest Pd size shows the highest 2,5- DMF yield**. The 5Pd-U-600 catalyst demonstrated higher 2,5-DMF yield (7.6%) in comparison to 5Pd-M-600 (2.3%) but present the same product distribution forming mainly humins.

IV.2.2.1. Catalyst recyclability studies

The reusability of the catalyst was evaluated through consecutive reaction cycles using the XXXCN catalyst under identical reaction conditions. After each reaction run, the catalyst was recovered by filtration, thoroughly washed with solvent to remove residual reactants and products, and dried overnight prior to reuse. The results are presented in figure IV.11.

As shown by the results, the conversion of 5-HMF remained very high during the first three cycles, reaching % in the first and second runs and slightly decreasing to 99% in the third run. A more pronounced decrease was observed in the fourth cycle, where the conversion dropped to 95%, indicating the onset of gradual catalyst deactivation upon repeated reuse.

Regarding product distribution, the selectivity toward 2,5-DMF gradually decreased with each successive cycle, from % in the first run to 49.34% in the fourth run. At the same time, the formation of by-products such as 5-MFA and 5-MF increased, suggesting changes in the catalytic behaviour during reuse. This shift in selectivity may be attributed to partial loss of active metal sites, metal sintering, surface oxidation, or deposition of carbonaceous species, which can affect hydrogenation and hydrodeoxygenation pathways.

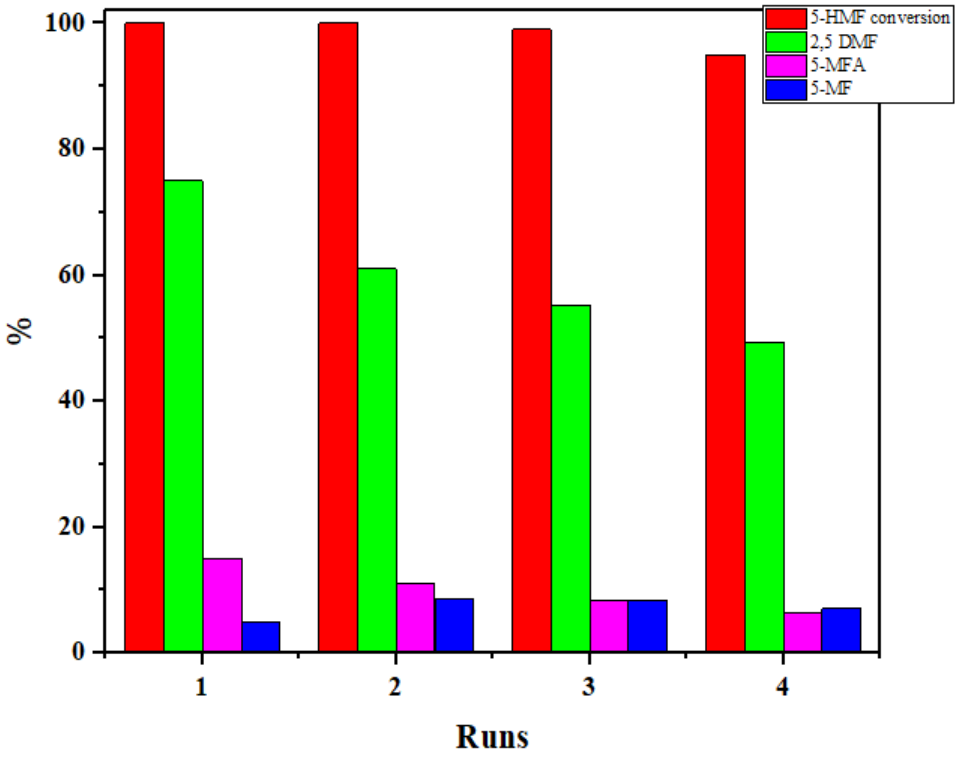

Figure IV.14: Recyclability of 5XXX-CN

Globaly, the catalyst **demonstrates good stability in terms of conversion, but a gradual decline in selectivity toward the desired product is observed upon reuse**. These results indicate that while the catalyst maintains high activity, structural or surface modifications during repeated cycles influence product selectivity, highlighting the importance of regeneration or optimization strategies to improve long-term catalytic performance.

IV.3. Partial conclusion

This chapter investigated Pd-based mono- and bimetallic catalysts supported on carbon nitride for the coupled reactions of formic acid dehydrogenation and the hydrodeoxygenation of 5-hydroxymethylfurfural (HMF) to 2,5-dimethylfuran (2,5-DMF). The results demonstrate that catalytic performance is strongly governed by a combination of metal dispersion, support properties, and metal–metal interactions rather than by metal loading alone.

The catalytic evaluation demonstrated that the performance of Pd-based catalysts strongly depends on support properties, Pd dispersion, and bimetallic composition. In formic acid dehydrogenation, monometallic Pd catalysts achieved conversions between 51 and 98%,

with the best results obtained for 5Pd-M1U3-600 and 5Pd-M1U3-550 (98 and 96%, respectively). Higher BET surface area and smaller Pd particle size were identified as the main factors governing activity, while metal loading showed a less significant influence. The catalysts calcined at 600 °C exhibited the highest specific activities, reaching TON and TOF values of 1573 and 524 h^{-1}, respectively.

The incorporation of a second metal further enhanced catalytic performance. PdCo catalysts outperformed both monometallic Pd and PdNi systems, achieving up to 98% formic acid conversion and improving the carbon balance to 78%, highlighting the beneficial synergistic interaction between Pd and Co.

For the hydrodeoxygenation of HMF, all catalysts showed high HMF conversions (>75%), confirming the effectiveness of formic acid as an in situ hydrogen source. However, product selectivity strongly depended on catalyst composition. While monometallic Pd catalysts produced low 2,5-DMF yields (~10%), PdCo catalysts significantly improved selectivity. The $5Pd_2Co_1$–CN catalyst exhibited the best performance, reaching a 2,5-DMF yield of approximately 60%, with a TON of 115.8 and a TOF of 19.3 h^{-1}. In contrast, PdNi catalysts showed lower DMF yields (<20%) and higher humin formation.

Reusability tests confirmed the good stability of XX_1–CN, maintaining HMF conversions above % after four cycles. Nevertheless, the selectivity toward 2,5-DMF gradually decreased from % to %, indicating progressive catalyst deactivation during reuse. Overall, the results identify PdCo-supported carbon nitride catalysts, particularly XX_1–CN, as the most promising systems for the coupled formic acid dehydrogenation and selective conversion of HMF into 2,5-DMF.

References:

[1] Q. Su, J. Sun, J. Wang, Z. Yang, W. Cheng, S. Zhang, Catalysis Science & Technology, (2014) 1556–1562. https://doi.org/10.1039/c3cy00921a.

[2] E. Farahi, S. You, I. Concina, Understanding Graphitic Carbon Nitride as Photocatalyst : A Case Study on Thermal Engineering of Physical and Chemical Features, (2024). https://doi.org/10.1002/pssa.202300844.

[3] S. Jing, X. Cao, L. Zhong, X. Peng, R. Sun, Industrial Crops & Products E ff ectively enhancing conversion of cellulose to HMF by combining in-situ carbonic acid from CO_2 and metal oxides, Ind. Crop. Prod. 126 (2018) 151–157. https://doi.org/10.1016/j.indcrop.2018.10.028.

[4] S. Jing, X. Cao, L. Zhong, X. Peng, X. Zhang, S. Wang, R. Sun, In Situ Carbonic Acid from CO_2 : A Green Acid for Highly E ff ective Conversion of Cellulose in the Presence of Lewis acid, (2016) 2–11. https://doi.org/10.1021/acssuschemeng.6b00623.

[5] I. Majeed, U. Manzoor, F.K. Kanodarwala, M.A. Nadeem, E. Hussain, H. Ali, A. Badshah, J.A. Stride, M.A. Nadeem, Catalysis Science & Technology, (2018) 1183–1193. https://doi.org/10.1039/c7cy02219k.

[6] G. Laurenczy, F. Joó, L. Nádasdi, Formation and characterization of water-soluble hydrido-ruthenium (II) complexes of 1, 3, 5-triaza-7-phosphaadamantane and their catalytic activity in hydrogenation of CO_2 and HCO_3^-in aqueous solution, Inorg. Chem. 39 (2000) 5083–5088. https://doi.org/10.1021/ic000200b

[7] J. Elek, L. Nádasdi, G. Papp, G. Laurenczy, F. Joó, Homogeneous hydrogenation of carbon dioxide and bicarbonate in aqueous solution catalyzed by water-soluble ruthenium (II) phosphine complexes, Appl. Catal. A Gen. 255 (2003) 59–67. https://doi.org/10.1016/S0926-860X(03)00644-6

[8] A.M. Ruppert, M. Jędrzejczyk, N. Potrzebowska, K. Kaźmierczak, M. Brzezińska, O. Sneka-Płatek, P. Sautet, N. Keller, C. Michel, J. Grams, Supported gold-nickel nano-alloy as a highly efficient catalyst in levulinic acid hydrogenation with formic acid as an internal hydrogen source, Catal. Sci. Technol. 8 (2018) 4318–4331. https://doi.org/10.1039/c8cy00462e.

[9] X. Shao, J. Xu, Y. Huang, X. Su, H. Duan, X. Wang, T. Zhang, Pd/C_3N_4 nanocatalyst for highly efficient hydrogen storage system based on potassium bicarbonate/formate, AIChE J. 62 (2016) 2410–2418. https://doi.org/10.1002/aic.15218

[10] M. Karatok, H.T. Ngan, X. Jia, C.R.O. Connor, J.A. Boscoboinik, D.J. Stacchiola, P. Sautet, R.J. Madix, Achieving Ultra-High Selectivity to Hydrogen Production from Formic Acid on Pd − Ag Alloys, (2023). https://doi.org/10.1021/jacs.2c11323.

[11] Y. Wang, Y. Qi, D. Zhang, C. Liu, New Insight into the Decomposition Mechanism of Formic Acid on Pd (111): Competing Formation of CO_2 and CO, (2014).

[12] S. Zhou, C. Qian, X. Chen, Comparative Theoretical Study of Adsorption and Dehydrogenation of Formic Acid , Hydrazine and Isopropanol on Pd (111) Surface, (2011) 726–734. https://doi.org/10.1007/s10562-011-0553-y.

[13] E. De Lyon, C. Umr, U. Claude, B. Lyon, L. De Chimie, Key Role of Anionic Doping for H_2 Production from Formic Acid on Pd(111), (2017). https://doi.org/10.1021/acscatal.6b03544.

[14] R. Zhang, H. Liu, B. Wang, L. Ling, Insights into the Preference of CO_2 Formation from HCOOH Decomposition on Pd Surface : A Theoretical Study, (2012). https://doi.org/10.1021/jp211900z

[15] X. Liu, P. Su, Y. Chen, B. Zhu, S. Zhang, W. Huang, g-C_3N_4 supported metal (Pd, Ag, Pt) catalysts for hydrogen-production from formic acid, (2018) 9449–9454. https://doi.org/10.1039/c8nj00404h.

[16] X. Shao, Pd/C_3N_4 Nanocatalyst for Highly Efficient Hydrogen Storage System Based on Potassium Bicarbonate / Formate, 62 (2016). https://doi.org/10.1002/aic.

[17] J.H. Lee, J. Ryu, J.Y. Kim, S.-W. Nam, J.H. Han, T.-H. Lim, S. Gautam, K.H. Chae, C.W. Yoon, Carbon dioxide mediated, reversible chemical hydrogen storage using a Pd nanocatalyst supported on mesoporous graphitic carbon nitride, J. Mater. Chem. A. 2 (2014) 9490–9495. https://doi.org/10.1039/C4TA01133C

[18] G.-L. Reactions, M. Mart, S. Ivanova, M.Á. Centeno, Formic Acid Dehydrogenation over Ru- and Pd-Based Catalysts: Gas- vs. Liquid-Phase Reactions, (2023). https://doi.org/10.3390/ma16020472

[19] R. Insyani, D. Verma, S.M. Kim, J. Kim, Direct one-pot conversion of monosaccharides into high-yield 2, 5-dimethylfuran over a multifunctional Pd/Zr-based metal–organic framework@ sulfonated graphene oxide catalyst, Green Chem. 19 (2017) 2482–2490. https://doi.org/10.1039/C7GC00269F

[20] M. Chatterjee, T. Ishizaka, H. Kawanami, Hydrogenation of 5-hydroxymethylfurfural in supercritical carbon dioxide–water: a tunable approach to dimethylfuran selectivity,

Green Chem. 16 (2014) 1543–1551. https://doi.org/10.1039/C3GC42145G

[21] Y. Chen, H. Guo, J. Yang, K. Xu, X. Lu, Y. Yang, H. Lin, L. Wu, L. Tan, G. Yang, N. Tsubaki, X. Gu, Y. Tang, Catalytic hydrodeoxygenation of 5-hydroxymethylfurfural to 2 , 5-dime - thylfuran over Pd-Co bimetallic catalysts supported on MoC x, Fuel. 361 (2024) 130682. https://doi.org/10.1016/j.fuel.2023.130682.

[22] D.S. Pisal, G.D. Yadav, Production of biofuel 2 , 5-dimethylfuran using highly efficient single-step selective hydrogenation of 5-hydroxymethylfurfural over novel Pd-Co / Al-Zr mixed oxide catalyst, Fuel. 290 (2021) 119947. https://doi.org/10.1016/j.fuel.2020.119947.

GENERAL CONCLUSION

In the last decades, the continuous restrictions related to climate change and CO_2 emissions have directed the research towards novel, clean and renewable sources able to produce and store energy. As an example, the Liquid Organic Hydrogen Carriers (LOHCs), organic compounds that can reversibly store and release hydrogen through catalytic processes. These systems offer several advantages over the traditional hydrogen storage methods like high energy density, ease of handling, and ability to maintain the existing liquid fuel infrastructure. Among others, formic acid (FA) is considered as promising hydrogen storage agent and versatile C1 building block for many industries.

The aim of this study was to develop effective catalytic system for the hydrodeoxygenation of 5-hydroxymethylfurfural (5-HMF) into valuable biofuel molecule, the 2,5-dimethylfuran (DMF) using formic acid as a hydrogen donor. This approach combines the conversion of biomass-derived compounds with the in-situ generation of hydrogen from formic acid, avoiding the use of external molecular hydrogen. The catalytic system comprises nanoparticles of Pd supported on carbon nitride, the effect of some parameters of support synthesis, like used precursors and temperature of thermal decomposition, on catalytic properties and reactivity was also studied. Another target of this study was to investigate the effect of a second metal addition (Co, Ni) on the activity and the performance stability in HDO of 5-HMF, over Pd/C_3N_4. A series of different C_3N_4 have been synthesized as a function of the initial precursors (melamine and urea) ratio and temperature of thermal treatment. The prepared catalysts have been characterized by several techniques, X-ray diffraction (XRD), specific area measurement (BET) and X-ray photoelectron spectroscopy (XPS).

The investigation, the synthesis, structural evolution, and physicochemical properties of Pd-based catalysts supported on graphitic carbon nitride (g-C_3N_4), including monometallic Pd systems and bimetallic PdCo and PdNi formulations. Particular attention was given to the effect of synthesis parameters (melamine/urea ratio and calcination temperature) and metal incorporation on texture, defect chemistry, metal dispersion, and electronic structure.

The synthesis strategy produced carbon nitride materials with carbon-rich but nitrogen-defective compositions close to the idealized “melon-type” g-C_3N_4 structure, with measured C/N molar ratios consistently around across all samples. Elemental analysis confirmed hydrogen contents between 0.99 and 2.12 wt%, indicating the presence of terminal –NH_x groups and

incomplete condensation. After metal incorporation, both carbon and nitrogen contents decreased to approximately 33–35 wt% C and 55–57 wt% N, while preserving an almost constant C/N ratio (~0.60–0.61), confirming that metal loading affects both elements proportionally rather than altering overall stoichiometry.

Textural properties were strongly governed by synthesis conditions. The introduction of urea significantly enhanced porosity and surface area, increasing BET values from 13–23 m^2/g (melamine-only samples) up to 98–106 m^2/g (urea-containing supports). The total pore volume increased accordingly from 0.041–0.069 cm^3/g to a maximum of 0.396 cm^3/g, demonstrating the key role of gas-evolving decomposition of urea in generating mesoporosity. After Pd incorporation, surface areas ranged broadly from 12 to 94 m^2/g, reflecting both pore blocking and metal-induced structural rearrangements.

Chemical analysis by ICP-OES showed that the nominal metal loading of 5 wt% was systematically exceeded in many cases. Monometallic Pd catalysts exhibited Pd contents ranging while bimetallic PdCo and PdNi systems maintained total metal contents between and wt%. This deviation is attributed to partial support loss during reduction and decomposition of carbon nitride induced by nitrate precursors.

XRD analysis confirmed the preservation of the g-C_3N_4 framework with characteristic reflections at $2\theta \approx 13°$ and 27°, corresponding to the (100) and (002) planes. Structural parameters revealed lattice constants of approximately a = 3.20–3.24 Å and c = 6.45–6.86 Å, with systematic contraction of the c parameter upon metal loading, indicating reduced interlayer spacing and stronger metal–support interactions. Palladium crystallite sizes varied significantly depending on composition, ranging from 2.8 nm to 15.4 nm. The smallest particles were obtained for urea-rich and bimetallic systems, particularly 5Pd–M_1U_3–600 (2.8 nm) and 5–CN (3.1 nm), while the largest aggregates were observed for Pd-rich or poorly stabilized formulations such as 5Pd–M_3U_1–550 (15.4 nm).

UV–Vis spectroscopy demonstrated systematic band gap modulation induced by defect engineering. A blue shift of the absorption edge was observed with increasing urea content and higher calcination temperature, associated with nitrogen vacancies and cyano-type defects. Additional spectral features confirmed the formation of reduced conjugation domains and modified electronic transitions. After Pd incorporation, optical absorption decreased in intensity

and new features appeared, including a weak plasmonic contribution around ~500 nm and charge transfer bands near ~220 nm, indicating electronic interaction between Pd and nitrogen sites.

XPS analysis confirmed that Pd exists in a electronically perturbed state, with Pd $3d_{5/2}$ and $3d_{3/2}$ peaks at approximately eV and. eV, respectively. A negative binding energy shift of eV relative to monometallic Pd was observed in bimetallic systems, confirming charge transfer from Co or Ni to Pd. Surface analysis also revealed that Pd surface concentration can differ significantly from bulk composition, indicating non-uniform metal distribution depending on synthesis route.

For formic acid dehydrogenation, Pd nanoparticles supported on carbon nitride achieved formic acid conversions ranging from 51% to 98%, depending strongly on support composition and Pd dispersion. The most active catalysts, 5Pd-M_1U_3-600 and 5Pd-M_1U_3-550, reached 98% and 96% conversion, respectively, with total gas volumes up to 624 mL and carbon balances between 64% and 75%. A clear structure–activity relationship was established, showing that increasing BET surface area from ~11 to 93 m^2/g significantly enhances activity, while Pd particle size plays a more critical role than metal loading. Among all monometallic systems, the best catalytic performance was observed for catalysts treated at 600 °C, reaching TON and TOF values up to 1573 and 524 h^{-1}, respectively.

Bimetallic modification further improved catalytic behavior. PdCo catalysts systematically outperformed PdNi systems, achieving formic acid conversions up to 98% and improving carbon balance, compared to a maximum for Pd–Ni catalysts for monometallic Pd. These results confirm that Co promotes more efficient hydrogen formation and carbon utilization, while Ni tends to favor stronger adsorption of intermediates and lower overall efficiency.

In the HMF hydrodeoxygenation reaction, the catalysts exhibited high HMF conversions generally above 75–95%, confirming efficient hydrogen transfer from formic acid. However, selectivity toward 2,5-DMF varied significantly depending on catalyst composition. Monometallic Pd achieved only about DMF yield, whereas PdC catalysts markedly enhanced performance. The best catalyst, 5CN, reached a 2,5-DMF yield of approximately; along with a TON of 115.8 and a TOF of 19.3 h^{-1}, representing the highest catalytic efficiency in the series. In comparison, PdN catalysts remained below DMF yield, with significantly higher humin formation and lower selectivity.

Recyclability tests of the best catalyst (5CN) demonstrated stable activity over four consecutive cycles, maintaining near-complete conversion (for two cycles, in the third, and in the

fourth). However, selectivity toward 2,5-DMF decreased, indicating gradual deactivation likely due to surface restructuring, partial sintering, or carbonaceous deposition.

In general, this thesis establishes that efficient 5-HMF conversion through formic acid assisted hydrodeoxygenation critically depends on the synergistic interaction between Pd and a second metal, as well as on the structural properties of the carbon nitride support. Among all investigated systems, PdCo catalysts, particularly **5–CN**, emerge as the most effective, combining high hydrogen generation efficiency, strong catalytic activity, and the highest selectivity toward 2,5-DMF. These findings provide a clear design strategy for developing next-generation catalysts for sustainable liquid fuel production from biomass-derived platform molecules.

Future work should focus on extending the current findings by systematically evaluating the performance of the optimized **5CN** catalyst supported on alternative materials under identical reaction conditions, in order to elucidate the influence of the support on activity, selectivity, and stability. In parallel, theoretical investigations based on density functional theory (DFT) are recommended to provide molecular-level insight into the reaction mechanism, adsorption behavior, and the nature of the catalytically active sites. Such computational studies would complement the experimental observations and help rationalize structure–activity relationships.

Further research should also broaden the scope of hydrogenation/deoxygenation (HDO) reactions by examining additional biomass-derived platform molecules, including levulinic acid and furfural, to assess the versatility and robustness of the catalytic system.

Finally, a key long-term objective is the development of an integrated one-pot catalytic process for the direct conversion of glucose to 2,5-dimethylfuran (2,5-DMF), which would represent a significant advancement toward more efficient and sustainable biorefinery pathways.

Abstract

This work studies the behavior of a series of Pd/C_3N_4 catalyst in the reaction of formic acid dehydrogenation and the use of the latter as H-donor for 2,5-hydroxymethyl furfural hydrodeoxygenation (5-HMF). Firstly, a series of supports have been synthesized from melamine and urea as a function of precursors ratio and temperature of their condensation. The different synthetic conditions resulted in materials with very different specific surface areas and N-containing groups on the surface which influenced Pd deposition. The resulting nitrogen defects facilitated enhanced electron transfer from nitrogen to Pd due to the close positioning of Pd nanoparticles near nitrogen sites. Consequently, the physicochemical and catalytic properties of the materials were notably impacted. In addition, the most performant support was identified and selected for further catalyst design. This optimized support was subsequently impregnated with PdCo and Pd Ni bimetallic systems, which exhibited improved catalytic performance compared to their corresponding monometallic counterparts, highlighting the beneficial effect of alloying on catalytic activity and stability.

Keywords: FA dehydrogenation, H2, CO_2, 5-HMF hydrodeoxygenation, 2,5-DMF

Résumé

Ce travail étudie le comportement d'une série de catalyseurs Pd/C_3N_4 dans la réaction de déshydrogénation de l'acide formique et l'utilisation de ce dernier comme un donneur d'hydrogène pour l'hydrodésoxygénation du 2,5-hydroxyméthyl furfural (5-HMF). Tout d'abord, une série de supports a été synthétisée à partir de mélamine et d'urée en fonction du rapport des précurseurs et de la température de leur condensation. Les différentes conditions de synthèse ont conduit à des matériaux avec des surfaces spécifiques très différentes et des groupes contenant N sur la surface qui ont influencé le dépôt de Pd. Les défauts d'azote résultants ont facilité un transfert d'électrons amélioré de l'azote vers le palladium en raison du positionnement rapproché des nanoparticules de palladium à proximité des sites azotés. Par conséquent, les propriétés physico-chimiques et catalytiques des matériaux ont été considérablement impactées. En outre, le support le plus performant a été identifié et sélectionné pour la conception de nouveaux catalyseurs. Ce support optimisé a ensuite été imprégné par des systèmes bimétalliques PdCo et PdNi, lesquels ont montré de meilleures performances catalytiques que leurs homologues monométalliques correspondants, mettant en évidence l'effet bénéfique de l'alliage sur l'activité catalytique et la stabilité.

Mots clés: FA déshydrogénation, H2, CO_2, 5-HMF hydrodésoxygénation, 2,5-DMF

الملخص

تدرس هذه الأطروحة سلوك سلسلة من المحفزات Pd/C_3N_4 في تفاعل نزع الهيدروجين من حمض الفورميك، واستخدام هذا الأخير كمانح للهيدروجين في تفاعل نزع الأكسجين الهيدروجيني لمركب 5-هيدروكسيميثيل فورفورال .(5-HMF) في البداية، تم تحضير سلسلة من الحوامل انطلاقاً من الميلامين واليوريا، وذلك بدلالة نسبة الطليعات ودرجة حرارة التكاثف. أدت ظروف التحضير المختلفة إلى مواد ذات مساحات سطحية نوعية متباينة بشكل كبير، وبمجموعات نيتروجينية مختلفة على السطح، مما أثر على ترسيب البالاديوم (Pd). وقد ساهمت العيوب النيتروجينية الناتجة في تعزيز انتقال الإلكترونات من النيتروجين إلى البالاديوم، نتيجة التوضع القريب لجسيمات Pd النانوية من مواقع النيتروجين. وبناءً على ذلك، تأثرت الخصائص الفيزيائية-الكيميائية والخصائص التحفيزية لهذه المواد بشكل ملحوظ .بالإضافة إلى ذلك، تم تحديد أفضل دعامة أداءً واختيارها لتصميم محفزات جديدة. ثم تم تشريب هذه الدعامة المُحسّنة بأنظمة ثنائية المعدن PdCo وPdNi ، والتي أظهرت أداءً حفزيًا أفضل مقارنةً بنظيراتها أحادية المعدن، مما يبرز التأثير الإيجابي لعملية تكوين السبيكة على النشاط الحفزي والاستقرار.

الكلمات المفتاحية :نزع الهيدروجين من حمض الفورميك، H_2، CO_2، نزع الأكسجين بالهدرجة لـ5-HMF، 2, 5-DMF.